國 立 交 通 大 學

顯示科技研究所

碩士論文

氮化鎵奈微米共振腔發光元件研究

The Study of GaN-based Micro/Nano Cavity Light Emitting Devices

研究生：葉家銘	Student：Jia-Ming Ye
指導教授：盧廷昌	Advisor：Tien-Chang Lu
陳瓊華	Chiung-Hua Chen

中華民國 一百零一 年 九 月

氮化鎵奈微米共振腔發光元件研究

The Study of GaN-based Micro/Nano Cavity Light Emitting Devices

研究生：葉家銘　　Student：Jia-Ming Ye

指導教授：盧廷昌　　Advisor：Tien-Chang Lu

陳瓊華　　Chiung-Hua Chen

國立交通大學

顯示科技 研究所

碩 士 論 文

A dissertation

Submitted to Display Institute

College of Electrical Engineering and Computer Science

National Chiao Tung University

In Partial Fulfillment of the Requirements

For the Degree of Master

In Electro-Optical Engineering

September 2012

Hsinchu, Taiwan, Republic of China

中 華 民 國 一百零一 年 九

氮化鎵奈微米共振腔發光元件研究

研究生：葉家銘　　　　　　　　指導教授：盧廷昌　教授

陳瓊華　教授

國立交通大學顯示科技研究所

摘　　要

本篇論文旨在探討共振腔長在數個微米至奈米的氮化鎵發光元件的製程技術及設計原理。以期能夠成功製作出電激發氮化鎵面射型雷射及奈米雷射。

首先，透過在量子井上成長氮化鋁，做為混合式布拉格反射鏡氮化鎵微共振腔結構的電流阻擋層，取代過去只有成長氮化矽在在 p 型氮化鎵上做絕緣層的方法，以期達到更加的電流侷限效果以及側向的光學侷限。更設計了環型的透明導電層取代原先的圓型透明導電層，希望能減少共振腔內部的損耗。接著，由於考慮到了藍寶石基板本身的電導率和熱傳導率不佳，以及氮化鎵-氮化鋁布拉格反射鏡的製作控制困難。我們採用了雷射剝離技術製作雙介電質布拉格反射鏡搭配氮化鋁電流阻擋層的電激發微共振腔發光元件。在元件複雜的製作完成之後，我們量測元件得到了一個高(800)以上的共振腔品質因子，並量測到了光激發雷射操作以及橫向模態，雖然沒有達到電激發雷射操作，但確實證明了此種設計製作的可行性，並且在最後提出元件可改良以及最佳化的方向。

第二部分，我們採用波導理論及有限元素分析法模擬設計了一個奈米雷射結構，證明了金屬能加強對光場局限的能力提升奈米級半導體元件的表現。

The Study of GaN-based Micro/Nano Cavity Light Emitting Devices

Student: Jia-Ming Ye Advisor: Prof. Tien-Chang Lu

Prof. Chiung-Hua Chen

Department of Display Institute

National Chiao-Tung University

Abstract

The purpose of this thesis is to discuss the design rules and improvement on the process of GaN-based micro/nano cavity light emitting devices so that we can successfully fabricate a laser lift-off GaN-based VCSELs and GaN-based nanolaser.

At first, we formed a GaN microcavity of hybrid Bragg reflector with a current blocking layer by growing AlN on the quantum well instead of growing SiN on the p-GaN conventionally in order to achieve a better current confinement and lateral optical confinement. Additionally, we designed a ring-shape transparent contact layer in replace of the original round-shape one to reduce the internal loss of the resonant cavity. To modify the intrinsic property of the sapphire substrate (poor electric and thermal conductivity) and to overcome the difficulty in the process of the AlN/GaN DBR, we used the laser lift-off technique to fabricate a MCLED with two dielectric DBRs and an AlN current blocking layer. After the complicated fabrication process, we obtained a high Q factor (800) and transvers modes from the device of laser operation by optically pumped. Even though we did not achieve the laser operation by electrically pumped, we have proved the feasibility of this method and gave some suggestion to improve and optimize the fabrication.

Second, we design a nanolaser by using finite element method and circular waveguide theory, the results prove that metal can enhance optical confinement and improve the performance of nanolaser.

Acknowledgement

首先誠摯的感謝指導教授盧廷昌博士及陳瓊華博士,兩位老師悉心的教導使我得以一窺半導體雷射領域的深奧，不時的討論並指點我正確的方向，使我在這些年中獲益匪淺。老師對學問的嚴謹更是我輩學習的典範。

兩年裡的日子,實驗室裡共同的生活點滴,學術上的討論、言不及義的閒扯、讓人又愛又怕的宵夜、趕作業的革命情感、因為睡太晚而遮遮掩掩閃進實驗室........，感謝眾位學長姐、同學、學弟妹的共同砥礪，你/妳們的陪伴讓兩年的研究生活變得絢麗多彩。

感謝博孝、昀霖、政宏、映佑、輝閔、政聰學長、巧芸、于彬學姐們不厭其煩的指出我研究中的缺失，且總能在我迷惘時為我解惑，也感昱薰、盛雲、書賢、育誠同學的幫忙，恭喜我們順利走過這兩年。實驗室的柏皓、宇勝學弟們當然也不能忘記，你們的幫忙及搞笑我銘感在心。

家人在背後的默默支持更是我前進的動力，沒有的體諒、包容，相信這兩年的生活將是很不一樣的光景。

最後，謹以此文獻給我摯愛的雙親。

家銘　　于 101 年 9 月 7 日

交通大學顯示所

Content

摘　　要 i

Abstract ii

Acknowledgement iv

Content v

List of Figures vii

Chapter 1 10

Introduction 10

1.1 Wide-bandgap III-V materials 10

1.2 Nitride-based Vertical Cavity Surface Emitting Lasers 11

1.2.1 Fully Epitaxial Grown VCSELs 12

1.2.2 VCSELs with Two Dielectric Mirrors 13

1.2.3 VCSELs with Hybrid Mirrors 14

1.3 Nanolasers 15

1.3.1 Metal Coated Nanolasers 17

1.3.2 Metal Coated Nanolasers with Surface Plasmon Effects 18

1.4 Motivation & Objective of the Thesis 19

Reference 21

Chapter 2 24

Numerical Methods, Fabrication Instruments, Measurement Setups and Process Parameters 24

2.1 Numerical Simulation Methods 24

2.2.1 Transfer Matrix Method 24

2.2.2 Finite Element Method 25

2.2 Fabrication Instruments 25

2.2.1 Electron-Beam Lithography System 25

2.2.2 Mask Alignment and Exposure System 26

2.2.3 Plasma-Enhanced Chemical Vapor Deposition (PECVD) 28

2.2.4 Electron Beam Physical Vapor Deposition 29

2.2.5 Dry Etching System 30

2.3 Measurement Setups 32

2.3.1 Four Point Probe 32

2.3.2 Scanning Electron Microscopy (SEM) 32

2.3.3 Photoluminescence Spectroscopy (PL) 33
2.3.4 Electroluminescence Spectroscopy (EL) 35
2.3.5 Atomic Force Microscope (AFM) 35
2.3.6 Others 38
2.4 Fabrication Process Parameters and Techniques 38
2.4.1 Initial Clean (I.C.) 38
2.4.2 Lithography Techniques and Parameters 39
2.4.3 PECVD Deposition Techniques and Parameters 41
2.4.4 Dry Etching Techniques and Parameters 42
2.4.5 Polish techniques 43
2.4.6 Lift-off techniques with photoresists 43
Reference 44
Chapter 3 45
An AlN Layer for the Current Confinement in GaN-Based VCSELs with Two Dielectric Distributed Bragg Reflectors 45
3.1 Operation principle of VCSELs 45
3.1.1 Fabry–Pérot cavity 45
3.1.2 Characteristics of Distributed Bragg reflectors (DBR) 46
3.1.3. Quality factor (Q) 48
3.1.4 Transverse mode 49
3.1.5 Carrier density rate equation 50
3.2 Fabrication flowchart 54
3.3 Characteristics of AlN layer 71
3.4 Results and Discussion 73
3.4.1 The optical characteristics of VCSELs 73
3.5 Summary 81
Reference 83
Chapter 4 84
Silver Coated Metal-Cavity Nanolasers with Distributed Bragg Reflectors 84
4.1 Operation Principle of Metal-Cavity Nanolasers 84
4.1.1 Surface Plasmons Theory 84
4.1.2 Circular Waveguide Theory 87
4.2 Design and Simulation of Metal-Cavity Nanolasers 92
4.3 Summary 102
Reference 103

Chapter 5 104

Conclusion and Future Work 104

5.1 Conclusion 104

5.2 Future work 105

List of Figures

Fig. 1.1 The band-gap diagram of Ⅱ-Ⅵ and Ⅲ-Ⅴ group semiconductor materials 11

Fig. 1.2 The schematic diagram of a vertical-cavity surface emitting laser diode. 12

Fig. 1.3 The schematic diagram of three nitride based VCSELs structures 15

Fig. 1.4 (a) Schematic of a nanopillar laser monolithically integrated onto silicon. (b) SEM image showing the well-faceted geometry of the nanopillar optical cavity. (c) First-order and (d) higher-order standing waves 17

Fig. 1.5 The structure of cavity formed by a rectangular semiconductor pillar encapsulated in Silver. (a) The schematic showing the device layer structure. (b) the scanning electron microscope image showing the semiconductor core of one of the devices. The scale bar is 1 micron. 18

Fig. 1.6 (A) Schematic of device: a single nanorod on a SiO_2 covered epitaxial Ag film (28 nm thick). The energy-density distribution (right) is calculated by the eigenmode method. (B) SEM images of nanorods. The left-hand SEM image shows the actual nanorod on epitaxial Ag film (C) STEM and TEM structural analyses 19

Fig. 2.1 Commercial Software of transfer matrix method (TFCalc 3.5) and finite element method (COMSOL 4.2) 25

Fig. 2.2 Schematic diagram of e-beam lithography and E-beam Lithography System (ELX-7500) 26

Fig. 2.3 Simplified illustrations of dry etching using positive photoresist during a photolithography process in semiconductor micro-fabrication. 27

Fig. 2.4 Alignment System (ABM Model 60 DUV/MUV/NearUV) 28

Fig. 2.5 Plasma Enhanced CVD System (SAMCO PECVD Model PD-220) 29

Fig. 2.6 Simplified illustration of e-beam evaporator 30

Fig. 2.7 Coating system with optical in-situ monitor (KS-800OPTO) and E-gun evaporator (ULVAC EBX-8C) 30

Fig. 2.8 ICP-RIE System (Oxford Plasmalab System 100) and ICP-RIE System (SAMCO RIE-101PH). 31

Fig 2.9 Schematic of 4-point probe configuration and Four point probe system (NAPSON RT-7) 32

Fig. 2.10 Scanning electron microscope System (JSM-7000F) 33

Fig. 2.11 Interband transitions in photoluminescence system 34

Fig. 2.12 The optical pumping system in experiment Using Nd:YVO4 355 nm pulse laser as pumping source, the pulse width is 0.5 ns, and repetition rate is 1k Hz. The laser light is focused by convex lens and pumped onto the device. Use objective lens to receive the light which emit from the device, and take flip mirror to control the optical path transmitting to CCD or fiber. 34
Fig. 2.13 The EL measurement system for electrically driving 35
Fig. 2.14 The concepts of AFM and the optical lever: (a) a cantilever touching a sample, (b) illustration of the meaning of "spring constant" as applied to cantilevers, (c) the optical lever. Scale drawing; the tube scanner measures 24 mm in diameter, while the cantilever is 100 µm long typically. 37
Fig. 2.15 The AFM feedback loop. A compensation network monitors the cantilever deflection and keeps it constant by adjusting the height of the sample. Atomic Force Microscope（D3100） 37
Fig. 2.16 N&K Surface Profile Analyzer (N&K 1500) 38
Fig. 2.17 Photography of diamond lapping films 43
Fig. 3.1 Schematic of a laser cavity showing the length, L, and reflection coefficients of the two-end facets, r_1 and r_2. 46
Fig. 3.2 Schematic diagrams of DBRs 46
Fig. 3.3 transmission pattern of a Fabry-Perot cavity in frequency domain 49
Fig. 3.4 Reservoir with continuous supply and leakage as an analog to a DH active region with current injection for carrier generation and radiative and nonradiative recombination 51
Fig. 3.5 Overall schematic of a GaN-based VCSEL with two dielectric DBRs and an AlN layer. 55
Fig. 3.6 Process flow chart of VCSELs from (a) to (n). 60
Fig. 3.7 Photography of VCSELs with incomplete isolation and surface were destroyed after laser liftoff. Silver regions are GaN material and yellow regions are contact metal which original covered by GaN but now exposed to air. 61
Fig. 3.8 SEM image of different apertures of SiO2 mask (a) 5 µm (b) 8µm (c) 10µm (d) 15µm 62
Fig. 3.9 SEM image of the SiO2 mask and the regrowth AlN layer 63
Fig. 3.10 The reflection spectrum of 10 pairs of TiO_2 /SiO_2 p-DBR 64
Fig. 3.11 Photography of VCSELs with p-contact layer and sapphire polish (a) front side (b) back side. 65
Fig. 3.12 PL spectrum before laser lift-off 66
Fig. 3.13 Photography of lift-off sapphire substrate 67
Fig. 3.14 OM image and roughness comparison from step 9 to step 11. 68
Fig. 3.15 Cross-sectional view and a top view before small mesa etching 69
Fig. 3.16 Photography of unwanted n-contact layer lifted off by PR stripper 70
Fig. 3.17 The reflection spectrum of 11 pairs of HfO_2 /SiO_2 n-DBR 71
Fig. 3.18 Photography of final VSCELs in front side and back side 71

Fig. 3.19 AFM image of three different re-growth temperatures. 73
74
Fig. 3.21 The simulated reflectivity without n-DBR was deposited 74
Fig. 3.22 The PL spectrum before n-DBR was deposited 75
Fig. 3.23 The PL spectrum before n-DBR was deposited 76
Fig. 3.24 The light output power verse the pumping energy density 77
Fig. 3.25 The polarization characteristics of the laser emission from the VCSEL above the threshold 77
Fig. 3.26 The logarithm light output power and laser emission peak linewidth verse the effective pumping energy density penetrating to QWs 79
Fig. 3.27 The electric field intensity simulated by transfer matrix, the horizontal axis correspond the layer arrangement of the VCSELs. 79
Fig. 4.1 (a)The schematic representation of electron density wave propagating along a metal-dielectric interface (b) the electric field distribution around the interface (c) dispersion curve of surface plasmon 85
Fig. 4.2 A circular waveguide 87
Fig. 4.3 Bessel function of the first kind and second kind 89
Fig. 4.4 The lowest five modes and corresponding electric fields pattern E **in circular waveguides** 91
Fig. 4.5 The z-component magnetic field H_z **and z-component poynting vector** P_z **for several TEnm modes** 91
Fig. 4.6 Schematic of an nanolaser combining DBRs and metal 92
Fig. 4.7 The Quality factor distribution of different modes for an laser 93
Fig. 4.8 (a) Top view illustration of the structure (b) surface mode (c) hybrid mode (d) lowest four waveguide modes 94
Fig. 4.9 (a) Reflectivity and (b) absorptivity of common metal reflector 95
Fig. 4.10 (a) Real part of complex dielectric constant (b) n and k of common reflector 95
Fig. 4.11 Quality factor of (a) different metal (b) different thickness of Ag 96
Fig. 4.13 Cutoff wavelength of the structure 98
Fig. 4.15 (a) Quality factor, confinement factor and (b) threshold gain verse t height of InGaN/GaN quantum wells structure 99
Fig. 4.16 (a) Quality factor , confinement factor and (b) threshold gain verse diameter of InGaN/GaN quantum wells structure 100
Fig. 4.17 SEM image of bulk GaN rod before Al deposition 101
Fig. 4.18 PL spectrum and L.L curve of bare GaN rod with 1.2μm in height and 3.6μm in diameter. 102
Fig. 4 .19 PL spectrum and effective L.L curve of metal coated GaN rod with 1.2μm in height and 3.6μm in diameter. 102

Chapter 1

Introduction

1.1 Wide-bandgap III-V materials

Wide-bandgap nitride materials have attracted great attention over past decade due to their promising potential for the applications of optoelectronic devices such as flat panel display, competing storage technologies, automobiles, general lighting, and biotechnology, and so on [1-4]. The III-N materials are synthesized mainly using the four kinds of atoms, gallium (Ga), nitride (N), aluminum (Al), and indium (In), to form the binary and ternary compounds such as GaN, InN, AlN, InxGa1-xN, and AlxGa1-xN etc. The bandgap of these materials cover a very wide range from 0.9eV to 6.1eV (Fig 1.1), which implies the large band off-set in hetero-structure could be achieved in this material system. The large band off-set is very useful to confine carrier for the high-speed and high power electronic devices and light emitting devices [5]. Their wide-range bandgap also provide possibility of full-color emission because they cover red, green, and blue emission regions. This property further makes nitride materials important and important for the applications of full-color display or solid-state lighting. Furthermore, nitride materials still have lots of advantages such as high bond energy (~2.3eV), high saturation velocity (~2.7 $\times$ 10^4 cm/s), high breakdown field (~2 $\times$ 10^6 V/cm), and strong excitonic energy (>50meV) [6-7]. Although wurtzite nitride compounds have some unique properties such as piezoelectric field and spontaneous polarization which is harmful to the efficiency of light emitting devices, the material system still is a very strong candidate for the future optoelectronic applications due to their superior material properties.

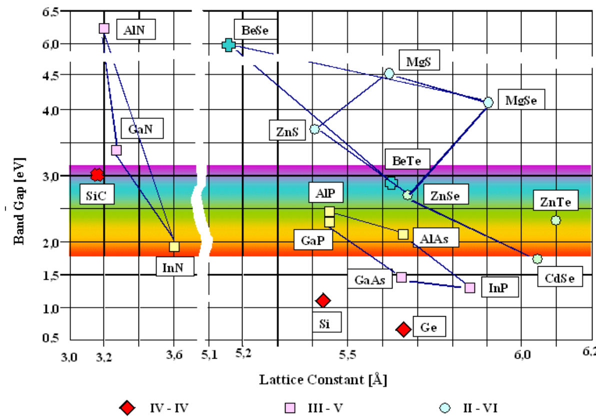

Fig. 1.1 The band-gap diagram of Ⅱ - Ⅵ and Ⅲ - Ⅴ group semiconductor materials

1.2 Nitride-based Vertical Cavity Surface Emitting Lasers

Although the optimization of the edge emitting laser keeps going, some properties of this kind of laser are unfavorable. One of those properties is its elliptic beam shape. On one hand, the coupling efficiency would be low as the elliptic beam is coupled into optical fiber (typically in the form of circular core). On the other hand, for the application of storage, the elliptic beam not only makes each writing pixel larger but also raises expenses for correcting light shape. Usually, this kind of laser shows slightly large divergence angle to be over ten degree. This also is disadvantageous to the projection. Furthermore, the side emitting laser devices also makes the testing of devices a tough task. The wafer should be cut into several stripes (several laser devices on one strip) before the testing. For a commercial product, the complicated testing would result in a poor producing efficiency and be disadvantageous. Therefore, in order to have a superior laser device, K. Iga demonstrated a new kind of laser diodes, vertical cavity surface emitting laser, in 1977. Vertical cavity surface emitting laser (VCSEL) is a vertical-emitting-type laser. It is formed by sandwiching a few-lambda cavity in a pair of reflectors, usually in the

form of distributed Bragg reflector (DBR), with a very high reflectivity (>99.9%) as shown in Fig. 1.2. In contrast to EELs, photons in the cavity of VCSEL are vertically in resonance and emit outside perpendicularly to the surface of the structure. This laser diode can have many advantageous properties than conventional edge emitting laser, such as circular beam shape, lower divergence angle, two-dimensional laser array possible, efficient testing, low threshold, and so on. Owing to these superior performances, VCSELs had become very attractive and started to be applied to the commercial products at long wavelength range. In fact, short-wavelength VCSELs are also very promising for the applications of storage, display, and projection. In particular, the use of two-dimensional arrays of blue VCSELs could further reduce the read-out time in high density optical storage and increase the scan speed in high-resolution laser printing technology. In recent years, several efforts have been devoted to the realization of nitride-based VCSELs. In recent years, several efforts have been devoted to the realization of nitride-based VCSELs [8-17].

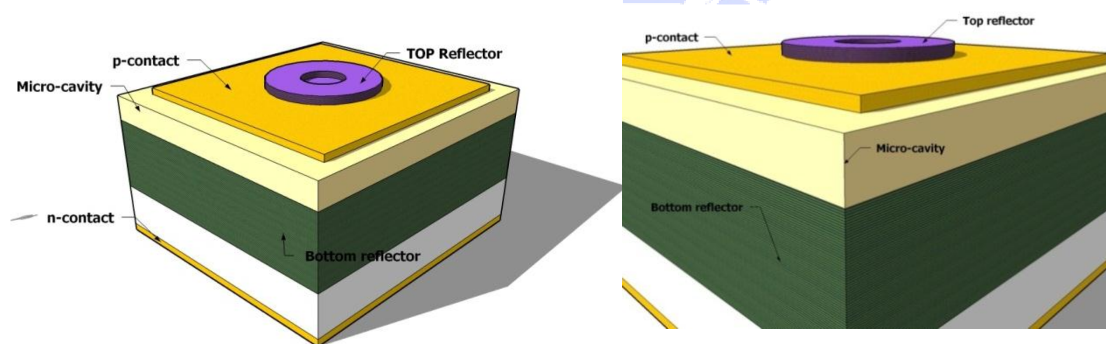

Fig. 1.2 The schematic diagram of a vertical-cavity surface emitting laser diode.

1.2.1 Fully Epitaxial Grown VCSELs

In 2005, J. F. Carlin [17] and E. Feltin [18] demonstrated the wholly epitaxial and high quality nitride-based micro-cavity (as shown in Fig. 1.3(a)) using

metalorganic vapor phase epitaxy (MOVPE or MOCVD). They used the lattice-matched AlInN/GaN as the bottom and top reflectors to avoid cracks happened due to the accumulation of the strain after stacking large pairs of layers. The reflectivity of AlInN/GaN could be achieved as high as 99.4%. They showed the 3/2-lambda cavity emitted a very narrow emission with a linewidth of 0.52 nm, corresponding to a quality factor of ~800.

1.2.2 VCSELs with Two Dielectric Mirrors

Compared to epitaxial grown reflectors, the fabrication of dielectric mirrors is relatively simple. Furthermore, the large index difference of dielectric mirrors makes them could easily have wide stop band (>50nm) and high reflectivity (>99%) by coating just few stacks of 1/4-lambda-thick layers. Therefore, using dielectric mirrors to accomplish nitride-based VCSELs had begun attractive. Song et al. [9], Tawara et al. [10] and J. T. Chu *et. al* [12] successively reported the structure (as shown in Fig. 1.3(c)) after 2000. They employed some process techniques such as wafer bonding and laser lift-off to make dielectric mirrors be coated onto both sides of nitride-based cavity. They showed a micro-cavity could have a very high quality factor to be greater than 400 and achieve lasing action using optical pumping. In addition, Takashi Mukai et al. [13] have demonstrated the CW lasing at room temperature in a GaN-based vertical-cavity surface-emitting laser (VCSEL) by current injection in 2008. Its optical cavity consisted of a 7λ-thick GaN semiconductor layer and an indium tin oxide layer for p-contact embedded between two SiO_2/Nb_2O_5 dielectric distributed Bragg reflectors. The threshold current of VCSEL is 13.9kA/cm^2 and the lasing wavelength is about 414 nm. However, the fabrication technique of this kind of VCSEL is relatively complicated, and its cavity

length cannot be efficiently controlled due to polishing problems.

1.2.3 VCSELs with Hybrid Mirrors

The so-called hybrid mirrors are a combination of two different kinds of reflectors, for example, a dielectric mirror and an epitaxial reflector. Typically, the fabrication of this structure is to grow bottom reflector and cavity using MOCVD and then coat dielectric mirror to complete VCSEL structure (as shown in Fig. 1.3(b)). The hybrid-cavity nitride-based VCSEL\formed by the dielectric mirror and the epitaxially grown high-reflectivity $GaN/Al_xGa_{1-x}N$ DBR was reported earlier. In 1999, Someya et al. [8] used 43 pairs of $Al_{0.34}Ga_{0.66}N/GaN$ as the bottom DBR and reported the lasing action at ~400nm. Then, Zhouet al. [11] also employed a bottom DBR of 60 pairs $Al_{0.25}Ga_{0.75}N/GaN$ and observed the lasing action at 383.2nm. Both these AlGaN/GaN DBR structures required large numbers of pairs due to the relatively low refractive index contrast between AlxGa1-xN and GaN. Therefore, recently some groups began to study the AlN/GaN for application in nitride VCSEL. The DBR structure using AlN/GaN has higher refractive index contrast ($\Delta n/n=0.16$) [19] that can achieve high reflectivity with relatively less numbers of pairs. It has wide stop band that can easily align with the active layer emission peak to achieve lasing action. However, the AlN/GaN combination also has relatively large lattice mismatch (~2.4%) and the difference in thermal expansion coefficients between GaN ($5.59x10^{-6/}K$) and AlN ($4.2x10^{-6}/K$) that tends to cause cracks in the epitaxial film during the growth of the AlN/GaN DBR structure and could result in the reduction of reflectivity and increase in scattering loss. With the mature of epitaxy techniques, the high-reflectivity AlN/GaN DBR structure with relatively smooth surface morphology has become possible with just twenty or thirty pairs [20]. In

comparison of these three VCSELs, it doesn't require complicated process such as laser lift-off technique to complete a hybrid VCSEL device. This means the fabrication of such structure is stable and reliable comparing to other structures. Thus, the hybrid structure is more advantageous in the aspects of fabrication and commercialization In fact, the investigation of the characteristics of the GaN-based VCSELs has gradually attracted more attentions. Kako et al. [21] investigated the coupling efficiency of spontaneous emission (β) and the polarization property of the nitride VCSEL and obtained a high β value of 1.6×10^{-2} and a strong linear polarization of 98%. Tawara et al. [10] also found a high β value of 10^{-2} in the nitride VCSEL with two dielectric mirrors. Honda et al. reported the estimation of high characteristics temperature of GaN-based VCSEL [22]. These all mean the development of nitride-based VCSEL and the understanding of the laser performance has become more and more important.

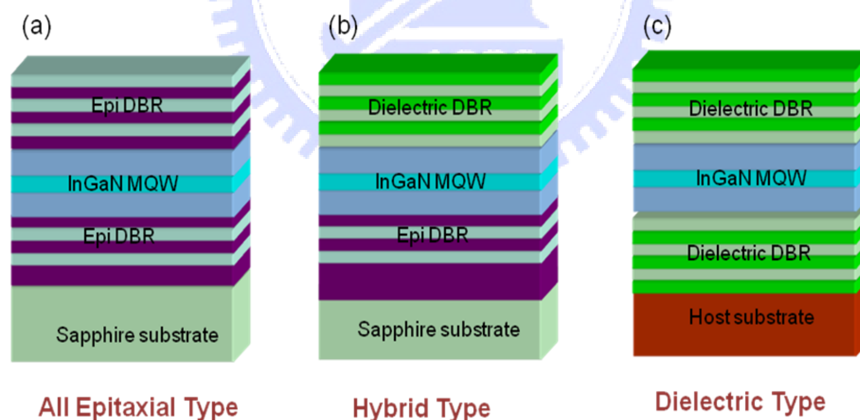

Fig. 1.3 The schematic diagram of three nitride based VCSELs structures

1.3 Nanolasers

Nanolasers [23] refer generally to miniaturized lasers that have sizes comparable to or smaller than wavelength involved. The driving force behind the development of

nanolasers, is the well-recognized sizemismatch between silicon-based microelectronic devices and the compound-semiconductor-based optoelectronic devices. As is evidenced by Moore's law for microelectronics, miniaturization and large-scale integration can lead to drastic improvement of performance and simultaneous decrease in cost. Efforts in integrated photonics over the last few decades have led to much less impressive results than electronic integrated circuits (ICs). Several of paradigm-shifting approaches in the last decade have resulted in record size reduction of microcavity lasers. These new approaches are best represented by the microdisk lasers supported on a pedestal [24–26], the photonic wire lasers [27] and photonic crystal (PC) lasers [28–31]. The high quality-factor cavity provided by the whisper-ing-gallery modes in microdisk lasers allows the gain volume to be reduced to the minimum. Similarly, high quality factor provided by photonic bandgap structures leads to a record size in optical mode volume. While the vertical size of disk and PC laser structures is sub-wavelength already, the lateral size is still comparably larger, on the order of 10 μm. Notice that at 2011, Roger Chen et al. [32] use a novel growth scheme to directly demonstrate the potency of bottom-up nano-optoelectronic integration of InGaAs nanopillar lasers. As show in Fig. 1.4, unique helically propagating cavity modes are used to strongly confine light despite the low refractive index contrast between InGaAs and silicon. Finally, all but one [28] of these lasers are so far optically pumped, whereas eventual device integration requires electrical injection lasers.

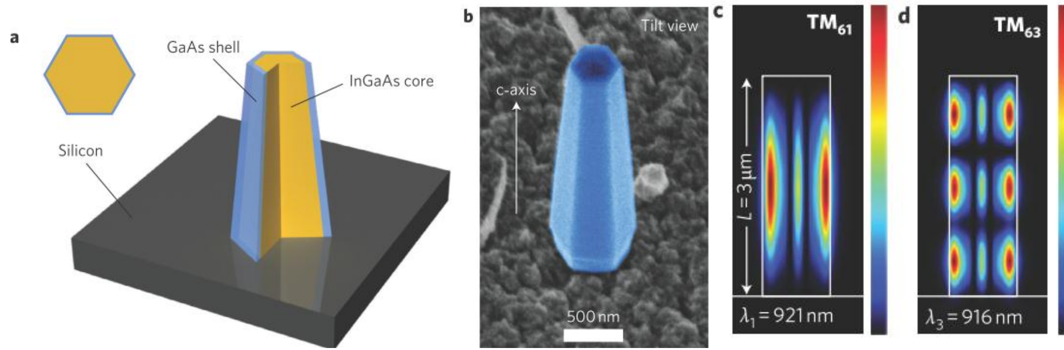

Fig. 1.4 (a) Schematic of a nanopillar laser monolithically integrated onto silicon. (b) SEM image showing the well-faceted geometry of the nanopillar optical cavity. (c) First-order and (d) higher-order standing waves

1.3.1 Metal Coated Nanolasers

Metal coated cavity has been intensely researched by scientist around the world. It could reduce the size o semiconductor laser to nano scale, even in subwavlentgh scale. This result breaks the diffraction limit which constrains the size of a laser that cannot be smaller than its nature wavelength. The lasing characteristics also be studied by researchers trying to explain the physical meaning.

As shown in Fig. 1.5 , Marin T. Hill et al. [33][34] demonstrated lasing in metal-coated nanocavity at 2007 and 2009. They coated silver and dielectric layer on the nanorod and observe lasing signal at 77K. After that, different designs of metal-coated nanocavtiy have reported experimentally or theoretically. Moreover, different kinds of metal have been use to form metal-coated nano cavity. From recent research results [33-37], researcher use silver, gold and aluminum to from the nano structure. At 2010, M. P. Nezhad et al. demonstrated a metal coated nanocavity with aluminum layer and SiO2 as the dielectric layer. They also proposed a theoretical analysis to show that optimization of the dielectric layer could have a higher chance to

get a better quality factor to achieve lasing action. K. Y. Yu et al. at 2010 demonstrated a nano-patch laser with metal coated above and below the gain medium, and analyze the lasing characteristic of the device [36]. In 2011, M. W. Kim et al. demonstrated lasing in metal-clad microring [37]. In summary, metal-coated nano cavity has been demonstrated experimentally in different structures includes nanorod , waveguide, and ring. In sum, recent research results mainly focus on InGaAsP material system, which has a lasing wavelength from red to infared region.

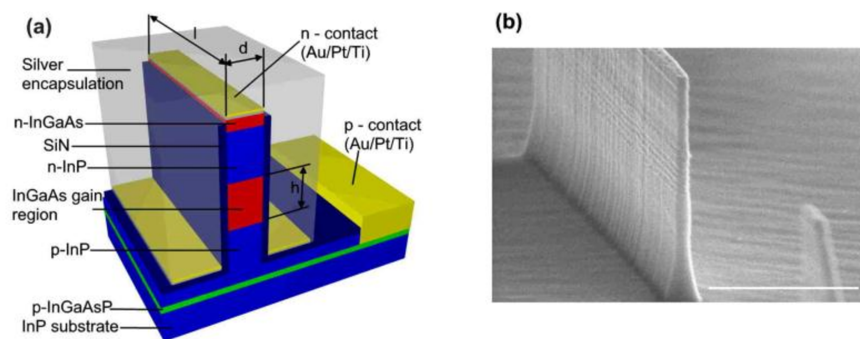

Fig. 1.5 The structure of cavity formed by a rectangular semiconductor pillar encapsulated in Silver. (a) The schematic showing the device layer structure. (b) the scanning electron microscope image showing the semiconductor core of one of the devices. The scale bar is 1 micron.

1.3.2 Metal Coated Nanolasers with Surface Plasmon Effects

At 2008, metal-coated waveguide structure had been demonstrated and bow-tie nanostructure had been demonstrated by S. W. Chang et al. [38]. The combination of surface plasmon effect and bow-tie structure shows a promising way theoretically in forming a semiconductor. At 2009 and 2011, Oulton group [39][40] report the experimental demonstration of nanometre-scale plasmonic lasers, generating optical modes a hundred times smaller than the diffraction limit. They realize such lasers using a hybrid plasmonic waveguide consisting of a high-gain cadmium sulphide

(CDS) semi-conductor nanowire, separated from a silver surface by a 5nm thick insulating gap. As shown in Fig. 1.6, Gwo group [41][42] demonstrated the 3D subdiff raction-limited laser operation in the green spectral region based on a metal-oxide- semiconductor (MOS) structure and use atomically smooth epitaxial Ag on Si as a improvement for plasmonics at 2011 and 2012.

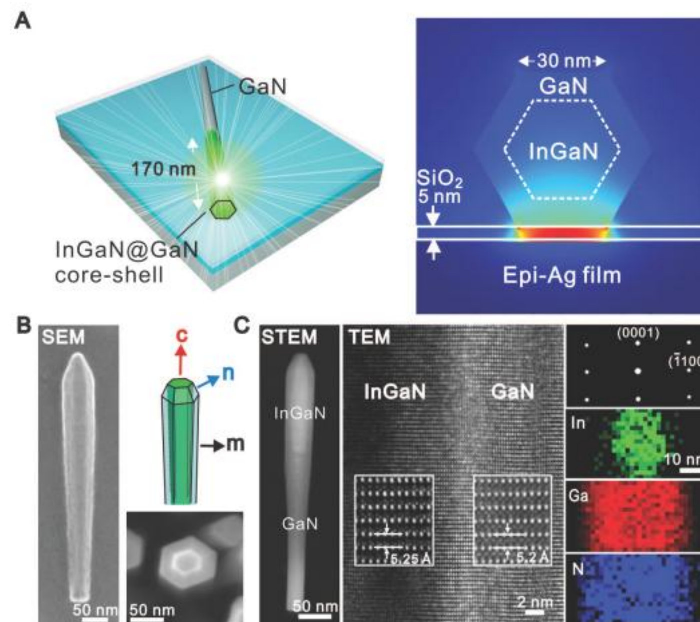

Fig. 1.6 (A) Schematic of device: a single nanorod on a SiO_2 covered epitaxial Ag film (28 nm thick). The energy-density distribution (right) is calculated by the eigenmode method. (B) SEM images of nanorods. The left-hand SEM image shows the actual nanorod on epitaxial Ag film (C) STEM and TEM structural analyses

1.4 Motivation & Objective of the Thesis

Our group reported room-temperature CW lasing of a GaN-based VCSEL with a bottom AlN/GaN DBR epitaxially grown on a sapphire substrate, a top dielectric DBR, and side-by-side n- and p-type contacts. And we also reported CW lasing both at 77 K and room temperature. However, the diffculty in obtaining high quality quantum wells (QWs) on such an epitaxial DBR and the heat generation induced by

current crowding in the side-by-side configuration still wait to be resolved. In this research, we utilize wafer bonding and laser liftoff techniques to permit VCSELs to be fabricated between two dielectric DBRs in a vertical contact structure, which improves the reflectivities of the DBRs , the current crowding effect and thermal dissipation. Besides, we add a unique AlN layer for current and optical confinement further improvement.

Metal-coated nanocavity shows huge potential to reduce the size of semiconductor laser into subwavelength scale. However, their research results mainly focus on InGaAsP material system and optical communication to infrared wavelength region. Shorter lasing wavelength and other material system have seldom been discovered by other groups in the world. The certified phenomena explanation and optimized design rule for metal-coated nanocavity is not clear. In this research, we utilize GaN as the gain medium for metal- coated nanocavity, combining with DBRs and silicon oxide. We try to clarify some myth for metal-coated nanocavity design. Finally, we design a minimum structure which is feasible and possible for laser operation.

The primary objective of this thesis focus on the development of GaN-based two dielectric VCSELs and the design of GaN-based metal-coated nanolaser. In chapter 2, we briefly introduce the instruments、process parameters and techniques which are used to fabricate and measure the devices. In chapter 3, we present experiments and results of lasing in AlN layer VCSELs at room temperature. In chapter 4, we use finite element method and circular waveguide theory to design a metal- coated nanolaser and shows some of preliminary results. Finally in chapter 5, we give a brief conclusion of this thesis.

Reference

[1] S. Nakamura, M. Senoh, N. Iwasa, and S. Nagahama, Jpn. J. Appl.Phys., 34, L797 (1995)

[2] S. Nakamura, T. Mukai, and M. Senoh, Appl. Phys. Lett.,64, 1687 (1994)

[3] S. Nakamura, M. Senoh, S.Nagahama, N.Iwasa, T. Yamada, T. Matsushita, Y. Sugimoto,and H.Kiyoku, Appl. Phys. Lett., 70, 868 (1997)

[4] S. Nakamura, Science, 281, 956 (1998)

[5] Y. Arakawa, IEEE J. Select. Topics Quantum Electron., 8, 823 (2002)

[6] H. Morkoc, Nitride Semiconductors and Devices (Spring Verlag, Heidelberg) (1999)

[7] S. N. Mohammad, and H. Morkoc, Progress in Quantum Electron., 20, 361 (1996)

[8] T. Someya, R.Werner, A. Forchel, M. Catalano, R. Cingolani, Y.Arakawa, Science, 285,1905 (1999)

[9] Y.-K. Song, H. Zhou, M. Diagne, A. V. Nurmikko, R. P. Schneider, Jr., C. P. Kuo, M. R. Krames, R. S. Kern, C. Carter-Coman, and F. A. Kish, Appl. Phys. Lett., 76, 1662 (2000)

[10] T. Tawara, H. Gotoh, T. Akasaka, N. Kobayashi, and T. Saitoh, Appl. Phys. Lett., 83, 830 (2003)

[11] H. Zhou, M. Diagne, E. Makarona, A. V. Nurmikko, J. Han, K. E. Waldrip and J. J. Figiel, Electron. Lett., 36,1777 (2000)

[12] J.T. Chu et. al., Jpn. J. Appl. Phys, 45, 2556 (2006).

[13] Yu Higuchi, Kunimichi Omae , Hiroaki Matsumura, and Takashi Mukai Applied Physics Express 1 , 121102 (2008)

[14] J. T. Chu et. al., Appl. Phys. Lett., 89, 121112 (2006).

[15]. C. C. Kao et. al., Appl. Phys. Lett., 87, 081105-1 (2005).

[16] C. C. Kao et. al., IEEE Photon. Technol. lett., 18, 877 (2006).

[17] J. F. Carlin, J. Dorsaz, E. Feltin, R. Butté, N. Grandjean, M. Ilegems, and M. Laügt, Appl.Phys. Lett., 86, 031107 (2005)

[18] E. Feltin, R. Butté, J. F. Carlin, J. Dorsaz, N. Grandjean, and M. Ilegems, Electron. Lett.,41, 94 (2005)

[19] T. Ive, O. Brandt, H. Kostial, T. Hesjedal, M. Ramsteiner, and K. H. Ploog, Appl. Phys. Lett., 85, 1970 (2004)

[20] H.H. Yao, C.F. Lin, H.C. Kuo, S.C. Wang, J. Crystal Growth, 262, 151 (2004)

[21] S. Kako, T. Someya, and Y. Arakawa, Appl. Phys. Lett., 80, 722 (2002)

[22] T. Honda, H. Kawanishi, T. Sakaguchi, F. Koyama and K. Iga, MRS Internet J. Nitride Semicond. 4S1, G6.2-1 (1999).

[23] Ning, C. Z. physica status solidi (b), NA-NA, doi:10.1002/pssb.200945436 (2010).

[24] A. F. Levi, S. L. McCall, S. J. Pearton, and R. A. Logan, IEEE Electron. Lett. 29, 1666 (1993).

[25] T. Baba, M. Fujita, A. Sakai, M. Kihara, and R. Watanabe, IEEE Photon. Technol. Lett. 9, 878 (1997).

[26] K. Srinivasan, M. Borcelli, O. Painter, A. Stintz, and S. Krishna, Opt. Express 14, 1094 (2006).

[27] J. P. Zhang, D. Y. Chu, S. L. Wu, S. T. Ho, W. G. Bi, C. W. Tu, and R. C. Tiberio, Phys. Rev. Lett. 75, 2678 (1995).

[28] H. Park, S. Kim, S. Kwon, Y. Ju, J. Yang, J. Baek, S. Kim, and Y. H. Lee, Science 305, 1444 (2004).

[29] S. Tomljenovic-Hanic, C. M. Sterke, M. J. Steel, B. J. Eggleton, Y. Tanaka, and S.

Noda, Opt. Express 15, 17248 (2007).

[30] A. J. Danner, J. C. Lee, J. J. Raftery, Jr., N. Yokouchi, and K. D. Choquette, Electron. Lett. 39, 1323 (2003).

[31] K. Nozaki, H. Watanabe, and T. Baba, Appl. Phys. Lett. 92, 021108 (2008).

[32] Chen, R., Tran, T. T. D., Ng, K. W., Ko, W. S., Chuang, L. C., Sedgwick, F. G., Chang-Hasnain, C., Nat. Photonics, vol5, March 2011.

[33] Hill, M. T., Marell, M., Leong, E. S. P., Smalbrugge, B., Zhu, Y. C., Sun, M. H., van Veldhoven, P. J., Geluk, E. J., Karouta, F., Oei, Y. S., Notzel, R.
Ning, C. Z., Smit, M. K. "L, Nat. Photonics, vol. 1, pp. 589, 2007.

[34] Hill, M. T. et al. o62Lasing in metal-insulator-metal sub-wavelength plasmonic waveguides. Opt. Express **17**, 11107-11112 (2009).

[35] Nezhad, M. P., Simic, A., Bondarenko, O., Slutsky, B., Mizrahi, A., Feng, L. A., Lomakin, V., Fainman, Y., Nat. Photonics, vol. 4, pp. 395, 2010.

[36] Yu, K., Lakhani, A. Wu, M. C., Opt. Express, vol. 18, pp. 8790, 2010

[37] M. W. Kim, P. C. Ku, Appl. Phys. Lett., vol. 98, pp. 131107, 2011.

[38] Chang, S. W., Ni, C. Y. A., Chuang, S. L., Opt. Express, vol. 16, pp. 10580, 2008

[39] Oulton, R. F. et al. doi:10.1038/nature08364 (2009).

[40] Sorger, V. J. et al. Nature communications **2**, 331, doi:10.1038/ncomms1315 2011.

[41] Wu, C. Y. et al. Nano Lett **11**, 4256-4260, doi:10.1021/nl2022477 (2011).

[42] Lu, Y. J. et al. P. Science **337**, 450-453, doi:10.1126/science.1223504 (2012).

Chapter 2

Numerical Methods, Fabrication Instruments, Measurement Setups and Process Parameters

2.1 Numerical Simulation Methods

2.2.1 Transfer Matrix Method

The transfer-matrix method [1] is a method used in optics and acoustics to analyze the propagation of electromagnetic or acoustic waves through a stratified (layered) medium [2]. This is for example relevant for the design of anti-reflective coatings and dielectric mirrors.

The reflection of light from a single interface between two media is described by the Fresnel equations. However, when there are multiple interfaces, such as in the figure, the reflections themselves are also partially transmitted and then partially reflected. Depending on the exact path length, these reflections can interfere destructively or constructively. The overall reflection of a layer structure is the sum of an infinite number of reflections, which is cumbersome to calculate.

The transfer-matrix method is based on the fact that, according to Maxwell's equations, there are simple continuity conditions for the electric field across boundaries from one medium to the next. If the field is known at the beginning of a layer, the field at the end of the layer can be derived from a simple matrix operation. A stack of layers can then be represented as a system matrix, which is the product of the individual layer matrices. The final step of the method involves converting the system matrix back into reflection and transmission coefficients.

2.2.2 Finite Element Method

The finite element method (FEM) [3] is a method used for finding the approximate solution of partial differential equations (PDE) that handle complex geometries (and boundaries), such as waveguides with arbitrary cross-sections, with relative ease. The field region is divided into elements of various shapes, such as triangles and rectangles, allowing the use of an irregular grid. The solution approach is based either on eliminating the differential equation completely (steady state problems), or rendering the PDE into an equivalent ordinary differential equation, which is then solved using standard techniques, such as finite differences. In a context of optical waveguides, the FEM can be used for mode solving and propagation problems. Two approaches to solve waveguide problem include the variational method and the weighted residual (Galerkin) method. Both methods lead to the same eigenvalue equation that needs to be solved.

Fig. 2.1 Commercial Software of transfer matrix method (TFCalc 3.5) and finite element method (COMSOL 4.2)

2.2 Fabrication Instruments

2.2.1 Electron-Beam Lithography System

Electron beam lithography, usually call as E-beam lithography, is a technique to utilize a beam of electrons to exposing the photo resist on the surface of a material, then selectively removing the photo resist on the film to transfer the pattern we want

onto the film. This could break the diffraction limit which constrains conventional photo lithography technique, and shows a promising chance to fabricate device in nano-scale.

The E-beam lithography system usually consists of an electron gun as source of electron, lenses for focusing, stage for moving the sample precisely under the electron beam, a beam blanker to control the exposure time of electron beam and a computer to control the whole system and the pattern. Fig. 2.2 shows the schematic diagram. For most of E-beam lithography system used for commercial applications are very expensive; therefore, for academic purpose, people usually convert an electron microscope into an E-beam lithography system with a relatively low cost. For thesis, we use an E-beam lithography system ELX-7500 as shown in Fig. 2.2.

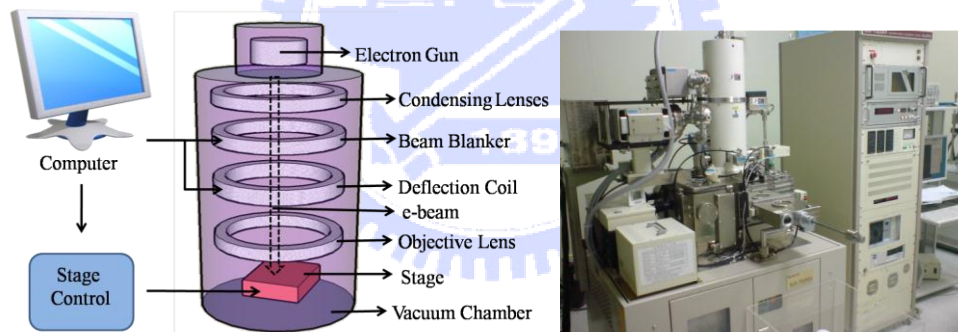

Fig. 2.2 Schematic diagram of e-beam lithography and E-beam Lithography System (ELX-7500)

2.2.2 Mask Alignment and Exposure System

Photolithography (also termed "optical lithography" or "UV lithography") [4] is a process used in microfabrication to selectively remove parts of a thin film or the bulk of a substrate. It uses light to transfer a geometric pattern from a photomask to a light-sensitive chemical "photoresist", or simply "resist," on the substrate. A series of

chemical treatments then either engraves the exposure pattern into, or enables deposition of a new material in the desired pattern upon, the material underneath the photo resist. For example, in complex integrated circuits, a modern CMOS wafer will go through the photolithographic cycle up to 50 times.

Photolithography shares some fundamental principles with photography in that the pattern in the etching resist is created by exposing it to light, either directly (without using a mask) or with a projected image using an optical mask. This procedure is comparable to a high precision version of the method used to make printed circuit boards. Subsequent stages in the process have more in common with etching than with lithographic printing. It is used because it can create extremely small patterns (down to a few tens of nanometers in size), it affords exact control over the shape and size of the objects it creates, and because it can create patterns over an entire surface cost-effectively. Its main disadvantages are that it requires a flat substrate to start with, it is not very effective at creating shapes that are not flat, and it can require extremely clean operating conditions.

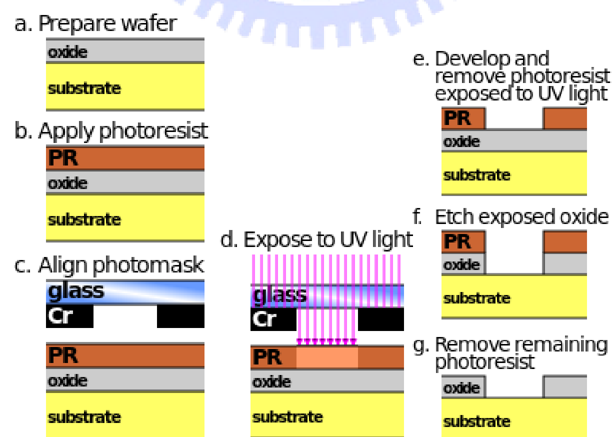

Fig. 2.3 Simplified illustrations of dry etching using positive photoresist during a photolithography process in semiconductor micro-fabrication.

Fig. 2.4 Alignment System (ABM Model 60 DUV/MUV/NearUV)

2.2.3 Plasma-Enhanced Chemical Vapor Deposition (PECVD)

Plasma-enhanced chemical vapor deposition (PECVD) [5] is a process used to deposit thin films from a gas state (vapor) to a solid state on a substrate. Chemical reactions are involved in the process, which occur after creation of a plasma of the reacting gases. The plasma is generally created by RF frequency between two electrodes, the space between which is filled with the reacting gases. Silicon dioxide can be deposited using a combination of silicon precursor gasses like dichlorosilane or silane and oxygen precursors, such as oxygen and nitrous oxide, typically at pressures from a few millitorr to a few torr. Plasma-deposited silicon nitride, formed from silane and ammonia or nitrogen, is also widely used, although it is important to note that it is not possible to deposit a pure nitride in this fashion. Plasma nitrides always contain a large amount of hydrogen. Fig.2.5 shows the Plasma-enhanced chemical vapor deposition system used to deposit SiN_x or SiO_2 as hard mask.

Fig. 2.5 Plasma Enhanced CVD System (SAMCO PECVD Model PD-220)

2.2.4 Electron Beam Physical Vapor Deposition

Electron Beam Physical Vapor Deposition [6] is a form of physical vapor deposition in which a target anode is bombarded with an electron beam given off by a charged tungsten filament under high vacuum. The electron beam causes atoms from the target to transform into the gaseous phase. These atoms then precipitate into solid form, coating everything in the vacuum chamber (within line of sight) with a thin layer of the anode material.

Thin film deposition is a process applied in the semiconductor industry to grow electronic materials, in the aerospace industry to form thermal and chemical barrier coatings to protect surfaces against corrosive environments, in optics to impart the desired reflective and transmissive properties to a substrate and elswhere in industry to modify surfaces to have a variety of desired properties. The deposition process can be broadly classified into physical vapor deposition (PVD) and chemical vapor deposition (CVD). In CVD, the film growth takes place at high temperatures, leading to the formation of corrosive gaseous products, and it may leave impurities in the film. The PVD process can be carried out at lower deposition temperatures and without

corrosive products, but deposition rates are typically lower. Electron beam physical vapor deposition, however, yields a high deposition rate from 0.1 μm / min to 100 μm / min at relatively low substrate temperatures, with very high material utilization efficiency. The schematic of an EBPVD system is shown in Fig. 2.6.

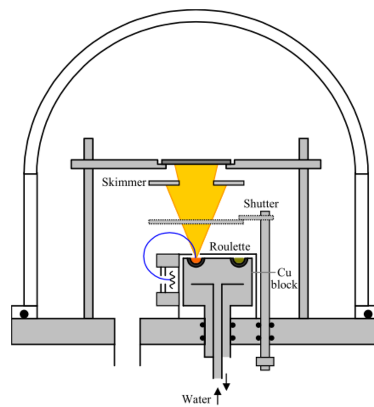

Fig. 2.6 Simplified illustration of e-beam evaporator

Fig. 2.7 Coating system with optical in-situ monitor (KS-800OPTO) and E-gun evaporator (ULVAC EBX-8C)

2.2.5 Dry Etching System

Dry etching process is critical for scientists to fabricate the device according to

their plan, and there are two types of etching processes: wet etching and dry etching. Dry etching process uses plasma to etch the semiconductor material and it is a kind of anisotropic etching process. The line-width of dry etching process is smaller than wet etching, therefore, dry etching process gradually replace wet etching process after 1980.

The mechanism of dry etching process is as follow: first, the etching gas has been diffuse to chamber under ultra-low pressure. Second, when the pressure is stable, plasma is produced by RF frequency. Third, the radicals produced by bombardment of high speed electron would diffuse to the wafer and attach to its surface. Fourth, with the help of ion bombardment, these radicals would react with the atoms on the surface and form by-product as gas. At the end, these volatile by-products would then leave the surface of wafer and discharge from chamber. Fig. 2.8 shows the inductively coupled plasma and reactive ion etching (ICP-RIE) system used to etch Si_3N_4 layer to transfer the patter from PMMA layer, and the ICP-RIE equipment used to etch GaN layer.

Fig. 2.8 ICP-RIE System (Oxford Plasmalab System 100) and ICP-RIE System (SAMCO RIE-101PH).

2.3 Measurement Setups

2.3.1 Four Point Probe

The 4-point probe setup consists of four equally spaced tungsten metal tips with finite radius. Each tip is supported by springs on the other end to minimize sample damage during probing. The four metal tips are part of an auto-mechanical stage which travels up and down during measurements. A high impedance current source is used to supply current through the outer two probes; a voltmeter measures the voltage across the inner two probes (See Fig. 2.9) to determine the sample resistivity. Typical probe spacing is ~ 1 mm.

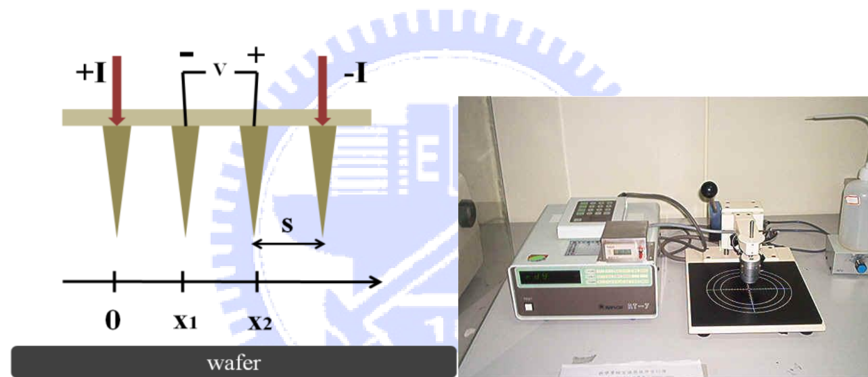

Fig 2.9 Schematic of 4-point probe configuration and Four point probe system (NAPSON RT-7)

2.3.2 Scanning Electron Microscopy (SEM)

Scanning electron microscope (SEM) is one of the most important equipment for people to observe objects in nano-scale. The electrons interact with atoms that make up the sample producing signals that contain information's about itself. Moreover, preparation of the samples for SEM is relatively easy due to the fact that SEM only require the sample to be conductivity. The combination of higher magnification, larger depth of focus, greater resolution, and ease of sample observation makes the SEM becomes one of the most widely used equipment used for commercial and research

purposes. Fig. 2.10 shows the JSM-7000F made by JEOL.

Fig. 2.10 Scanning electron microscope System (JSM-7000F)

2.3.3 Photoluminescence Spectroscopy (PL)

Photoluminescence characterization equipment generally uses the PL method to obtain the wavelength and intensity of the semiconductor material being analyzed. PL is the process of optical absorption of electrons in solids between an initial energy state Ei and a final energy state Ef. Excitation of an electron to Ef will leave Ei

unoccupied creating a hole. Absorption creates electron-hole pairs while luminescence is the process which occurs when electrons in excited states drop to a lower level emitting a photon $\hbar w$ as shown in Fig. 2.11. The electron–hole recombination creates a photon which is also known as a radiative transition. Direct gap materials are good light emitters and their optical properties are analyzed using this technique.

Photons are absorbed using an excitation source which is typically a laser. The frequency of the source $\hbar wL$ must be greater than the energy gap Eg. The result is that electrons are injected into the conduction band and holes into the valence band. Electrons and holes are initially created in higher states within these bands but will rapidly relax to the bottom of their respective bands reaching their lowest energy state. Relaxation occurs by emitting phonons, for energy loses from the higher states,

which obeys the conservation laws. The difference in energy between the two bands is Eg which is the energy gap, also known as the band gap. Luminescence occurs close to the band gap Eg, near k = 0. After excitation, both electrons and holes relax to their lowest energy states by emitting phonons.

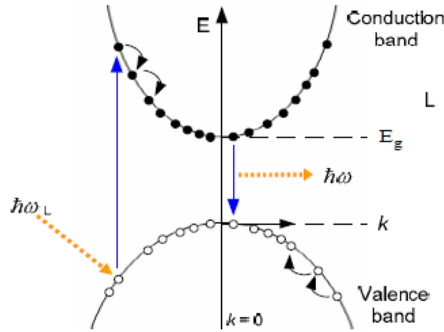

Fig. 2.11 Interband transitions in photoluminescence system

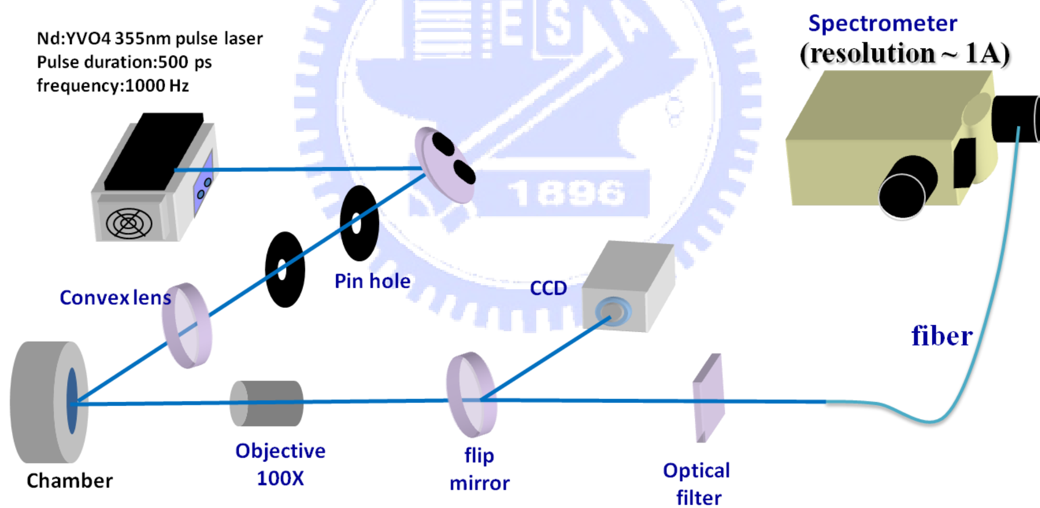

Fig. 2.12 The optical pumping system in experiment Using Nd:YVO4 355 nm pulse laser as pumping source, the pulse width is 0.5 ns, and repetition rate is 1k Hz. The laser light is focused by convex lens and pumped onto the device. Use objective lens to receive the light which emit from the device, and take flip mirror to control the optical path transmitting to CCD or fiber.

2.3.4 Electroluminescence Spectroscopy (EL)

As shown in Fig. 2.13, Electroluminescence (EL) is an optical phenomenon and electrical phenomenon in which a material emits light in response to an electric current passed through it, or to a strong electric field. This is distinct from light emission resulting from heat (incandescence), chemical reaction (chemiluminescence), sound (sonoluminescence), or other mechanical action (mechanoluminescence). Electroluminescence is the result of radiative recombination of electrons and holes in a material (usually a semiconductor). The excited electrons release their energy as photons - light. Prior to recombination, electrons and holes are separated either as a result of doping of the material to form a p-n junction (in semiconductor electroluminescent devices such as LEDs), or through excitation by impact of high-energy electrons which are accelerated by a strong electric field.

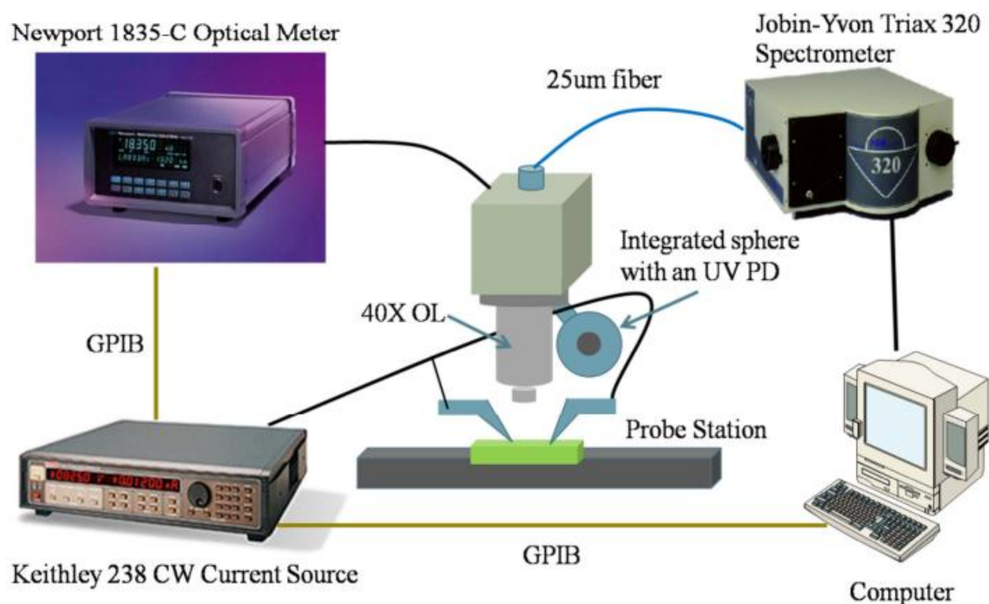

Fig. 2.13 The EL measurement system for electrically driving

2.3.5 Atomic Force Microscope (AFM)

The AFM utilizes a sharp probe moving over the surface of a sample in a raster

scan. In the case of the AFM, the probe is a tip on the end of a cantilever which bends in response to the force between the tip and the sample. The small probe-sample separation (on the order of the instrument's resolution) makes it possible to take measurements over a small area. To acquire an image the microscope raster-scans the probe over the sample while measuring the local property in question.

The resulting image resembles an image on a television screen in that both consist of many rows or lines of information placed one above the other. Unlike traditional microscopes, scanned-probe systems do not use lenses, so the size of the probe rather than diffraction effect generally limits their resolution. As shown in Fig. 2.14 AFM operates by measuring attractive or repulsive forces between a tip and the sample. In its repulsive "contact" mode, the instrument lightly touches a tip at the end of a leaf spring or "cantilever" to the sample. As a raster-scan drags the tip over the sample, some sort of detection apparatus measures the vertical deflection of the cantilever, which indicates the local sample height. Thus, in contact mode the AFM measures hard-sphere repulsion forces between the tip and sample. In tapping mode, the AFM derives topographic images from measurements of attractive forces; the tip does not touch the sample.

The presence of a feedback loop is one of the subtler differences between AFMs and older stylus-based instruments such as record players and stylus profilometers. The AFM not only measures the force on the sample but also regulates it, allowing acquisition of images at very low forces. As shown in Fig. 2.15, the feedback loop consists of the tube scanner that controls the height of the entire sample; the cantilever and optical lever, which measures the local height of the sample; and a feedback circuit that attempts to keep the cantilever deflection constant by adjusting the voltage applied to the scanner. One point of interest: the faster the feedback loop can correct

deviations of the cantilever deflection, the faster the AFM can acquire images; therefore, a well-constructed feedback loop is essential to microscope performance. AFM feedback loops tend to have a bandwidth of about 10 kHz, resulting in image acquisition time of about one minute.

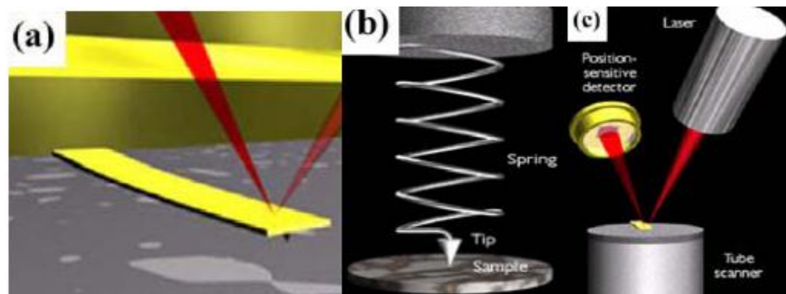

Fig. 2.14 The concepts of AFM and the optical lever: (a) a cantilever touching a sample, (b) illustration of the meaning of "spring constant" as applied to cantilevers, (c) the optical lever. Scale drawing; the tube scanner measures 24 mm in diameter, while the cantilever is 100 μm long typically.

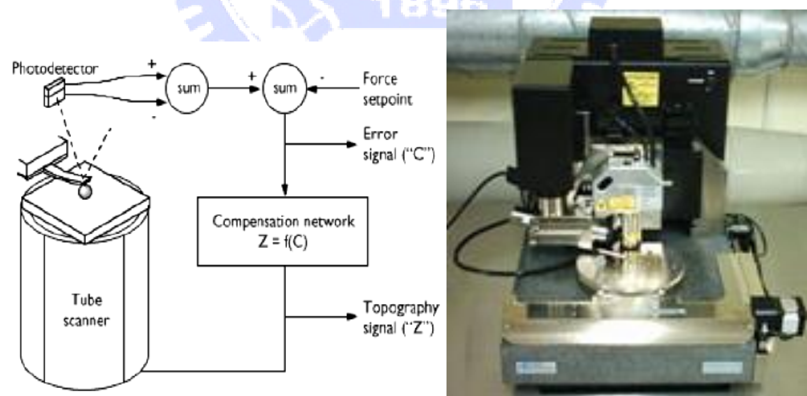

Fig. 2.15 The AFM feedback loop. A compensation network monitors the cantilever deflection and keeps it constant by adjusting the height of the sample. Atomic Force Microscope（D3100）

2.3.6 Others

Fig. 2.16 N&K Surface Profile Analyzer (N&K 1500)

2.4 Fabrication Process Parameters and Techniques

To fabricate GaN-based light emitting devices, there are some useful parameters and techniques used in our experiments regularly. And also those information will be mention and quote in second half of this thesis.

2.4.1 Initial Clean (I.C.)

The purpose of Initial Clean (I.C.) is to remove the small particle and organism on the sample surface. You should do it before each fabrication process. The details parameters are expressed as below:

1. Degreasing particles in acetone (ACE) 5min by ultrasonic baths.
2. Dipping in isopropyl alcohol (IPA) 5min by ultrasonic baths for organism removed.
3. Rising in de-ionized water (D.I. water) 5min for surface clean.
4. Blowing with N_2 gas for surface drying.

2.4.2 Lithography Techniques and Parameters

The purpose of the photolithography is to transfer the pattern of the mask to the photoresist (PR) on the wafer. In our experiments, positive photoresists AZ-6112、AZ-5214E and negative photoresists AZ-2020、AZ-2070 were used. Although AZ-5214E is positive photoresist, it is capable of image reversal (IR) resulting in the effect of negative photoresist. In fact AZ-5214E is almost exclusively used in the IR-mode which is proper to be used in the lift-off process. However, image reversal resists generally do not cross-link. Hence, from approx. 120-130℃ on, the resist structures start to soften. The solution is AZ-2020 which has approximate thickness and stronger mechanical properties. AZ-2070 is used when we need extreme thickness photoresist mask. Notice that hard bake 120 ^{o}C 5min can be applied when dry etching is the following process. Those photolithography techniques are described as below：

AZ-6112 positive exposure

Initial Clean	
Dehydration Bake	120 ^{o}C 5min
Spin coating	1000rpm/10sec, 3000rpm/30sec (thickness ~2μm)
Soft bake	90 ^{o}C 90sec
Edge bead removal	Polyester swab moisten with ACE.
Alignment and exposure	1.9sec ~ 2.2sec
Development	Dip in AZ-300 30sec、Water 30sec
Post check	OM.
Hard bake	120 ^{o}C 5min (optional)

AZ-5214E image reverse exposure

Initial Clean	
Dehydration Bake	120 °C 5min
Spin coating	1000rpm/10sec, 3000rpm/30sec (thickness ~1.6μm)
Soft bake	90 °C 90sec
Edge bead removal	Polyester swab moisten with ACE.
Alignment and exposure	2.8sec ~ 3 sec
Reversal bake	120 °C 120sec
Flood exposure	11sec ~ 13sec
Development	Dip in AZ-300 40sec、Water 30sec
Post check	OM.
Hard bake	120 °C 5min (optional)

AZ-2020 negative exposure

Initial Clean	
Dehydration Bake	120 °C 5min
Spin coating	1000rpm/10sec, 1500rpm/35sec (thickness 2 ~3μm)
Soft bake	110 °C 60sec
Edge bead removal	Polyester swab moisten with ACE.
Alignment and exposure	100mJ/cm2
Post bake	110 °C 60sec

Development	Dip in AZ-300 120sec、Water 30sec
Post check	OM.
Hard bake	120 ^{o}C 5min (optional)

AZ-2070 negative exposure

Initial Clean	
Dehydration Bake	120 ^{o}C 5min
Spin coating	1000rpm/10sec, 2200rpm/30sec (thickness 6~7μm)
Soft bake	110 ^{o}C 120sec
Edge bead removal	Polyester swab moisten with ACE
Alignment and exposure	16sec ~ 19sec
Post bake	110 ^{o}C 140sec
Development	Dip in AZ-300 120sec、Water 30sec
Post check	OM.
Hard bake	120 ^{o}C 5min (optional)

2.4.3 PECVD Deposition Techniques and Parameters

The purpose of PECVD technique is to deposit a Si_3N_4 film for hard mask. The details of PECVD parameters are as shown below：

Si_3N_4 film deposition (SAMCO PD220)

SiH_4/Ar: 20sccm	Temperature: 300 ^{o}C	Rate: 9.6nm/min
NH_3: 10sccm	RF power: 35W	

N_2: 490sccm	Pressure: 100Pa	

<u>SiO_2 film deposition (OXFORD INSTRUMENTS Plasmalab80Plus)</u>

SiH_4: 9sccm	Temperature: 300 ^{o}C	Rate: 81nm/min
N_2O: 710sccm	RF power: 25W	
	Pressure: 1000mTorr	

2.4.4 Dry Etching Techniques and Parameters

Dry etching provide anisotropic etching extensively used in mask transferation. Noticed that dry etching also cause critical sidewall roughness. The ICP-RIE parameters are as shown below：

<u>Si_3N_4 film etching (Oxford Plasmalab system 100)</u>

Ar/O_2: 5sccm	Temperature: 20℃	Rate: 90nm/min
CHF_3: 50sccm	RF power: 150W	
	Pressure: $7.5*10^{-9}$Torr	

<u>GaN film etching (SAMCO RIE-101PH)</u>

Ar: 20sccm	Temperature: 20℃	Rate: 660nm/min
Cl_2: 40sccm	ICP power: 200W Bias power: 200W	
	Pressure: 0.49Pa	

2.4.5 Polish techniques

Diamond lapping films usually used in polishing fiber optic connectors. The mineral key on films make from aluminum oxide or diamond which supperizely has good perfomace in elimitating the GaN surface roughness caused by dry etching .

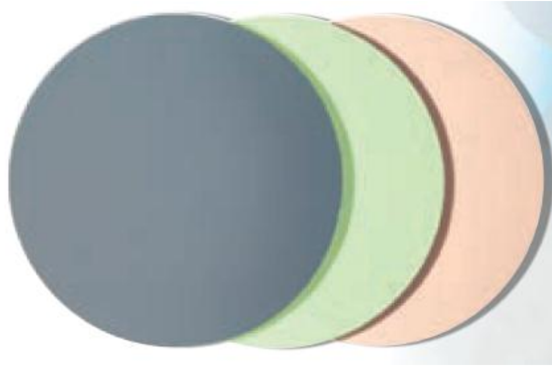

Fig. 2.17 Photography of diamond lapping films

2.4.6 Lift-off techniques with photoresists

Beside wet or dry etching, lift-off is a common technique to pattern metal or dielectrica films in the µm or sub-µm range. The main criteria for the choice of a photoresist best-suited for a certain lift-off process are:,,

- The thickness of the coated material
- The coating technology (evaporation, sputtering, CVD, ...) and the maximum temperature the resist film has to stand during coating
- The required resolution

Generally, the thickness of photoresist has to be three times thicker than the coating film and can be remove easily by ACE with ultrasonic vibration in several minutes at room temperature. For some difficult cases, the used of thicker photoresist、PR stripper、higher solvent temperature、strogher ultrasonic intensity can accelerate lift-off process.

Reference

[1] http://en.wikipedia.org/wiki/Transfer-matrix_method_%28optics%29

[2] Born, M.; Wolf, E., Principles of optics: electromagnetic theory of propagation, interference and diffraction of light. Oxford, Pergamon Press, 1964.

[3] http://optical-waveguides-modeling.net/index.jsp

[4] http://en.wikipedia.org/wiki/Photolithography

[5] http://en.wikipedia.org/wiki/Plasma-enhanced_chemical_vapor_deposition

[6] http://en.wikipedia.org/wiki/Electron_beam_physical_vapor_deposition

Chapter 3

An AlN Layer for the Current Confinement in GaN-Based VCSELs with Two Dielectric Distributed Bragg Reflectors

3.1 Operation principle of VCSELs

3.1.1 Fabry–Pérot cavity

The most common types of optical cavities consist of two facing plane (flat) or spherical mirrors [1]. The simplest of these is the plane-parallel or Fabry–Pérot cavity, consisting of two opposing flat mirrors. In basics of laser physics a laser cavity where a propagating mode has to be stationary inside the cavity to form a laser as shows in Fig. 3.1. Mathematically this means that a complex field amplitude, E_0 at an arbitrary location inside the cavity has to return to the original value after a round trip propagation and twice of reflections at the two-end facets, or

$$r_1 r_2 \exp\{2ikL\} E_0 = E_0 \tag{3.1}$$

where r_1 , r_2 ,k are amplitude reflectivities of the two facets and complex propagation constant, respectively. Splitting Equation above into real and imaginary parts leads to following two equations ($k = k'+k''$):

$$L = \frac{\ln(r_1 r_2)}{2k''} \tag{3.1}$$

$$L = \frac{\lambda}{2n_{neff}} m,\ m = 1,2, \ldots \tag{3.2}$$

By Eq. 3.2 and mathematical derivation, the mode spacing can be given as

$$\Delta\lambda = \frac{\lambda^2}{2n_{neff}L} \tag{3.3}$$

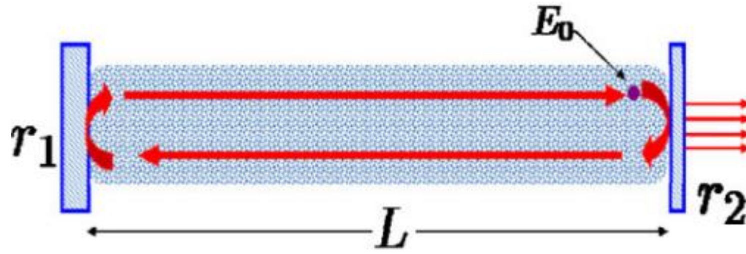

Fig. 3.1 Schematic of a laser cavity showing the length, L, and reflection coefficients of the two-end facets, r_1 and r_2.

3.1.2 Characteristics of Distributed Bragg reflectors (DBR)

Distributed Bragg reflectors (DBR) serve as high reflecting mirror in numerous optoelectronic and photonic devices such as VCSEL. There are many methods to analyze and design DBRs, and the matrix method is one of the popular one. The calculations of DBRs are entirely described in many optics books, and the derivation is a little too long to write in this thesis. Hence, we put it in simple to understand DBRs. Consider a distributed Bragg reflector consisting of m pairs of two dielectric, lossless materials with high- and low- refractive index n_H and n_L, as shown in Fig. 3.2 The thickness of the two layers is assumed to be a quarter wave, that is, $L_1 = \lambda_B/4n_H$ and $L_2 = \lambda_B/4n_L$, where the λ_B is the Bragg wavelength.

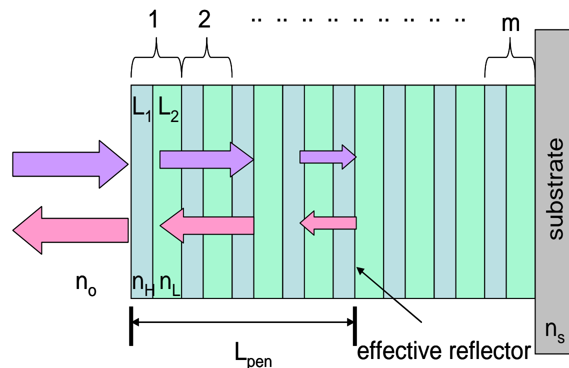

Fig. 3.2 Schematic diagrams of DBRs

Multiple reflections at the interface of the DBR and constructive interference of the multiple reflected waves increase the reflectivity with increasing number of pairs. The reflectivity has a maximum at the Bragg wavelength λ_B. The reflectivity of a DBR with m quarter wave pairs at the Bragg wavelength is given by

$$R = \left(\frac{1 - \frac{n_s}{n_o}(\frac{n_L}{n_H})^{2p}}{1 + \frac{n_s}{n_o}(\frac{n_L}{n_H})^{2p}} \right) \tag{3.4}$$

where the n_o and n_s are the refractive index of incident medium and substrate.

The high-reflectivity or stop band of a DBR depends on the difference in refractive index of the two constituent materials, Δn (n_H-n_L). The spectral width of the stop band is given by

$$\Delta\lambda_{stopband} = \frac{2\lambda_B \Delta n}{\pi n_{eff}} \tag{3.5}$$

where neff is the effective refractive index of the mirror. It can be calculated by requiring the same optical path length normal to the layers for the DBR and the effective medium. The effective refractive index is then given by

$$n_{eff} = 2(\frac{1}{n_H} + \frac{1}{n_L})^{-1} \tag{3. 6}$$

The length of a cavity consisting of two metal mirrors is the physical distance between the two mirrors. For DBRs, the optical wave penetrates into the reflector by one or several quarter-wave pairs. Only a finite number out of the total number of quarter-wave pairs are effective in reflecting the optical wave. The effective number of pairs seen by the wave electric field is given by

$$m_{eff} \approx \frac{1}{2}\frac{n_H + n_L}{n_H - n_L}\tanh(2m\frac{n_H - n_L}{n_H + n_L}) \tag{3.7}$$

For very thick DBRs (m→∞) the tanh function approaches unity and one obtains

$$m_{eff} \approx \frac{1}{2}\frac{n_H + n_L}{n_H - n_L} \tag{3.8}$$

Also, the penetration depth is given by

$$L_{pen} = \frac{L_1 + L_2}{4r}\tanh(2mr) \tag{3.9}$$

Where r = (n1-n2)/ (n1+n2) is the amplitude reflection coefficient. L_1 and L_2 are the thickness of each DBR layer. For a large number of pairs (m→∞), the penetration depth is given by

$$L_{pen} \approx \frac{L_1 + L_2}{4r} = \frac{L_1 + L_2}{4}\frac{n_H + n_L}{n_H - n_L} \tag{3.10}$$

Comparison of Eq. (3.8) and Eq. (3.10)

$$L_{pen} = \frac{1}{2}m_{eff}(L_1 + L_2) \tag{3.11}$$

The factor of (1/2) in Eq. (3.11) is due to the fact that meff applies to effective number of periods seen by the electric field whereas Lpen applies to the optical power. The optical power is equal to the square of the electric field and hence it penetrates half as far into the mirror. The effective length of a cavity consisting of two DBRs is thus given by the sum of the thickness of the center region plus the two penetration depths into the DBRs.

3.1.3. Quality factor (Q)

Since the theory of Fabry-Perot cavity has been explained, we can talk about the finesse and the quality factor of resonant cavity. The cavity finesse, F, is defined as the ratio of the transmittance peak seperation (Δψ) to the transmittance full-width at half-maximum (δψ):

$$F = \frac{\Delta\phi}{\delta\phi} = \frac{\pi}{2\phi_{1/2}} = \frac{\pi}{1 - \sqrt{R1R2}} \tag{3.12}$$

Fig. 3.3 shows the transmission pattern of a Fabry-Perot cavity in frequency domain.

The finesse of the cavity in the frequency is then given by F = νFSR/Δν. Besides the quality factor Q is also equal to λ/δλ, where δλ is the narrow emission linewidth around λ.

$$Q = \frac{\lambda}{\delta\lambda} \tag{3.13}$$

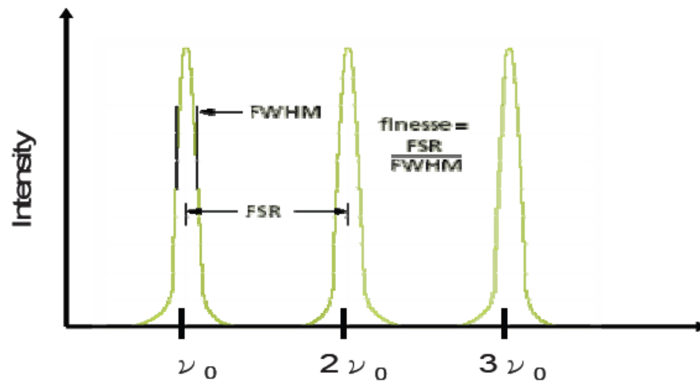

Fig. 3.3 transmission pattern of a Fabry-Perot cavity in frequency domain

3.1.4 Transverse mode

The nature of the transverse optical confinement determines the possible lateral optical modes that might lase. Although VCSELs tend to lase in only a single axial mode , because the DBR mirrors fill much of the cavity, lateral modes can exist for device diameters down to led than a micro. The losses explicitly discussed above were those of the fundamental lateral mode, although the general discussion may be applied to losses for higher-order modes as well. In fact, the higher-order modes tends to experience higher size-dependent optical losses than the fundamental mode, and this is why it is possible to observe single-mode operation in devices that have diameters of several microns

The transverse mode of gain-guided structures tends to vary with pumping level and

thermal environment, and they are rather difficult to analyze analytically. However, the lateral modes of more strongly index-guided VCSELs with etched mesas or graded index dielectric waveguides, provided the Fresnel number is sufficiently large(F~10) so that significant diffraction does not occur in unguided sections. Then, the modes can be determined from normalized dispersion charts, generally used for optical fibers. In both the etched-mesa and dielectrically aperture cases, the effective lateral index profile can be determined by dividing the net change in optical path length over the cavity length by the cavity length. Thus, the assumed uniform waveguide has a lateral index roll-off given by

$$\delta n_1 = -\frac{\varphi_0(r)\lambda}{2\pi L} = -(n_o - n_{de})\zeta_{de}(r)t(r)/L \qquad (3.14)$$

For a step index resulting from an abrupt dielectric aperture or an etched mesa, the aperture thickness $t\,(\,r < a\,) = 0$ and $t\,(\,r > a\,) = t$. For the etched-mesa VCSEL, t is taken to be L_{eff2} if the etch extends just through the top DBR mirror. For a tapered aperture, $t\,(\,r\,)$ varies with radius.

The change in the optical path length between the aperture and unapertured regions of the device gives rise to change in the longitudinal resonant wavelength with radius. The shift of the mode due to a change in a physical length, it can be applied general form:

$$\Delta\lambda(r) = \lambda\frac{\delta n_1(r)}{n_0} \qquad (3.15)$$

Determine the effective lateral index step is also possible, though it will not work if the shift becomes large than the longitudinal mode spacing or the mirror stop-band.

3.1.5 Carrier density rate equation

The carrier density in the active region is governed by a dynamic process. In fact,

we can compare the process of establishing a certain steady-state carrier density in the active region to that of establishing a certain water level in a reservoir which is being simultaneously filled and drained. This is shown schematically in Fig. 3.4 As we proceed, the various filling (generation) and drain (recombination) terms illustrated will be defined. The current leakage illustrated in Fig. 3.4 contributes to reducing η i and is created by possible shunt paths around the active region. The carrier leakage, R l, is due to carriers "splashing" out of the active region (by thermionic emission or lateral diffusion if no lateral confinement exists) before recombining. Thus, this leakage contributes to a loss of carriers in the active region that could otherwise be used to generate light.

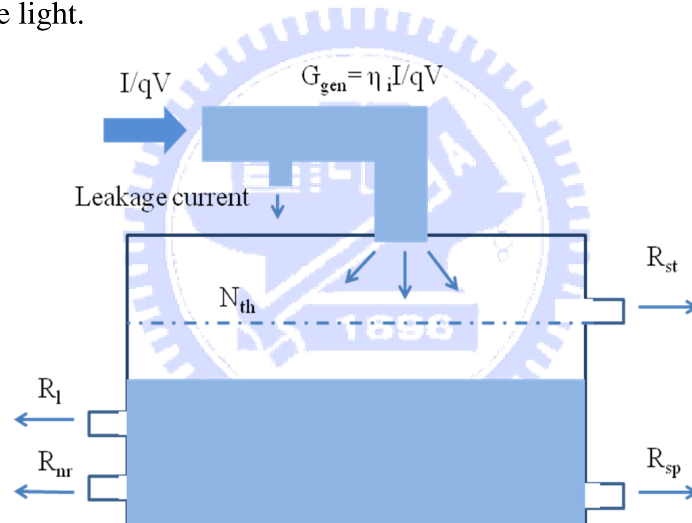

Fig. 3.4 Reservoir with continuous supply and leakage as an analog to a DH active region with current injection for carrier generation and radiative and nonradiative recombination

For the DH active region, the injected current provides a generation term, and various radiative and non-radiative recombination process as well as carrier leakage provide recombination terms. Thus, we can write the carrier density rate equation,

$$\frac{dN}{dt} = G_{gen} - R_{r} \quad (3.16)$$

where N is the carrier density (electron density), G_{gen} is the rate of injected electrons and R_{rec} is the ratio of recombining electrons per unit volume in the active region. Since $\frac{\eta_i I}{q}$ are electrons per second being injected into the active region, $G_{gen} = \frac{\eta_i I}{qV}$, where V is the volume of the active region. The recombination process is complicated and several mechanisms must be considered. Such as, spontaneous recombination rate, $R_{sp} \sim BN^2$, non-radiative recombination rate, R_{nr}, carrier leakage rate, R_l, ($R_{nr} + R_l = AN+CN^3$), and stimulated recombination rate, R_{st}. Thus we can write $R_{rec} = R_{sp} + R_{nr} + R_l + R_{st}$. Besides, $N/\tau \equiv R_{sp} + R_{nr} + R_l$, where τ is the carrier lifetime. Therefore, the carrier density rate equation could be expressed as

$$\frac{dN}{dt} = \frac{\eta_i I}{qV} - \frac{N}{\tau} - R_{st} \quad (3.17)$$

3.1.6 Photon density rate equation

Now, we describe a rate equation for the photon density (N_p), which includes the photon generation and loss terms. The photon generation process includes spontaneous recombination (R_{sp}) and stimulated recombination (R_{st}), and the main photon generation term of laser above threshold is R_{st}. Every time an electron-hole pair is stimulated to recombine, another photon is generated. Since, the cavity volume occupied by photons, V_p, is usually larger than the active region volume occupied by electrons, V, the photon density generation rate will be $[V/V_p]R_{st}$ not just R_{st}. This electron-photon overlap factor, V/V_p, is generally referred to as the confinement factor (Γ). Sometimes it is convenient to introduce an effective thickness (d_{eff}), width (w_{eff}), and length (L_{eff}) that contains the photons. That is, $V_p=d_{eff}w_{eff}L_{eff}$. Then, if the active region has dimensions, d, w, and L_a, the confinement factor can be expressed as,

$\Gamma=\Gamma_x\Gamma_y\Gamma_z$, where $\Gamma_x = d/d_{eff}$, $\Gamma_y = w/w_{eff}$, $\Gamma_z = L_a/L_{eff}$. Photon loss occurs within the cavity due to optical absorption and scatting out of the mode, and it also occurs at the output coupling mirror where a portion of the resonant mode is usually couple to some output medium. These net losses can be characterized by a photon (or cavity) lifetime (τ_p). Hence, the photon density rate equation takes the form

$$\frac{dN_p}{dt} = \Gamma R_{st} + \Gamma\beta_{sp}R_{sp} - \frac{N_p}{\tau_p} \tag{3.18}$$

where β_{sp} is the *spontaneous emission factor*. As to R_{st}, it represents the photon-stimulated net electron-hole recombination which generates more photons. This is a gain process for photons. It is given by

$$\left(\frac{dN_p}{dt}\right)_{gen} = R_{st} = \frac{\Delta N_p}{\Delta t} = v_g g N_p \tag{3.19}$$

where v_g is the group velocity and g is the gain per unit length.

Now, we rewrite the carrier and photon density rate equations

$$\frac{dN}{dt} = \frac{\eta_i I}{qV} - \frac{N}{\tau} - v_g g N_p \tag{3.20}$$

$$\frac{dN_p}{dt} = \Gamma v_g g N_p + \Gamma\beta_{sp}R_{sp} - \frac{N_p}{\tau_p} \tag{3.21}$$

3.1.7 Threshold gain

In order for a mode of the laser to reach threshold, the gain in the active section must be increased to the point when all the propagation and mirror losses are compensated. Most laser cavities can be divided into two general sections: an active section of length L_a and a passive section of length L_p. For a laser, at the threshold, the gain is equal whole loss in the cavity, which includes cavity absorption and mirror loss. For convenience the mirror loss term is sometimes abbreviated as, $\alpha_m \equiv (1/2L)$

$ln(1/R_1R_2)$. Noting that the cavity life time (photon decay rate) is given by the optical loss in the cavity, $1/\tau_p = 1/\tau_i + 1/\tau_m = v_g(\alpha_i + \alpha_m)$. Thus, the threshold gain in the steady state can be expressed with following equation

$$\Gamma g_{th} = \alpha_i + \alpha_m = \frac{1}{v_g \tau_p} = \alpha_i + \frac{1}{2L} \ln\left(\frac{1}{R_1 R_2}\right) \tag{3.22}$$

where α_i is the average internal loss which is defined by $(\alpha_{ia}L_a + \alpha_{ip}L_p)/L$ (i.e.,$\alpha_{ia}L_a$ and $\alpha_{ip}L_p$ are loss of active region and passive section, respectively), and R_1 and R_2 is the reflectivity of top and bottom mirror of the laser cavity, respectively.

3.2 Fabrication flowchart

3.2.1 Simplified flowchart of fabrication

The whole device schematic is as shown in Fig. 3.5.

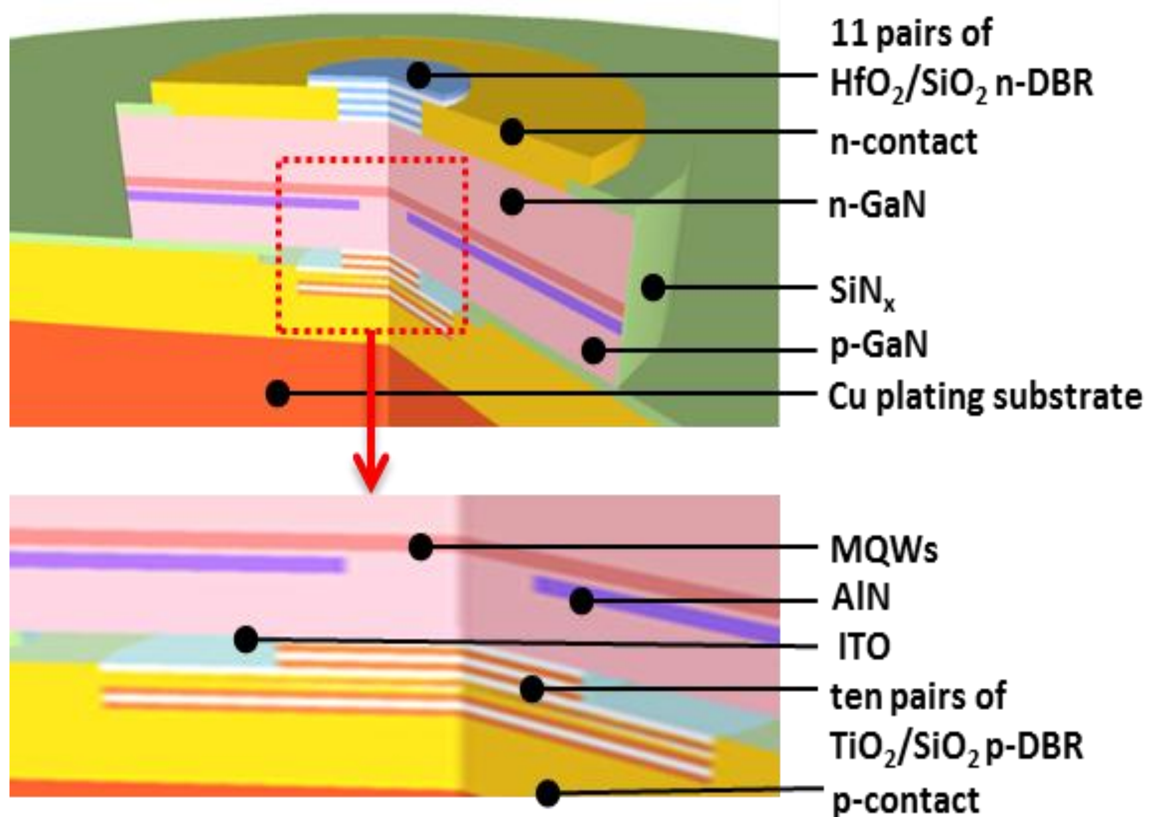

Fig. 3.5 Overall schematic of a GaN-based VCSEL with two dielectric DBRs and an AlN layer.

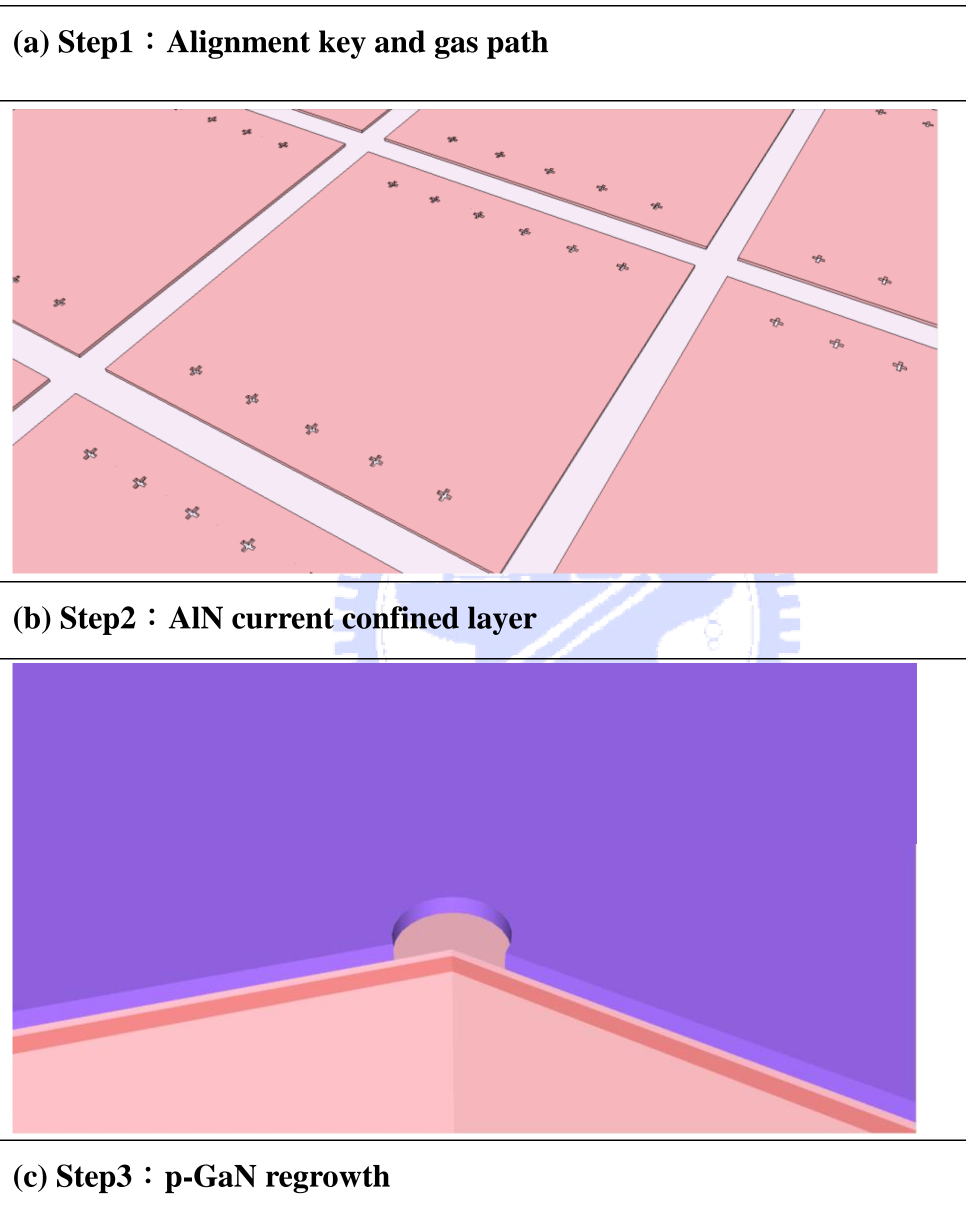

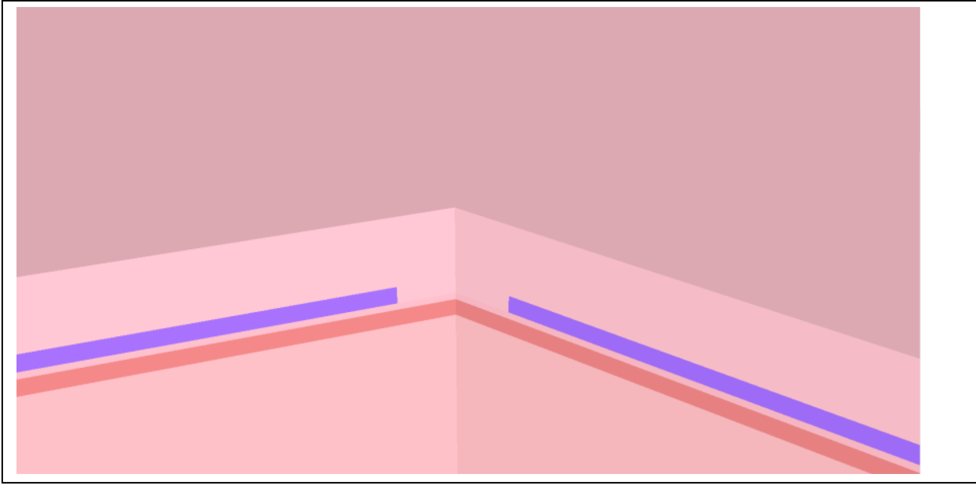

(d) Step4：SiO_2 current confinement layer

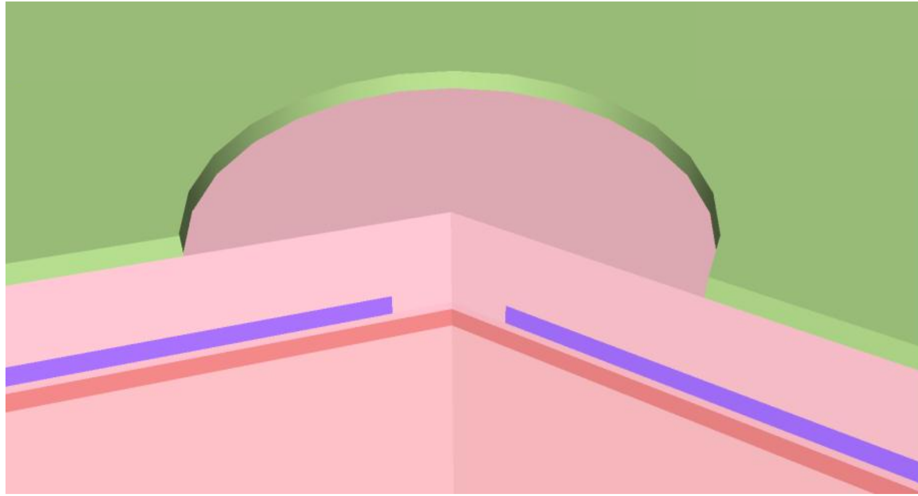

(e) Step5：ITO layer

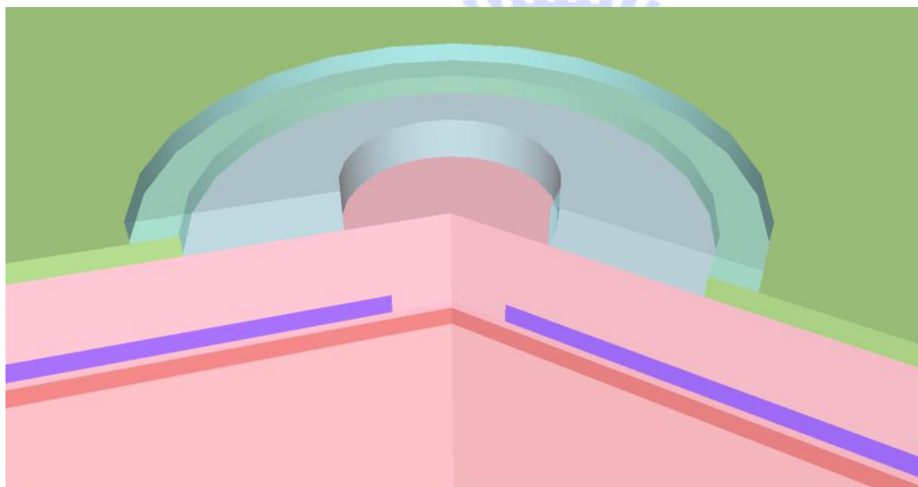

(f) Step6：TiO_2/SiO_2 p-side DBR

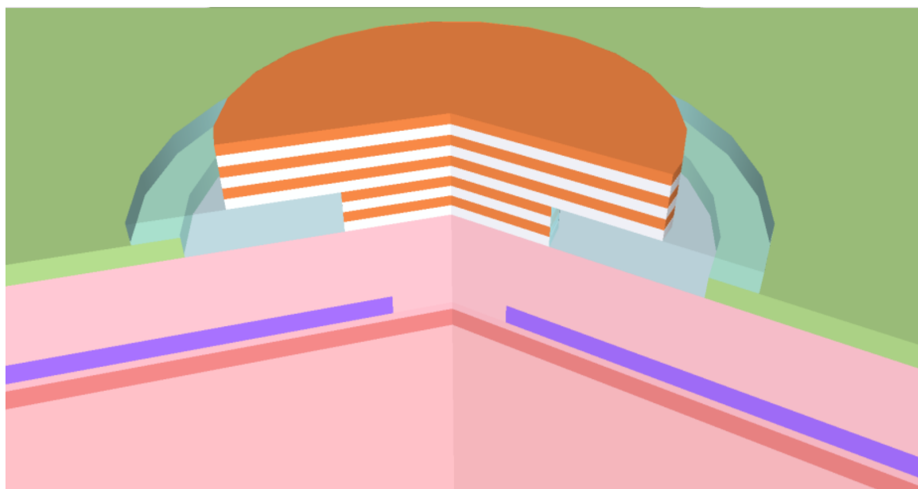

(g) Step7：Cr/Pt/Au p-contact layer

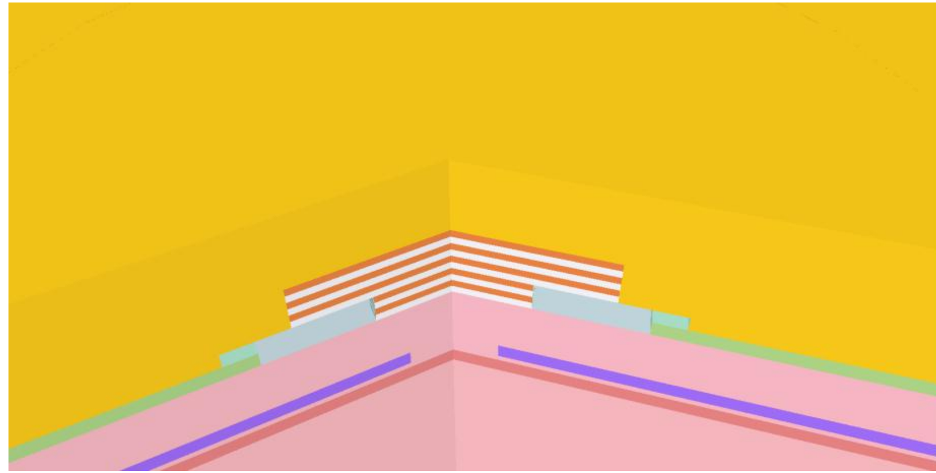

(h) Step8：Cu plating as new substrate

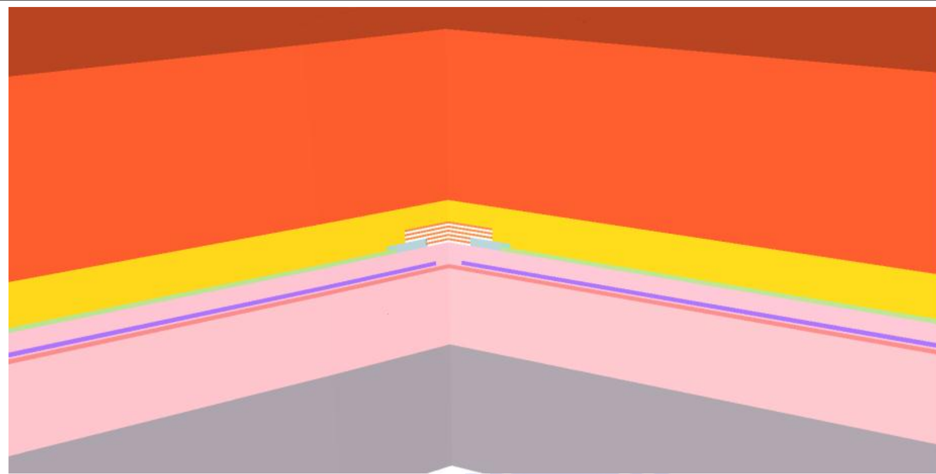

(i) Step9：Laser lift-off the sapphire substrate

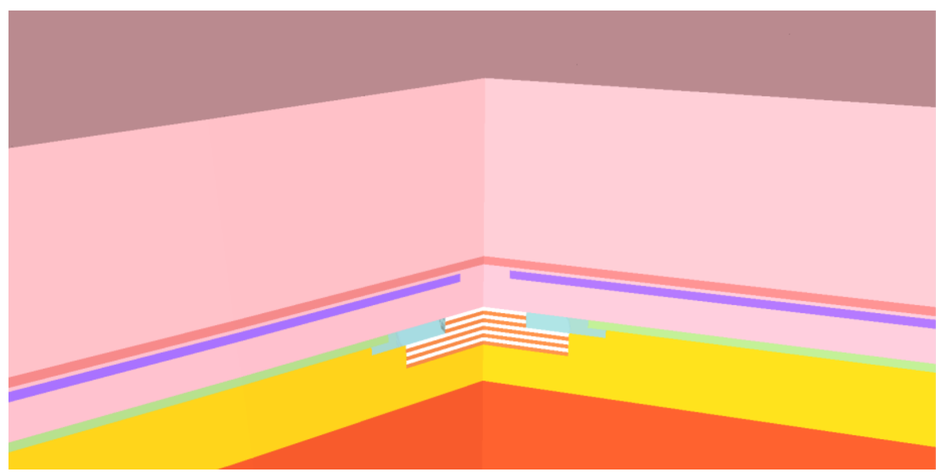

(j) Step10：Dry etching control vertical size Step11：Reduce roughness by polish
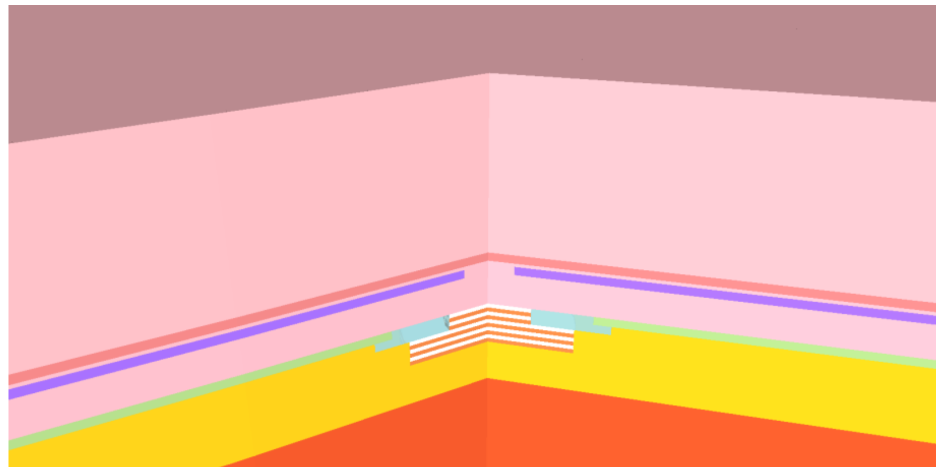
(k) Step12：Isolate each laser structure
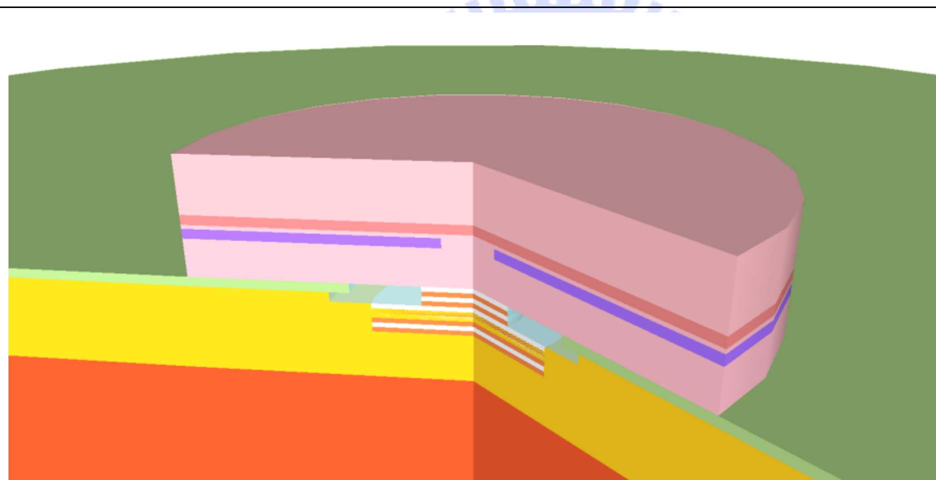
(l) Step13：SiO2 passivation layer
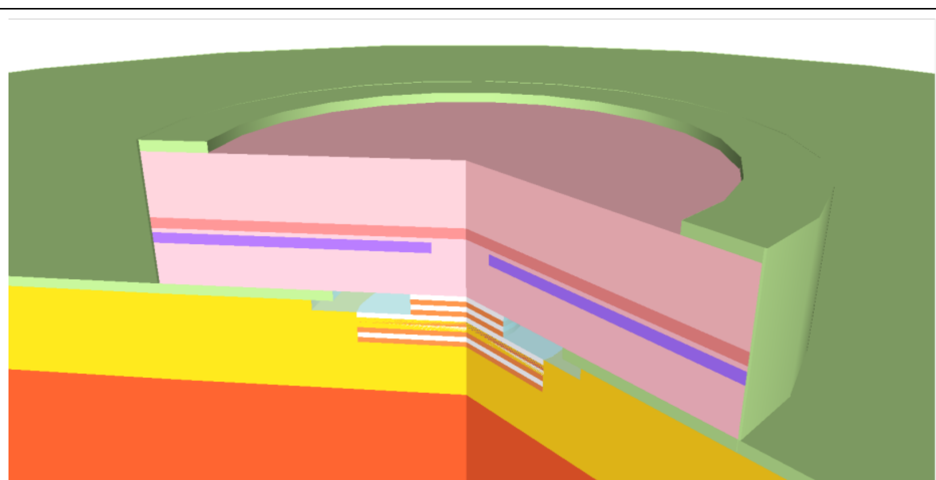

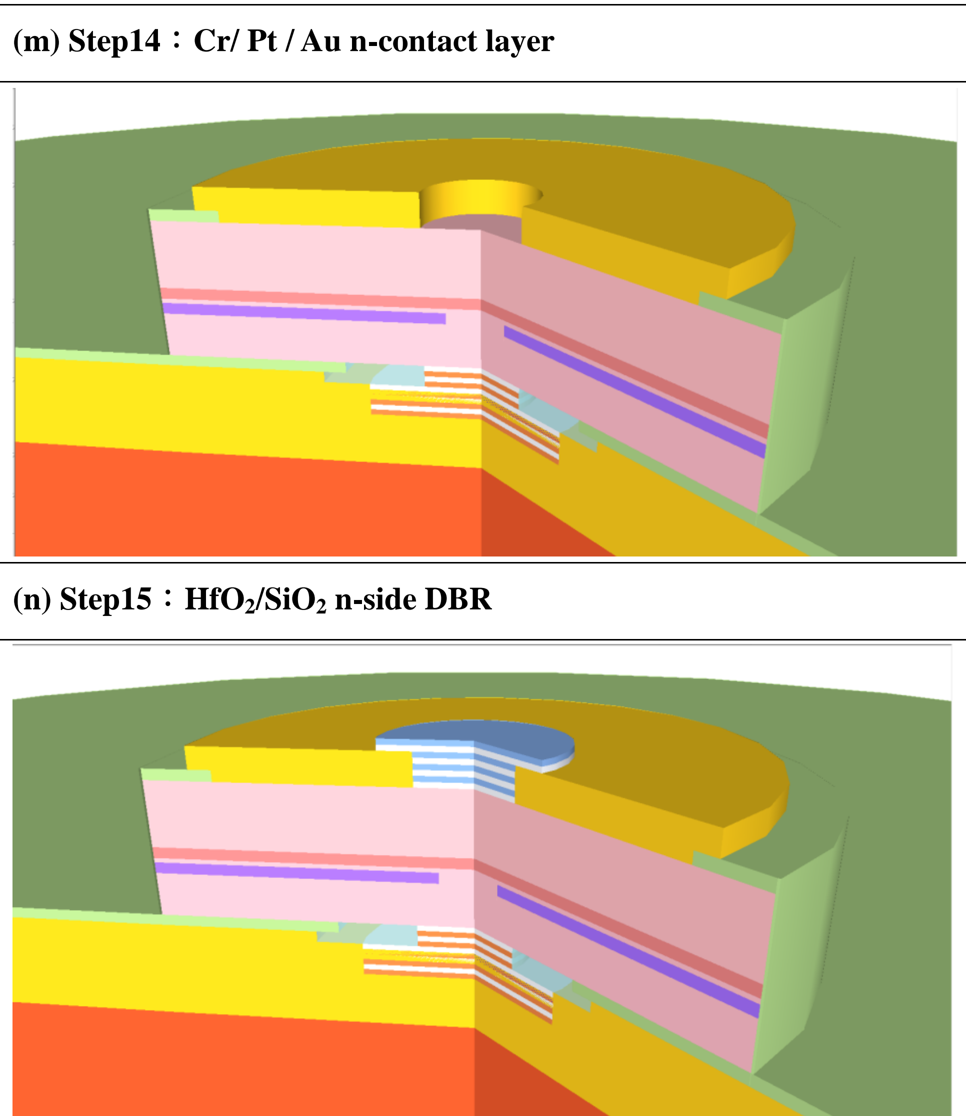

Fig. 3.6 Process flow chart of VCSELs from (a) to (n).

To completely describe the process flowchart, the reasons and the conditions for each processes and data from middle inspect data are entirely described in the next section.

3.2.2 Detailed fabrication process

Step1：Alignment key and gas path (Fig. 3.6 (a))

At the beginning, we had to etch the "large" mesa to make an alignment key,

which would be the position of laser beam and used to control the laser intensity in the process of laser lift-off. The mesa pattern is square and 1200 μm in length and width. The isolation in this step should be done completely to ensure that sapphire substrate will be laser lift-off successfully. The path is etched deeply to let the reactive gas exhaust. As shown in Fig. 3.7, incomplete isolation lead to GaN material be lifted off by the gas generated from laser liftoff process. We used the AZ nLof 2070 thick photolithography techniques to form the mask which had enough thickness to protect the mesa region until n-GaN and u-GaN materials was dry etched entirely.

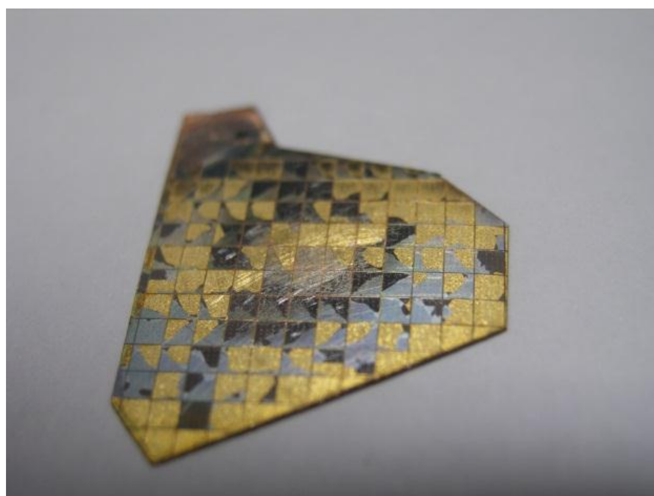

Fig. 3.7 Photography of VCSELs with incomplete isolation and surface were destroyed after laser liftoff. Silver regions are GaN material and yellow regions are contact metal which original covered by GaN but now exposed to air.

Step2：AlN current confined layer (Fig. 3.6 (b))

The AlN layer epitaxial flowchart is fabricated with five steps. In the beginning, SiO_2 hard mask (Fig. 3.8) is used to define the current aperture. The SiO_2 was grown by PECVD and then patterned by the photolithography technique to define the current confinement layer with the effective current aperture varying from 5 μm to 20 μm.

After the process, the surface with and without AlN materials are as shown in Fig. 3.9. And 30 nm、50 nm、70 nm three different thickness for the AlN layer were used.

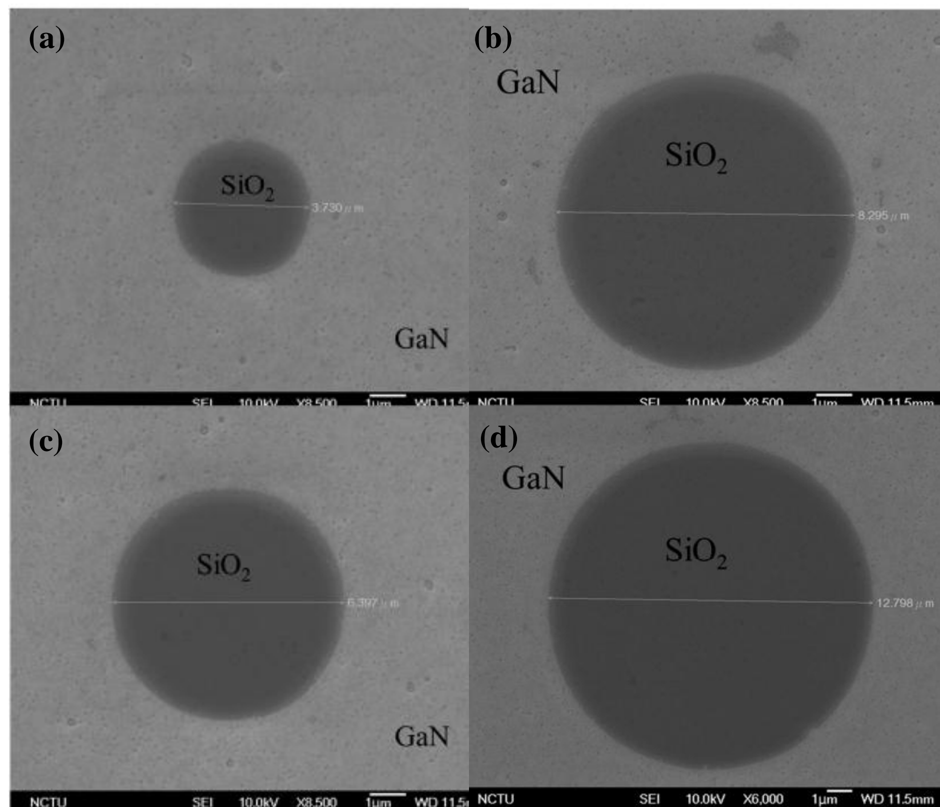

Fig. 3.8 SEM image of different apertures of SiO2 mask (a) 5 μm (b) 8μm (c) 10μm (d) 15μm

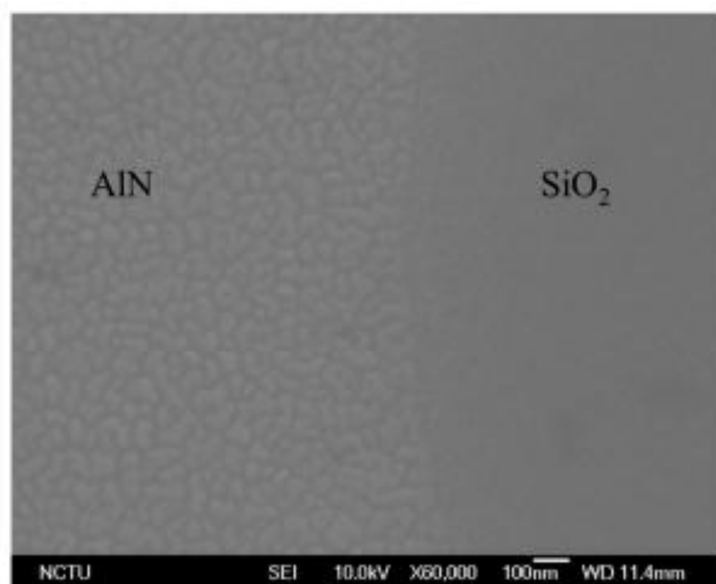

Fig. 3.9 SEM image of the SiO2 mask and the regrowth AlN layer

Step3：p-GaN regrowth (Fig. 3.6 (c))

P-GaN was regrowth on the AlN layer. We growth around 186 nm p-GaN. By OM check several 70nm AlN layer samples. There are no cracks or boundaries on the p-GaN surface which means that p-GaN thickness is enough to sew up the 20 μm AlN aperture. For the same reason, 30nm and 50nm AlN layer samples could be considered successes.

Step4：SiO_2 current coffined layer (Fig. 3.6 (d))

The 500 nm SiO_2 layer was deposited by PECVD and patterned by the photolithography technique. After that, we defined the current injection apertures by dry etching and BOE wet etching. By doing this way, we could avoid the undercut due to using the wet etching alone, which may have serious effect on the pattern size. The SiO_2 pattern is circular and 60 μm in diameter

Step5：ITO layer (Fig. 3.6 (e))

The ITO patterns were defined by the photolithography technique. Then the 180nm ITO layer metal was deposited by sputter and wet etched by oxalic acid dehydrate. The ITO was annealed at 400 degree and 5 minutes, then did circuit transmission line model (CTLM) measurements to complete this step. The ITO pattern has ring shape and 70 μm in outer diameter. The inner diameters vary from 15μm to 30 μm.

Step6：TiO_2/SiO_2 p-side DBR (Fig. 3.6 (f))

The 10 pairs of TiO_2 /SiO_2 p-DBRs stack were deposited by E-gun system and lifted off by AZ nL of 2070 thick PR. The reflection spectrum of p-DBR was exhibited in Fig. 3.10. The stopband is very wide and the reflectivity is higher than 99.5 %. The p-DBR pattern is circular and 40 μm in diameter

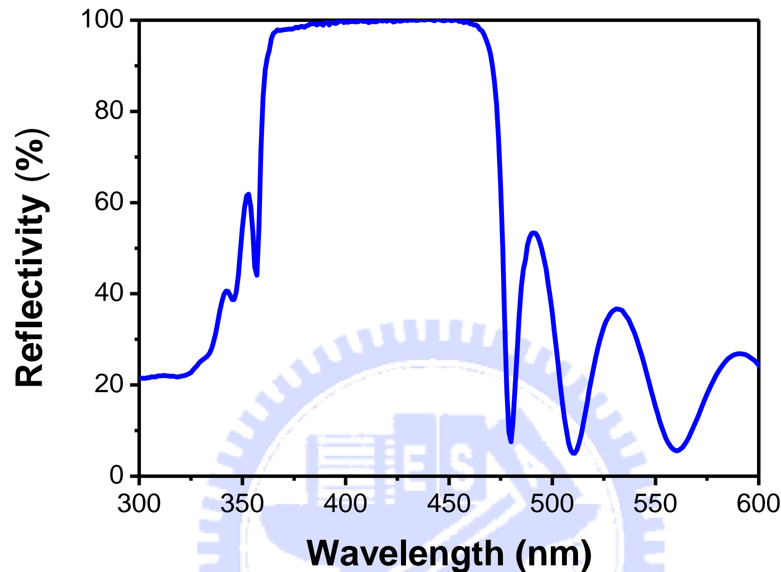

Fig. 3.10 The reflection spectrum of 10 pairs of TiO_2 /SiO_2 p-DBR

Step7：Cr/Pt/Au p-contact layer (Fig. 3.6 (g))

Deposited the p-contact metal on the samples. The p-contact metal was composed of chromium 50 nm, platinum 50 nm, gold 1.9 μm. After that we polish the sapphire substrate as show in Fig. 3.11

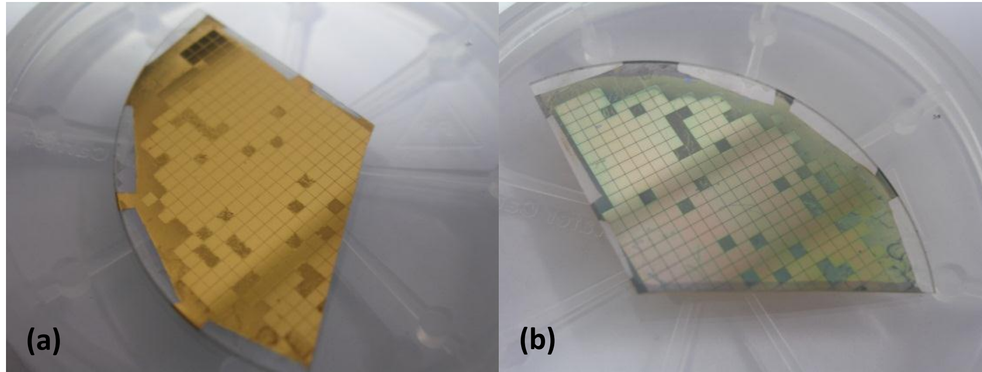

Fig. 3.11 Photography of VCSELs with p-contact layer and sapphire polish (a) front side (b) back side.

<u>Step8：Cu plating as new substrate (Fig. 3.6 (h))</u>

Copper has good heat dissipation and conductivity. Plating the copper around 100 μm and thin gold as the new substrate and protect layer.

<u>Step9：Laser lift-off the sapphire substrate (Fig. 3.5 (i))</u>

First, we prepare the samples by polishing the sapphire substrate for the KrF excimer laser spot alignment and centralization. We use 355nm pulse laser pumped the sample from polished sapphire substrate (Fig. 3.12). As shown in Fig. 3.12, the dominate wavelength and FWHM are 410nm and 15nm. Clear Fabry–Pérot modes are observed in the spectrum. The longitude mode spacing around 5nm which coincide the estimated cavity length is 6.6 μm which is reasonable. Because that the accurate cavity length has to include gain media length and penetration depth in both p-DBR and sapphire. In our case the epitaxial is at least 4.3 μm (4μm n-GaN, 145nm QWs, 186nm p-GaN)

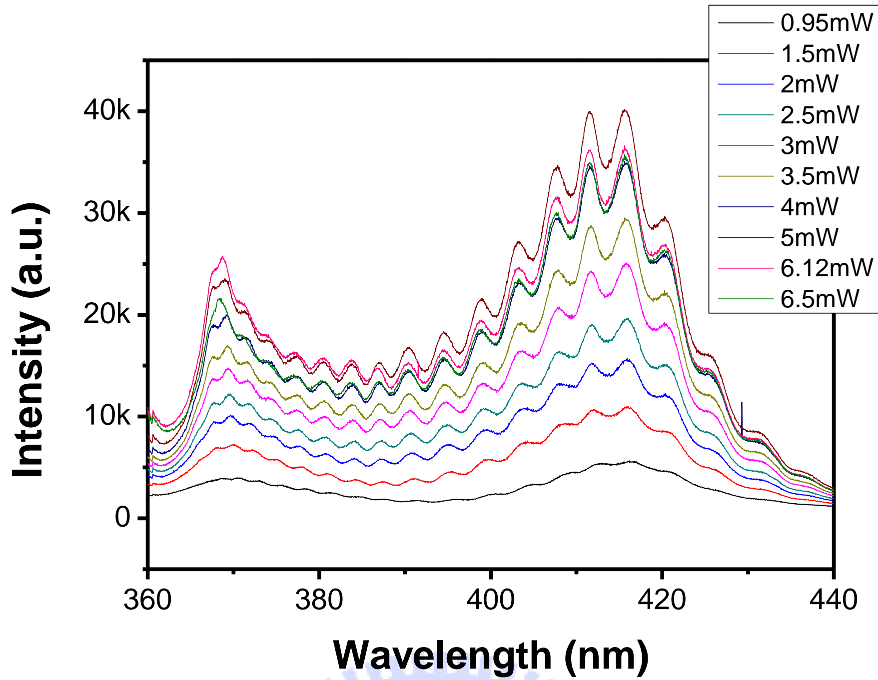

Fig. 3.12 PL spectrum before laser lift-off

The sample was then subjected to the laser lift-off process. A KrF excimer laser at a wavelength of 248 nm was used to remove the sapphire substrate. The laser with a beam size of 1.2 mm × 1.2 mm was incident from the polished backside of the sapphire substrate onto the sapphire/GaN interface to decompose GaN into Ga and N_2. The lift-off sapphire substrate is shown in Fig. 3.13. After laser lift-off process, the original sapphire substrate separated from GaN-based material which totally transferred to the copper substrate.

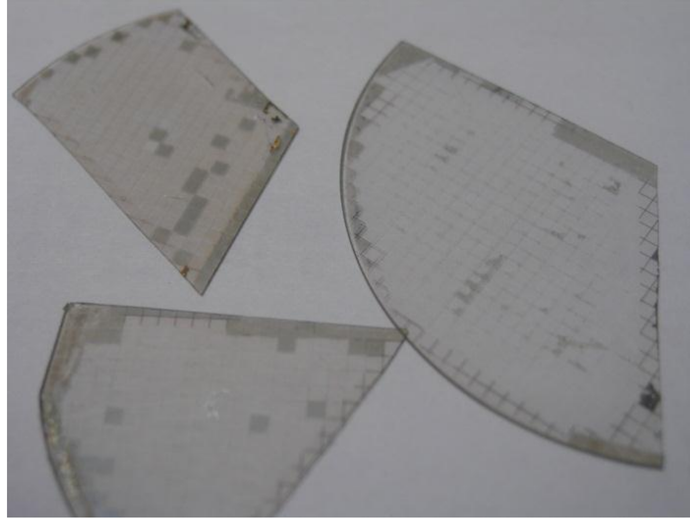

Fig. 3.13 Photography of lift-off sapphire substrate

Step10：Dry etching control vertical size (Fig. 3.6 (j))

First the sample was dipped into diluted HCl solution to remove residual Ga droplet on the u-GaN. We used the ICP dry etching system to remove the u-GaN about 3 μm and remain the n-GaN around 1.96μm. However, in this step the p-GaN surface was damaged by ICP dry etching. The roughness will make serious non-radiation, which may makes the loss higher than the gain in the laser structure.

Step11：Reduce roughness by polish (Fig. 3.6 (j))

Then we used the polish technique as we mentioned in chapter 2 to reduce the surface roughness. The surface roughness was examined by AFM, The RMS comparison shown in Fig. 3.14 proved that ICP etching truly makes the surface damaged. And the polish technique reduces the effect so much.

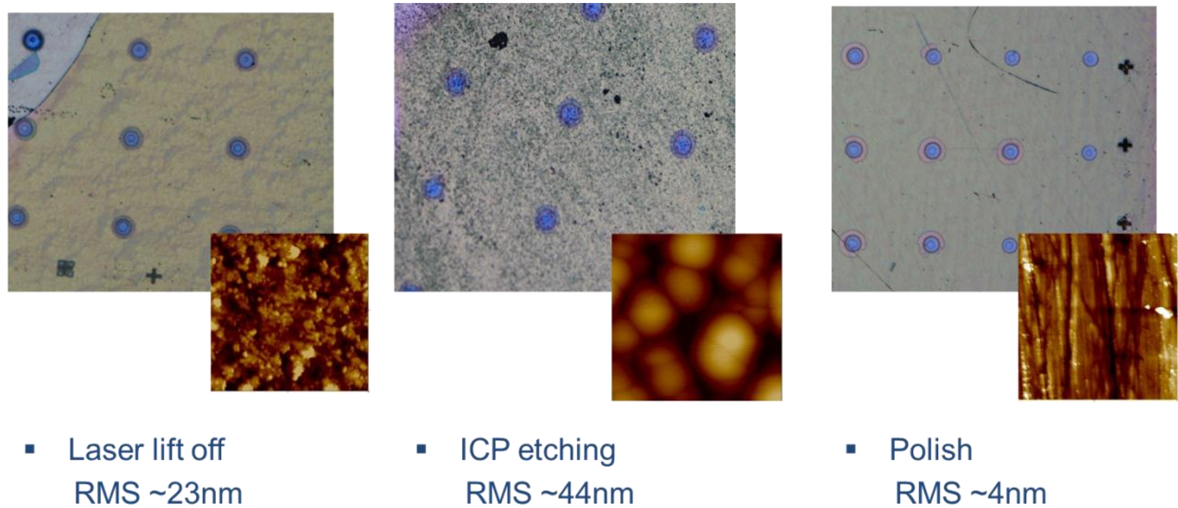

Fig. 3.14 OM image and roughness comparison from step 9 to step 11.

<u>Step12：Isolate each laser structure (Fig. 3.6 (k))</u>

Then we used the photolithography technique to define the “small” mesa, which meant individual devices. The ICP system etched all of the areas but the “small mesa”. This work isolated each laser structure and prevented any current leakage from path to surface. The Fig. 3.15 cross-sectional view and top view show many concentric circles representing each accomplished layer. The small mesa pattern is circular and 140 μm in diameter

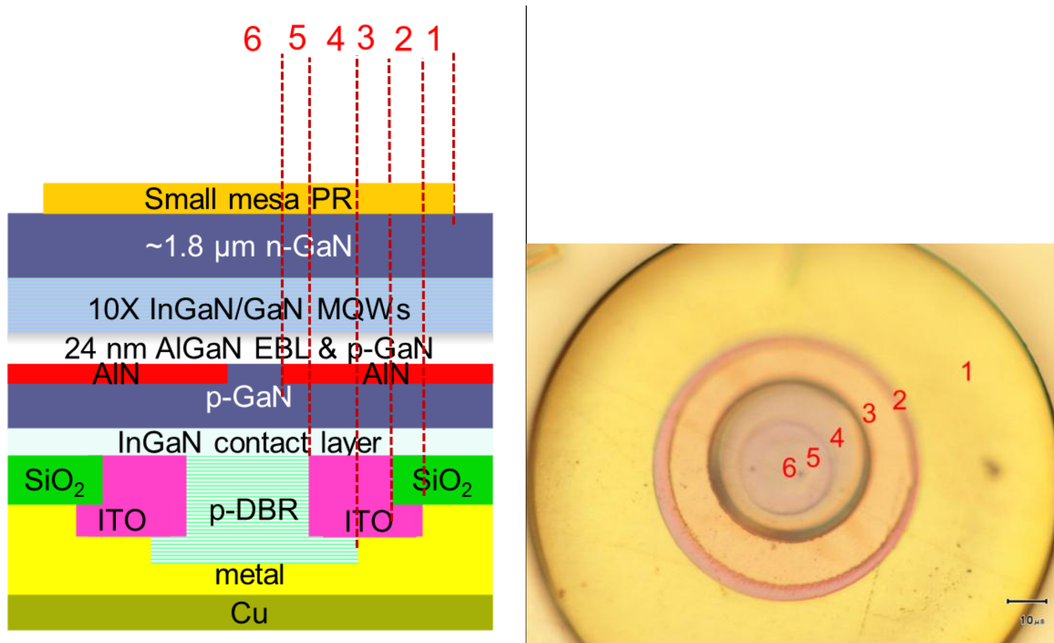

Fig. 3.15 Cross-sectional view and a top view before small mesa etching

Step13：SiO_2 passivation layer (Fig. 3.6 (l))

Deposit the 200nm SiO_2 which covered around the mesa. This work prevents the sidewall leakage. The small mesa pattern is circular and 110 µm in diameter

Step14：Cr/ Pt / Au n-contact layer (Fig. 3.6 (m))

Then the patterned chromium 50 nm, platinum 50 nm, gold 1.9 µm were formed on the n-GaN as an n-contact metal without additional semitransparent contact layer (Fig. 3.16). The n-contact layer pattern is ring shape and 125 µm in outer diameter. The inner diameter is 80 µm.

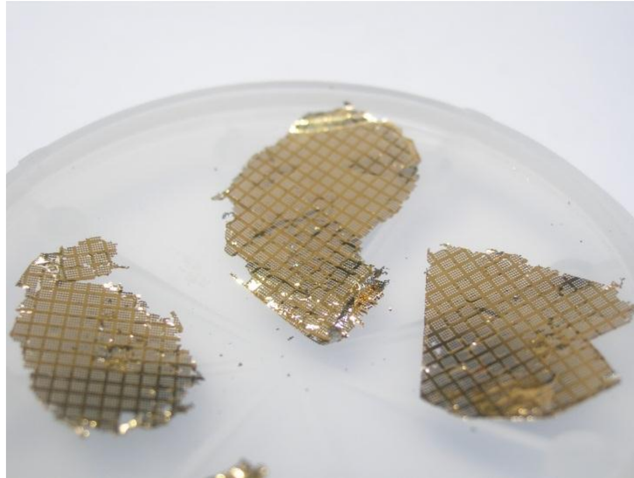

Fig. 3.16 Photography of unwanted n-contact layer lifted off by PR stripper

<u>Step15：HfO_2/SiO_2 n-side DBR (Fig. 3.6 (n))</u>

Finally, n-DBR consisting of 11 pairs of SiO_2 and HfO_2 layers was deposited on the n-type GaN surface. The measured reflectance spectrum of the SiO_2/HfO_2 DBR is exhibited in Fig. 3.17. The reflection spectrum of -DBR was exhibited in Fig. 3.17. The stop band is very wide and the reflectivity is higher than 99.2 %. The n-DBR pattern is circular and 85 μm in diameter. The final appearance of sample was shown in Fig. 3.18. N-DBR reflects blue violet color in front side and thin Au cover on Cu substrate appear golden color.

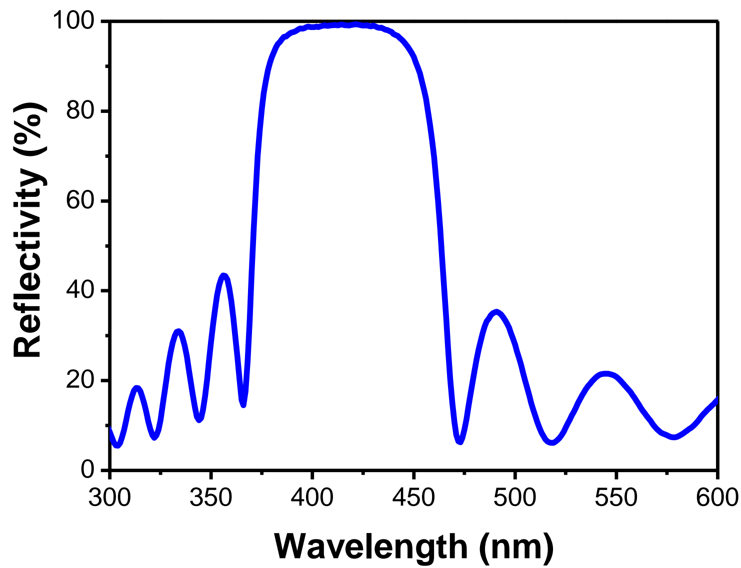

Fig. 3.17 The reflection spectrum of 11 pairs of HfO_2 /SiO_2 n-DBR

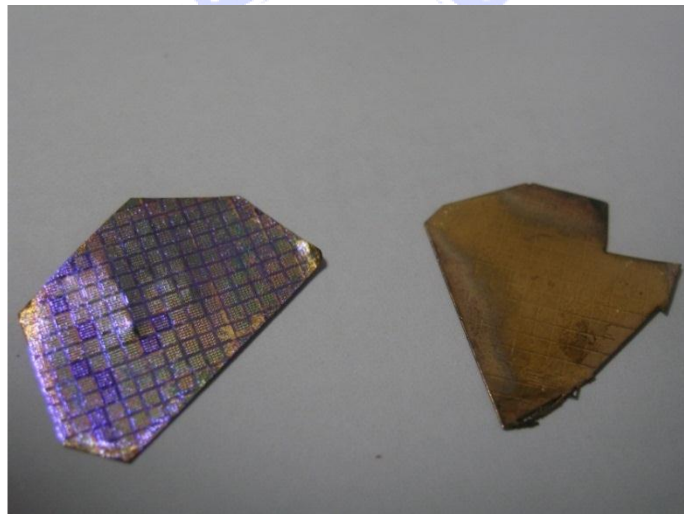

Fig. 3.18 Photography of final VSCELs in front side and back side

3.3 Characteristics of AlN layer

Aluminum nitride is stable at high temperatures in inert atmospheres and melts at 2800 ℃. In a vacuum, AlN decomposes at ~1800 ℃. In the air, surface oxidation occurs above 700℃, and even at room temperature, surface oxide layers of 5-10 nm have been detected. This oxide layer protects the material up to 1370℃. Above this

temperature bulk oxidation occurs. Aluminum nitride is stable in hydrogen and carbon dioxide atmospheres up to 980℃. The material dissolves slowly in mineral acids through grain boundary attack, and in strong alkalies through attack on the aluminum nitride grains. The material hydrolyzes slowly in water. Aluminum nitride is resistant to attack from most molten salts, including chlorides and cryolite. Aluminum nitride (AlN) is a nitride of aluminium. Its wurtzite phase (w-AlN) is a wide band gap (6.2 eV) semiconductor material, giving it potential application for deep ultraviolet optoelectronics.

Among the prominent nitride semiconductors such as, GaN, AlN, InN and their alloys, with the notable exception of AlN and its alloys, layers of high-quality most of the materials can be grown at temperatures of 1200 ℃ or less. The crystalline quality of AlN layers is always inferior to its counterpart GaN grown at much lower temperatures. The high temperature growth of AlN films is expected to be effective in improving crystalline quality and surface morphology because surface migration of Al-species would increase at high temperatures.

Although the high temperature re-growth condition contribute the better quality of AlN film, but it may probably damage the quantum well. As the result, we choose lower temperature conditions to re-growth the AlN current blocking layer.

The regrowth temperatures are various from 850°C to 1080°C. We used four probe and AFM to measure the sheet resistance and roughness of AlN. Fig.3.19 shows the AFM of three re-growth conditions, as the temperature rise the morphology of film become more flatness. Table3.1 shows the comparisons of three temperatures in different re-growth condition.

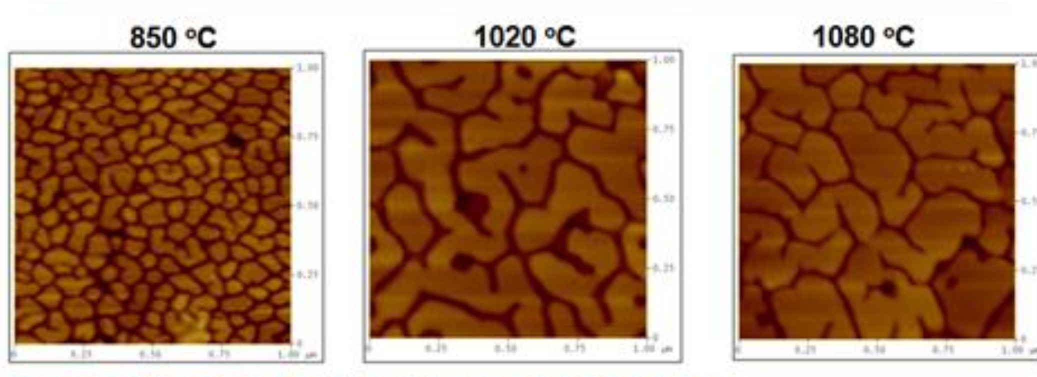

Fig. 3.19 AFM image of three different re-growth temperatures.

	850 °C	1020 °C	1080 °C
Sheet resistance	3~5KΩ	6~8KΩ	6~13KΩ
R.M.S.	3.627nm	2.935nm	2.485nm

Table 3.1 Resistance and roughness comparison of AlN film with three different re-growth temperatures.

3.4 Results and Discussion

3.4.1 The optical characteristics of VCSELs

Before the lasts step, we measured the PL spectrum. Not only the p-DBR has high reflectivity, but also we use apply the polish technique. In Fig. 3.20, we can observe clear Fabry-Perot modes before the n-DBR being deposited and obtain the FWHM around 3 nm. Besides, the longitude mode spacing around 10nm, coincide with the estimated cavity length 3 μm. The value is reasonable because in our case the structure height was reduced to around 2.3 μm (1.96μm n-GaN, 145nm QWs, 186nm p-GaN) by ICP dry etching. And the accurate cavity length has to plus penetration depths in the p-DBR and air. The structure's reflectivity simulated by transfer matrix shows the regular dips with same spacing around 10nm in Fig. 3.21 which is another

evidence of longitude modes. By the way, clear Fabry-Perot modes prove that the polish technique reduces the surface roughness resulted from step9 to step14 and makes a good mirror in n-side surface.

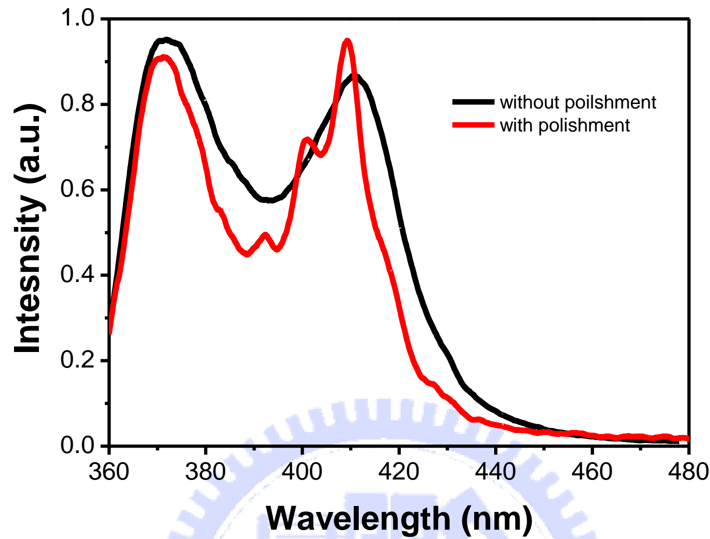

Fig. 3.20 PL spectrum without n-DBR was deposited

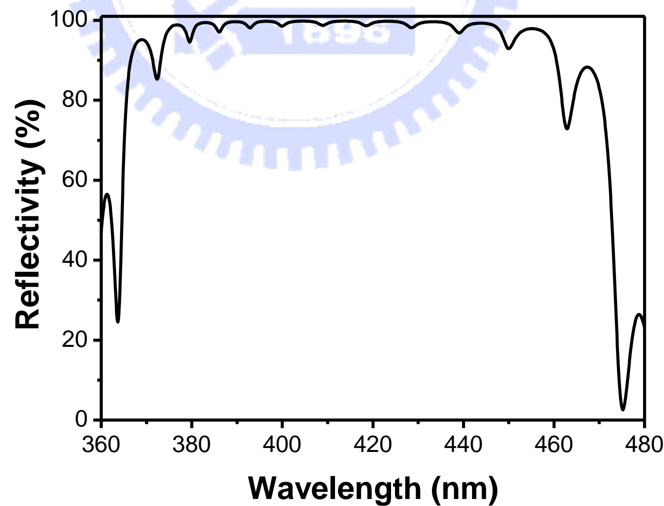

Fig. 3.21 The simulated reflectivity without n-DBR was deposited

After the n-DBR being deposited, we measured the PL spectrum. Because the two-DBR has high reflectivity, we observed the laser operation pumped by pulse laser at room temperature.

For the device with 70 nm AlN confinement layer and 8 μm apertures, we obtained the PL spectrum (Fig. 3.22) with the FWHM around 0.5 nm near threshold and correspond the Q factor around 800 when approaching threshold energy. Noticed that in here we chose the highest peak at 401.3 nm to calculate. We also check the value by transfer matrix. The simulated reflectivity of the structure with p-DBR and n-DBR shows a special narrow pit (FWHM 0.5 nm) at the wavelength of 401 nm in Fig. 3.23. The narrow pit means good cavity and the possibility of laser appearance around the wavelength.

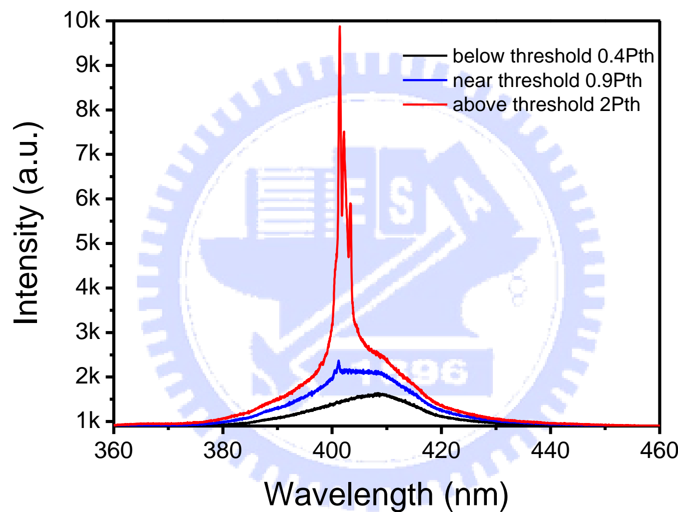

Fig. 3.22 The PL spectrum before n-DBR was deposited

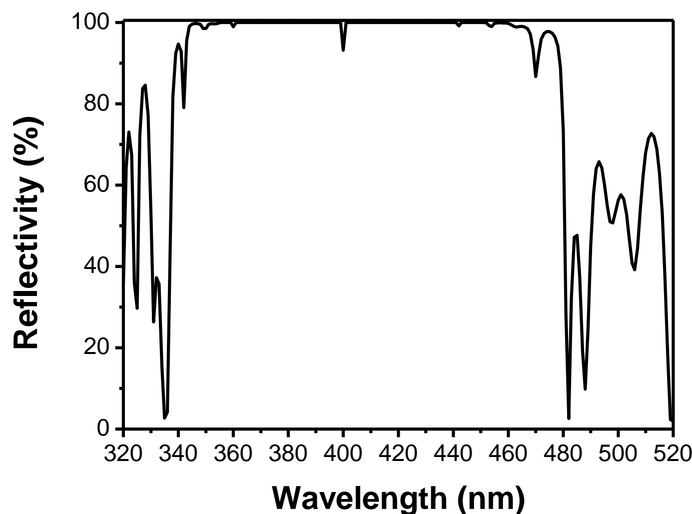

Fig. 3.23 The PL spectrum before n-DBR was deposited

The laser operation can be confirmed by two step L.L. curve (Fig. 3.24) and near 70% polarization (Fig. 3.25). The relatively high threshold energy density around 750 mJ/cm^2 does not means abnormal behavior in the structure. Actually, there is only few pumping power passing through the p-DBR and the 1.96 μm n-GaN material. The p-DBR reflectivity is 43% for the wavelength of the pumping power. The rest of pumping power passing through 1.96 μm n-GaN material also can be estimated. The absorption coefficient α using the approximation equations

$$\alpha = \alpha_0 * \sqrt{\frac{(E-Eg)}{Eg}},\ \alpha_0 = 2 * 10^5\ cm^{-1} \quad (3.23)$$

, where E is the corresponding energy gap of the pumping power, Eg the energy gap of the absorption material. In our case α around 2.747*10^4 cm^{-1} implying that less than 0.5% pumping power will remain. Traditional VCSELs has only around 200nm p-GaN material on the top of quantum wells (QWs) implying 57% pumping power remains.

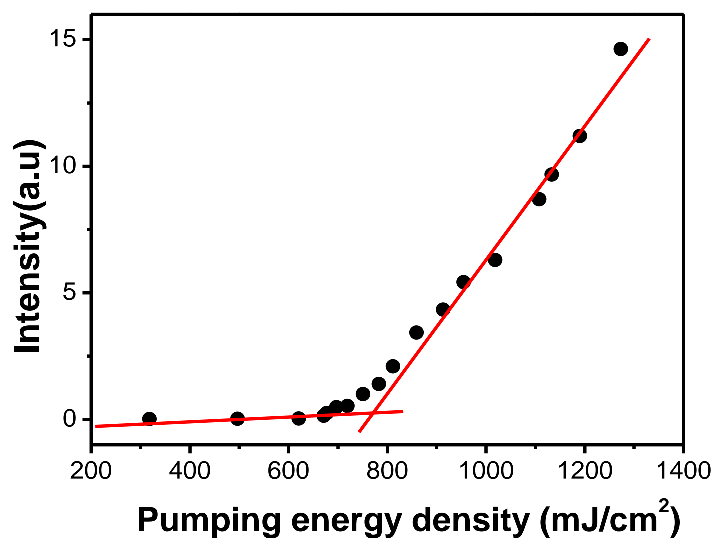

Fig. 3.24 The light output power verse the pumping energy density

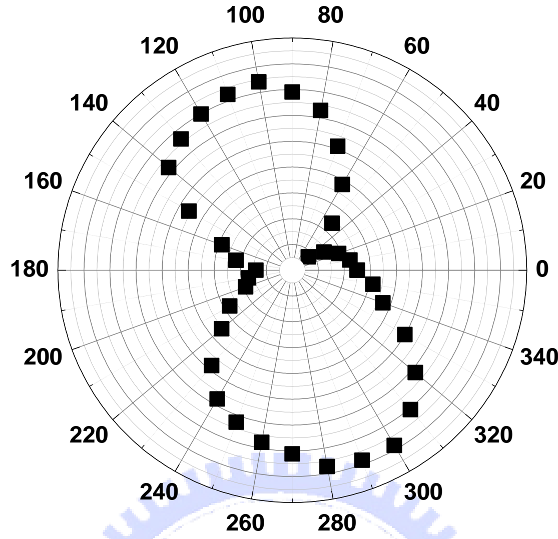

Fig. 3.25 The polarization characteristics of the laser emission from the VCSEL above the threshold.

We estimated the spontaneous emission coupling factor of our VCSEL sample from Fig. 3.26, which is the logarithm plot of Fig. 3.24. According to Horowicz et al., the difference between the heights of the emission intensities before and after the threshold corresponds roughly to the value of β. We obtained a β value of about $2.5*10^{-2}$ for our VCSEL. We also estimated the β value from the Purcell factor F_p using the approximation equations

$$F_p \cong \frac{3Q(\frac{\lambda}{n})^3}{4\pi^2 V} \tag{3.23}$$

, where Q is the cavity quality factor, λis the laser wavelength, V is the optical volume of laser emission, and n is the refractive index. The refractive index is 2.54 for the GaN cavity. The optical volume V is estimated to be about $9.273*10^{-12}cm^3$ for a measured emission spot size of about 2.1 μm. And the accurate cavity length is about 17 λ considering the penetration depth of the DBRs (Fig. 3.27). The cavity length

was confirmed by calculating the numbers of wave packets in transfer matrix simulation as shown in Fig. 3.27. Of course you can confirm the cavity length by using the formula about penetration depth which we had mentioned in chapter 3.1. Anyway, by using these parameters, we obtained an estimated Purcell factor of about $2.56*10^{-2}$ and an estimated β value of about $2.49*10^{-2}$ which is close to the value we obtained above from Fig. 3.26. This β value is nearly three orders of magnitude higher than that of the typical edge emitting laser which is generally in the order of 10^{-4} ~10^{-5}.

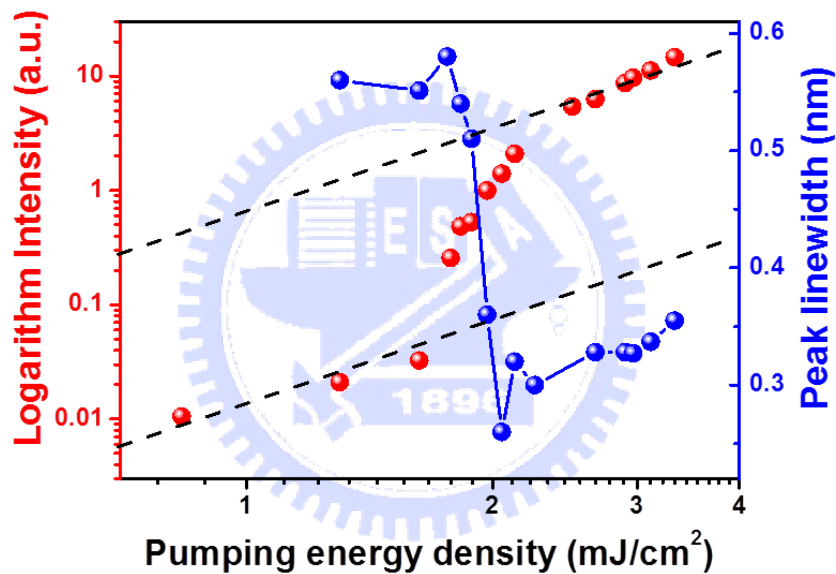

Fig. 3.26 The logarithm light output power and laser emission peak linewidth verse the effective pumping energy density penetrating to QWs

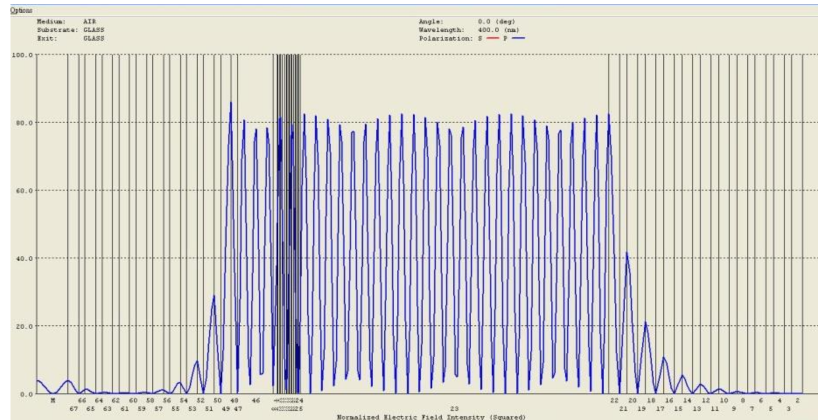

Fig. 3.27 The electric field intensity simulated by transfer matrix, the horizontal axis correspond the layer arrangement of the VCSELs.

As you can see in Fig. 3.28, multiple peaks appear on the plot of the power over threshold. The phenomenon is obviously different from standard VCSELs with single mode. In Fig. 3.20 the longitude mode spacing in the VCSELs is around 10 nm which is much larger the multi-peaks spacing in Fig. 3.22. We supposed those peaks being generated by the refractive index difference between AlN and GaN. The refractive index difference provides the optical confinement in transverse direction. Standard VCSELs does not consider the transverse mode effect, mainly because the horizontal scale (several hundred micrometers) is much larger than the vertical distance (few micrometers). And the transverse modes leak out rapidly since the sidewall roughness and big surface area. Even the transvers modes fortunately exit in the structure, the spacing in spectrum will less than few angstroms and there is no regularity in the horizontal scale (several hundred micrometers). The AlN apertures from 5 μm to 20 μm are near the cavity vertical distance, so it cannot be neglect. Additionally, because

the apertures are in the middle of the VCSELs, the configuration gives the possibility of holding stable transverse modes. And the identifiable mode spacing might be observed in this horizontal scale. For an almost planar resonator, such as the VCSELs with top and bottom DBRs, the mode spacing can be given by

$$\Delta\nu = \frac{c\lambda_0}{2\pi^2 n^2 w_0^2} \quad and \quad \Delta\lambda = \frac{\Delta\nu * {\lambda_0}^2}{c} \tag{3.24}$$

Where n is the effective refractive where n is the effective refractive index

and w_0 is the minimum spot size. The measured spot size is 2.1 μm and the estimated mode spacing is 0.115 nm for n=2.54 and $\lambda_0 = 401$ nm. The measured mode spacing is approximately same order as shown in Fig. 3.28, which is the same order with the estimated value.

(a)

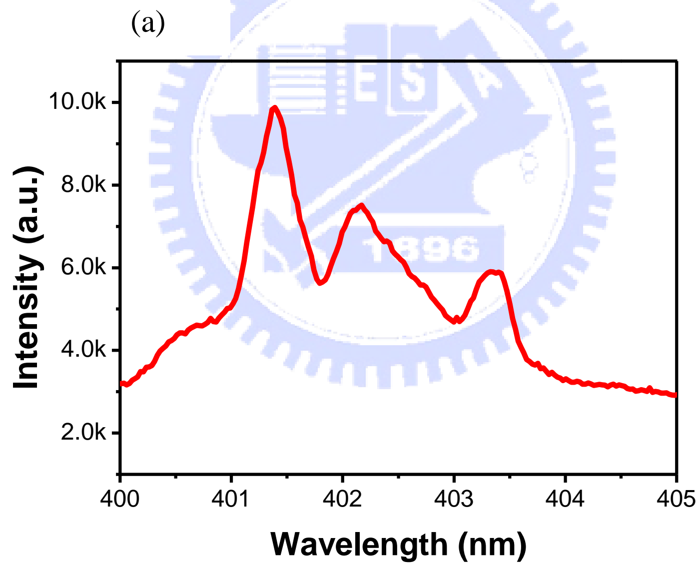

(b)

(c)

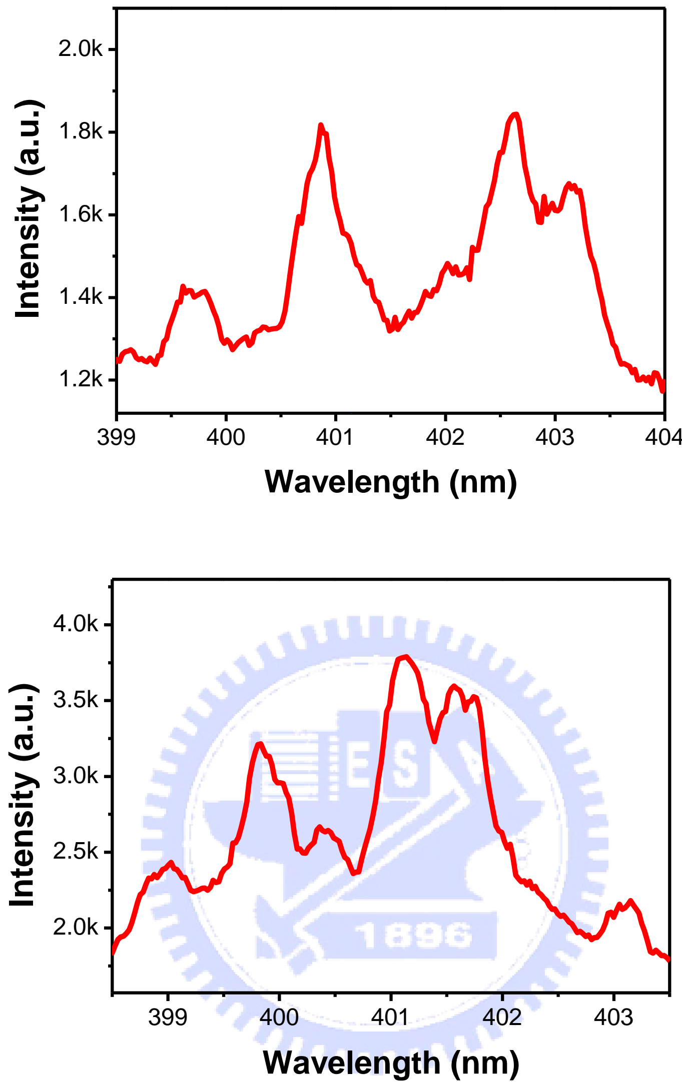

Fig. 3.28 Transverse modes of the VCSELs of (a) 8 μm (b) 15 μm (c) 20 μm in AlN aperture size.

3.5 Summary

In summary, we have investigated the VCSELs with buried AlN current apertures. In the optical characteristics, The emission from the VCSEL with aburied AlN layer shows a very narrow linewidth of 0.3 nm, corresponding to a cavity Q-value of 800, and a dominant emission peak wavelength at 401 nm. The measured average cavity mode spacing is approximately 0.5 nm, which is roughly consistent with the estimated value, demonstrating the effect of lateral optical confinement

provided by the AlN layer. Further optimization of bottom DBR growth and crystal quality in this structure would promise to realize low threshold GaN-based VCSELs or GaN-based polariton lasers.

Reference

[1] Ning, C. Z. oSemiconductor nanolasers. physica status solidi (b), NA-NA, doi:10.1002/pssb.200945436 (2010).

[2] A. Sharma, J. M. Yarrison-Rice, H. E. Jackson, and K. D. Choquette, J. Appl. Phys. 92, 6837 (2002).

Chapter 4

Silver Coated Metal-Cavity Nanolasers with Distributed Bragg Reflectors

4.1 Operation Principle of Metal-Cavity Nanolasers

4.1.1 Surface Plasmons Theory

Surface plasmon (SP) [1] are light waves trapped on the surface because of electron gas couple with photons. It is a kind of electromagnetic wave propagating on the interface. The SPPs existed ate their interface between dielectric materials and metal could attribute to resonant coupling of photons from the polarized light with the oscillation of metal free electron.

In Drude model, the complex dielectric constant derived from the free electron in metal driven by electromagnetic can be given by

$$\varepsilon(\omega) = 1 - \frac{\omega_p^2}{\omega^2 + i\omega r_D} \tag{4.1}$$

Where $\omega_p = (\frac{Ne^2}{m\varepsilon 0})^{\frac{1}{2}}$ means plasma frequency, r_D is collision frequency, N is free electron number around 10^{25}~10^{26}. For magnetic frequency smaller than ω_p, Re[ε]<0 and $\mathrm{Im}[\varepsilon] \ll |\mathrm{Re}[\varepsilon]|$, In general, ω_p is deep UV region and r_D much smaller than ω in visible light.

Because $\tilde{n} = \sqrt{\varepsilon} = n + ik$, we find out k will much bigger than n when $r_D < \omega < \omega_p$. This means the electromagnetic waves decay rapidly. And k around zero when $\omega_p < \omega$. This means electromagnetic waves can propagate inside the metal.

Surface plasmon only exit in TM modes. For TE waves there is only parallel component and cannot accumulate surface charge. On the other sides, TM waves

provide vertical component which induce polarization charge density. The charge can be driven by parallel force and form longitudinal waves as shown in Fig. 4.1(a).

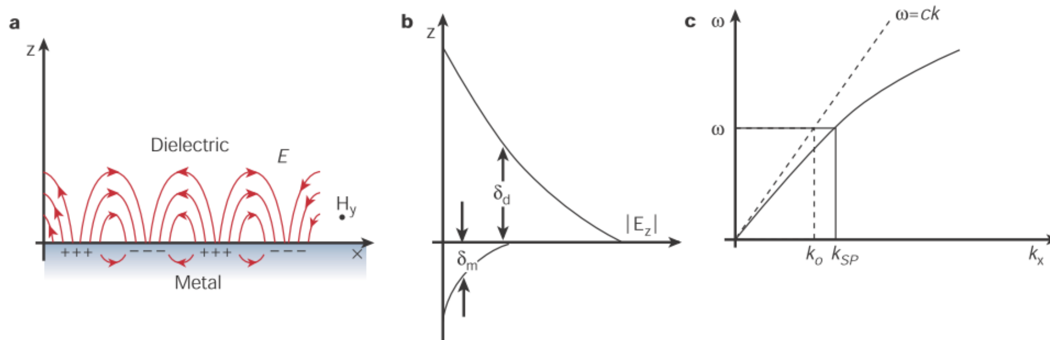

Fig. 4.1 (a)The schematic representation of electron density wave propagating along a metal-dielectric interface (b) the electric field distribution around the interface (c) dispersion curve of surface plasmon

SPs at the interface between a metal and a dielectric material have a combined electromagnetic wave and surface charge character as shown in Fig. 4.1(a). They are transverse magnetic in character (H is in the y direction), and the generation of surface charge requires an electric field normal to the surface. This combined character also leads to the field component perpendicular to the surface being enhanced near the surface and decaying exponentially with distance away from it Fig. 4.1(b). The field in this perpendicular direction is said to be evanescent, reflecting the bound, non-radiative nature of SPs, and prevents power from propagating away from the surface. In the dielectric medium above the metal, typically air or glass, the decay length of the field, δ_d, is of the order of half the wavelength of light involved, whereas the decay length into the metal, δ_m , is determined by the skin depth. The dispersion curve for a SP mode in Fig.4.1(c) shows the momentum mismatch problem that must be overcome in order to couple light and SP modes together, with the SP mode always lying beyond the light line, that is, it has greater momentum ($\hbar k_{sp}$) than

a free space photon ($\hbar k_0$) of the same frequency ω.

By Maxwell equation and boundary condition, only TM wave could generate surface plasmon modes which also have to obey Eq. 4.2 and Eq. 4.3.

$$\frac{k_{1z}}{\varepsilon_1} + \frac{k_{2z}}{\varepsilon_2} = 0 \tag{4.2}$$

$$k_x = \frac{\omega}{c}\left[\frac{\varepsilon_1 \varepsilon_2}{\varepsilon_1 + \varepsilon_2}\right]^{\frac{1}{2}} \tag{4.3}$$

Finally, we could infer that necessary material characteristic condition for two material generating surface plasmon are Eq. 4.4 and Eq. 4.5

$$Re[\varepsilon_1] + Re[\varepsilon_2] < 0 \tag{4.4}$$

$$Re[\varepsilon_1]*Re[\varepsilon_2] < 0 \tag{4.5}$$

SPs could concentrate and channel light under subwavelength scales, which has a huge potential on exploring physical phenomenon under such small scale, and this might help scientists and engineers to make photonic integrated circuit with small size. This kind of structure also solves the problem that dielectric waveguide would show poor confinement under subwavelength region. Concentrating light in this way leads to an electric field enhancement that can be used to manipulate light–matter interactions and boost non-linear phenomena. Therefore, lots of applications have been developed for many years and exit in our daily life [2-5]

It is the most difficult task for researchers to observe the behavior of a bio molecule. Therefore, in order to observe this tiny molecule with the size in just a few nanometers, researchers utilize surface plasmon effect to improve the extraction of light. With this new technique, researchers could observe their samples and distinguish its details even in subwavelength region. For biosensor, the utilization of surface plasmon effect makes the test sample become label free and can be detected

directly in real time. This has been applied to drug screening, kinase analysis and research on antibody development. To further lower the cost of production for a single chip, a better lithography is needed to put more patterns on a single wafer , the e-beam lithography and other techniques are still struggling on their throughput, which is too low to become commercialize. A set of plasmonic mirrors takes the advantages of surface plasmon effect and demonstrate lithography techniques with a linewidth only 80nm recently [3]. This new method has showed a promising way to the development of nanolithography. Moreover , taking the advantages of energy confinement and field enhancement, researchers have achieved making a semiconductor laser in subwavelength scale even with the lossy metal coated on it [5]. This will discuss thoroughly in the following section.

4.1.2 Circular Waveguide Theory

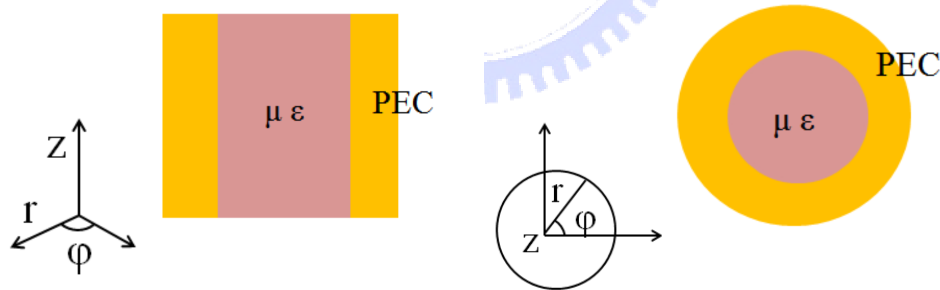

Fig. 4.2 A circular waveguide

For a circular waveguide [6] (Fig. 4.2), we can perform the sequence of steps in cylindrical coordinates as we did in rectangular coordinates to find the transverse field components in terms of the longitudinal (i.e. Ez , Hz) components. In cylindrical coordinates, the transverse field is

$$E_T = \hat{r}Er + \hat{\varphi}E\varphi \tag{4.6}$$

$$H_T = \hat{r}Hr + \hat{\varphi}H\varphi \tag{4.7}$$

Using this in Maxwell's equations (where the curl is applied in cylindrical coordinates) leads to

$$H_r = \frac{j}{k_c^2}\left(\frac{\omega\varepsilon}{r}\frac{\partial E_z}{\partial\varphi} - \beta\frac{\partial H_z}{\partial r}\right) \tag{4.8}$$

$$E_r = \frac{-j}{k_c^2}\left(\beta\frac{\partial E_z}{\partial\varphi} - \frac{\omega\mu}{r}\frac{\partial H_z}{\partial r}\right) \tag{4.9}$$

$$H_\varphi = \frac{-j}{k_c^2}\left(\omega\varepsilon\frac{\partial E_z}{\partial r} - \frac{\beta}{r}\frac{\partial H_z}{\partial\varphi}\right) \tag{4.10}$$

$$E_\varphi = \frac{-j}{k_c^2}\left(\frac{\beta}{r}\frac{\partial E_z}{\partial\varphi} - \omega\mu\frac{\partial H_z}{\partial\varphi}\right) \tag{4.11}$$

where

$$k_C = k - \beta \tag{4.12}$$

TEM waves cannot exit in such a waveguide without inner conductor. Because in this configuration conductor current $I_c = 0$, and TEM waves $E_z = H_z = 0$ makes the no displacement current $I_d = 0$.

TE modes in circular waveguides

Using the homogenous Helmholtz's equation derives from time-harmonic Maxwell's equation.

$$(\nabla^2 + k^2)\begin{pmatrix}\vec{H}\\ \vec{E}\end{pmatrix} = 0 \tag{4.13}$$

For TM modes $E_z = 0$, we only consider $(\nabla^2 + k^2)H_z = 0$, in cylindrical coordinates of above gives

$$\left(\frac{\partial^2}{\partial r^2} + \frac{1}{r}\frac{\partial}{\partial r} + \frac{1}{r^2}\frac{\partial^2}{\partial\varphi^2} + \frac{\partial^2}{\partial z^2} + +k^2\right)H_z(r,\varphi,z) = 0 \tag{4.14}$$

Using the separation of variables approach, we let $H_z(r,\varphi,z) = R(r)\Phi(\varphi)e^{-j\beta z}$

Using this result in Eq. 4.13 leads to

$$r^2R'' + rR' + (r^2{k_C}^2 - n^2)R = 0 \tag{4.15}$$

The general solutions are

$$\Phi(\varphi) = c_1 \sin n\varphi + c_2 \cos n\varphi \, , n = 1, 2, 3 \ldots \tag{4.16}$$

$$R(r) = c_1 J_n(k_C r) + c_2 Y_n(k_C r) \tag{4.17}$$

Where $J_n(x)$ is the Bessel function of the first kind of order n and $Y_n(x)$ is the Bessel function of the second kind of order n as shown in Fig. 4.3.

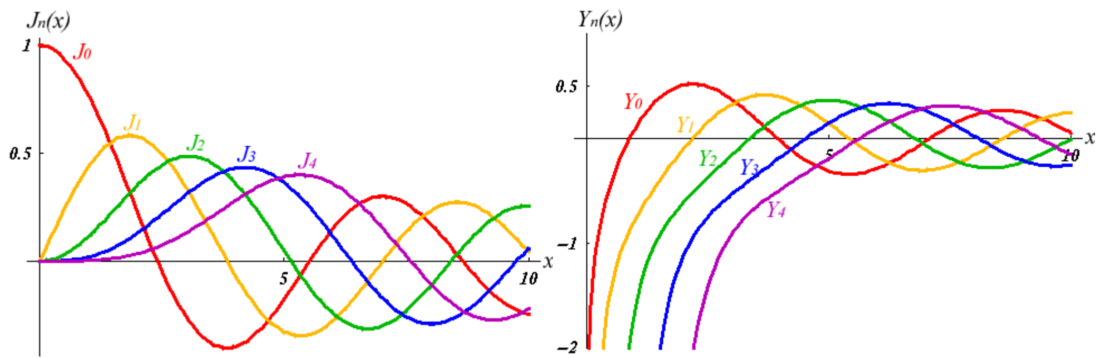

Fig. 4.3 Bessel function of the first kind and second kind

Obviously, $Y_n(r \to 0) \to -\infty$, Eq. 4.16 degenerate to $R(r) = c_1 J_n(k_C r)$

From above all, the results is

$$H_z(r, \varphi, z) = (c_1 \sin n\varphi + c_2 \cos n\varphi) * J_n(k_C r) * e^{-j\beta z} \tag{4.18}$$

To find out the k_C and n, we substitute Eq. 4.18 into Eq. 4.11, we get

$$E_\varphi(r, \varphi, z) = \frac{j\omega\mu}{k_C}(c_1 \sin n\varphi + c_2 \cos n\varphi) * J_n{}'(k_C r) * e^{-j\beta z} \tag{4.19}$$

The function to satisfy boundary condition $E_\varphi(r = a) = 0$ can be written as

$$J_n{}'(k_C a) = 0 \tag{4.20}$$

The zero point gives in Table 10.1. Table Xxx lists the values of several x_{nm}, which denotes the m_{th} zero of $J_n{}'(x)$: $J_n{}'(x'_{nm}) = 0$

n \ m	1	2	3
0	3.832	7.016	10.174
1	1.841	5.331	8.536

2	3.054	6.706	9.970

Table 10.1 Zeros of $J_n'(x'_{nm}), x'_{nm}$

TM modes in circular waveguides

Similarly, for TM modes H_z =0, we only consider $(\nabla^2 + k^2)E_z = 0$, in cylindrical coordinates of above gives

$$(\frac{\partial^2}{\partial r^2} + \frac{1}{r}\frac{\partial}{\partial r} + \frac{1}{r^2}\frac{\partial^2}{\partial \varphi^2} + \frac{\partial^2}{\partial z^2} + +k^2)E_z(r, \varphi, z) = 0 \quad (4.21)$$

Using the separation of variables approach, we let $E_z(r, \varphi, z) = R(r)\Phi(\varphi)e^{-j\beta z}$

Similar way from eq. 4.15to eq. 4.17then we can get

$$E_z(r, \varphi, z) = (c_1 \sin n\varphi + c_2 \cos n\varphi) * J_n(k_C r) * e^{-j\beta z} \quad (4.22)$$

The function to satisfy boundary condition $E_z(r = a) = 0$ can be written as

$$J_n(k_C a) = 0 \quad (4.23)$$

The zero point gives in Table 10.2. Table Xxx lists the values of several x_{nm}, which denotes the m_{th} zero of $J_n(x)$: $J_n(x_{nm}) = 0$

n \ m	1	2	3
0	2.405	5.520	8.654
1	3.832	7.016	10.174
2	5.135	8.417	11.620

Table 10.2 Zeros of $J_n(x_{nm}), x_{nm}$

Cutoff frequency and mode patterns

Obviously, in TE modes x'_{nm} has minimal value when n=1, m=1, in TM modes x_{nm} has minimal value when n=0, m=1, those represent the lowest k_C value in TE modes and TM modes, respectively. Besides, we can derive the lowest f_C by the

transfer equation below：

$$k = \omega\sqrt{\mu\varepsilon} = 2\pi f\sqrt{\mu\varepsilon} \tag{4.23}$$

Propagation constant β has to be real numbers for electromagnetic fields propagation, which means $k > k_C$ or $f > f_C$ is the necessary condition for waveguide mode operation. We also call f_C cutoff frequency. Frequency sequence and modes patterns$|E|$ for the lowest five modes in circular waveguides are as show in Fig. 4.4.

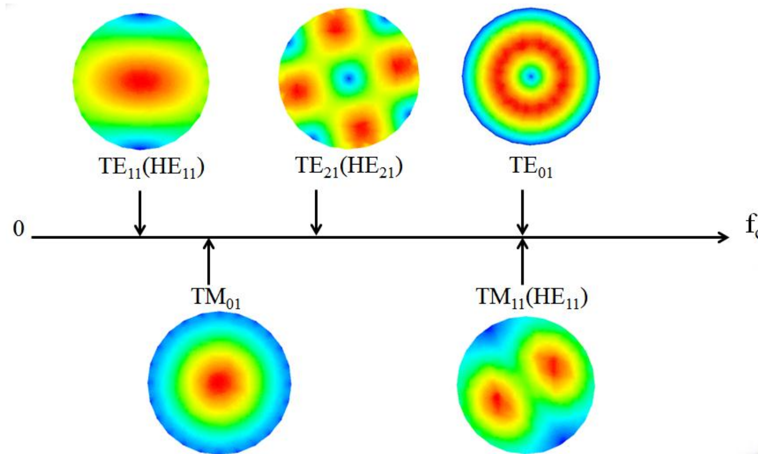

Fig. 4.4 The lowest five modes and corresponding electric fields pattern $|E|$ in circular waveguides

The z-component magnetic fields H_z for TE modes (TE_{nm}) (Fig. 4.5) are quite different from electric fields$|E|$. You may notice that n-component and m-component have relationship with z-component magnetic fields H_z in φ direction order and r direction order respectively.

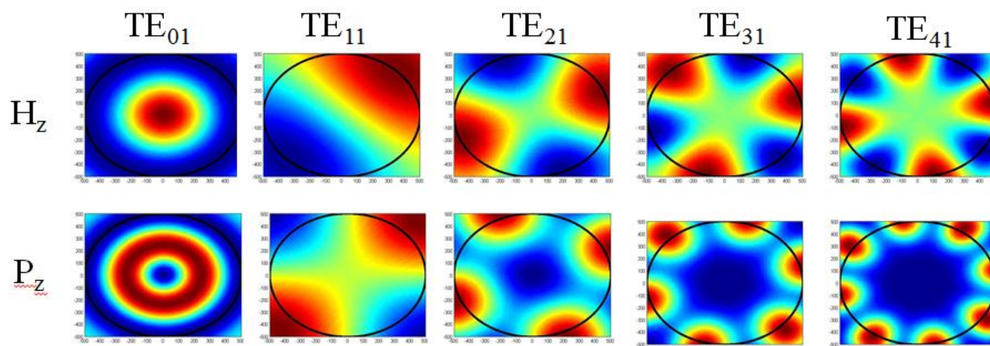

Fig. 4.5 The z-component magnetic field H_z and z-component poynting

vector P_z for several TE modes TE_{nm}

4.2 Design and Simulation of Metal-Cavity Nanolasers

Remember that we mentioned in chapter 1.4, We try to clarify some myth and develop some design rules for metal-coated nanocavity. Although there are several groups in the world declare that they create nanolasers, some problems still confuse researchers. For example, what are real physic phenomena inside nanolasers? Is the successful laser operation really attributed to plasmon effect? or there are some other cavity modes could also contributed to nanolasers? AndHow to optimize and design existing structures to achieve nanolasers?

There several kinds of laser structure have been reported to approach nanoscale laser in three dimensions. Most of them used metal to enhance the confinement factor or try to produce the surface plasmon . Here we choose the structure with one side covering by DBRs and others side covering by metal as shown in Fig. 4.6

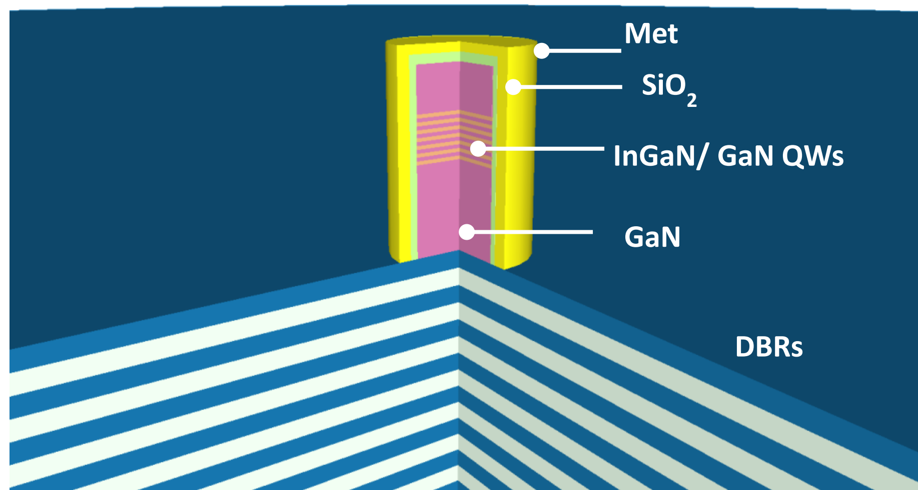

Fig. 4.6 Schematic of an nanolaser combining DBRs and metal

We convince that the structure has several advantages in the same time, including good confinement factor by covering metal, lower absorption ratio by

covering dielectric layer, good light extraction and pumping source penetration on DBRs side and an open opportunity to observe surface plasmon effect.

At the beginning, we hope to design a laser which is due to surface plasmon effect contribution. The use of finite element method and 3D model faithful shows the mode patterns inside laser. However, after numerous attempts, we find out surface plasmon effect has no benefit but concentrating the light on the surface between the dielectric layer and the metal layer. Such phenomena both lower the confinement factor and quality factor. In other words, the surface plasmon effect makes the unattainable threshold energy, although the effect has smallest mode volume. Here is an example, for the case with the configuration of 5 layers DBRs、GaN 200 nm in diameter and 1000 nm in height、50 nm silver and SiO_2 coating. The quality factor distribution by simulation (Fig. 4.7) indicates that waveguide modes may have more chance to produce a feasible laser structure.

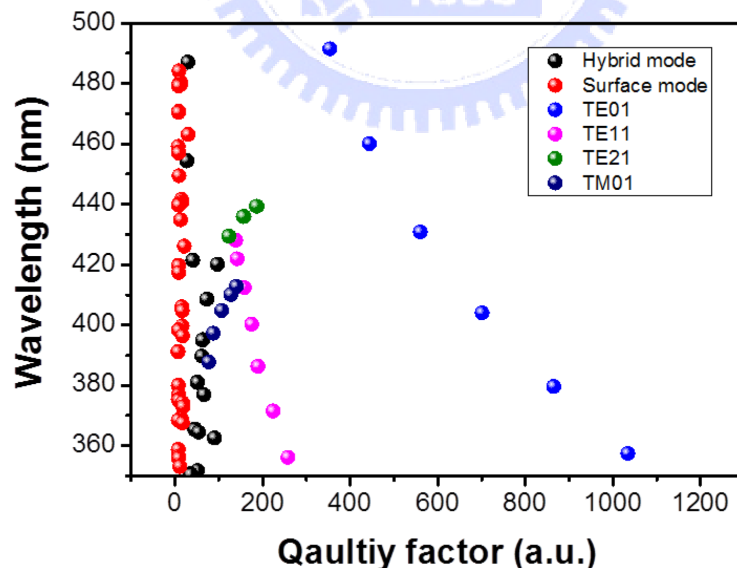

Fig. 4.7 The Quality factor distribution of different modes for an laser

Fig. 4.8 shows the mode pattern by simulation could explain the distribution in Fig. 4.7. It seems that we will get lower quality factor when more proportion of

electric field near the metal surface. Besides, the surface plasmon effect has a characteristic of extremely high intensity near the dielectric layer and metal layer. Above two reasons make enormous absorption that why we get such low quality factor in surface mode.

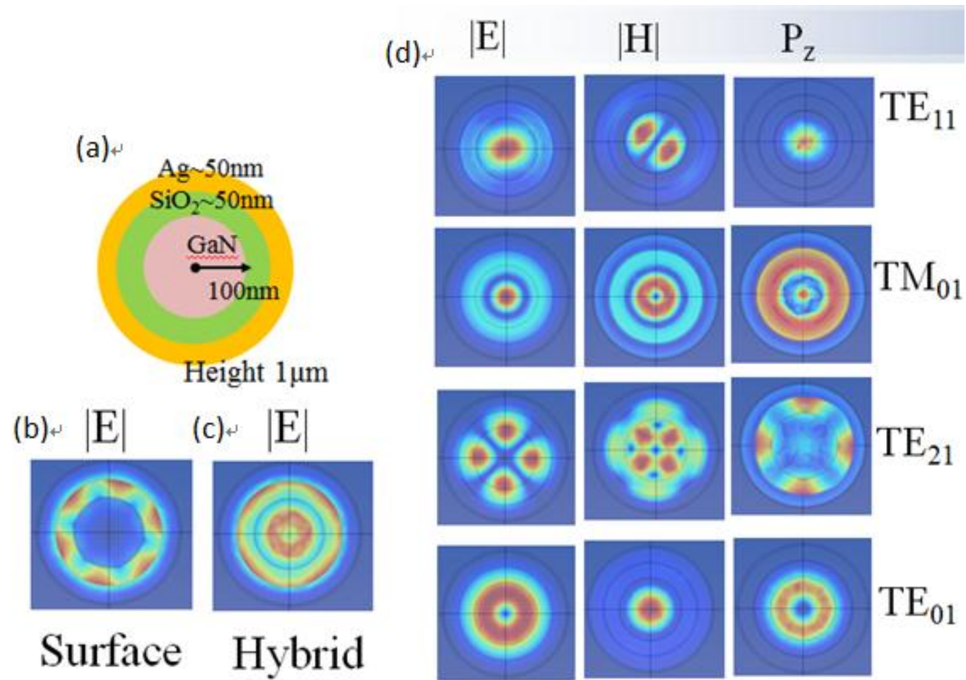

Fig. 4.8 (a) Top view illustration of the structure (b) surface mode (c) hybrid mode (d) lowest four waveguide modes

Then we change the target on waveguide modes. Before we focus on optimizing waveguide modes laser, there are three significant parameters in the structure. First, metal choices and thickness optimization. Second, dielectric layers choices and thickness optimization. Third, GaN shape, diameter and height. Each of them strongly influences the result of laser design.

Metal choices and thickness

Silver, Albumin, gold, copper are common material for reflector. As shown in Fig. 4.9 the reflectivity and absorptivity of them. Silver and Albumin shows high

reflectivity and low absorptivity in blue light region. The confinement and quality factor may be benefit from those characteristic.

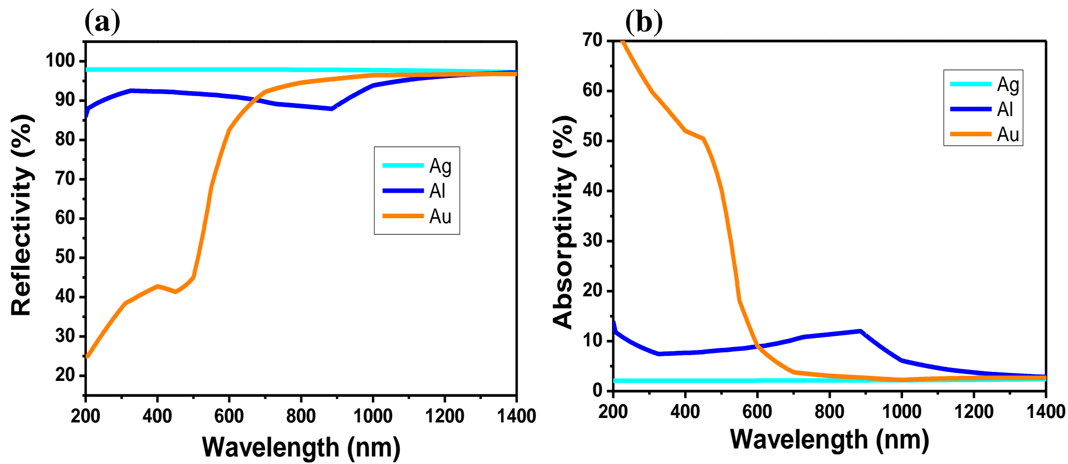

Fig. 4.9 (a) Reflectivity and (b) absorptivity of common metal reflector

Fig. 4.10 (a) shows real part a of material, the equation given below are the basic conditions for surface plasmon effect, without inserting other dielectric layer, the regions of plasmon effect observation for Ag are over 460 nm. Fig. 4.10 (b) shows the n, k of metal, Al has higher k than Au and Ag.

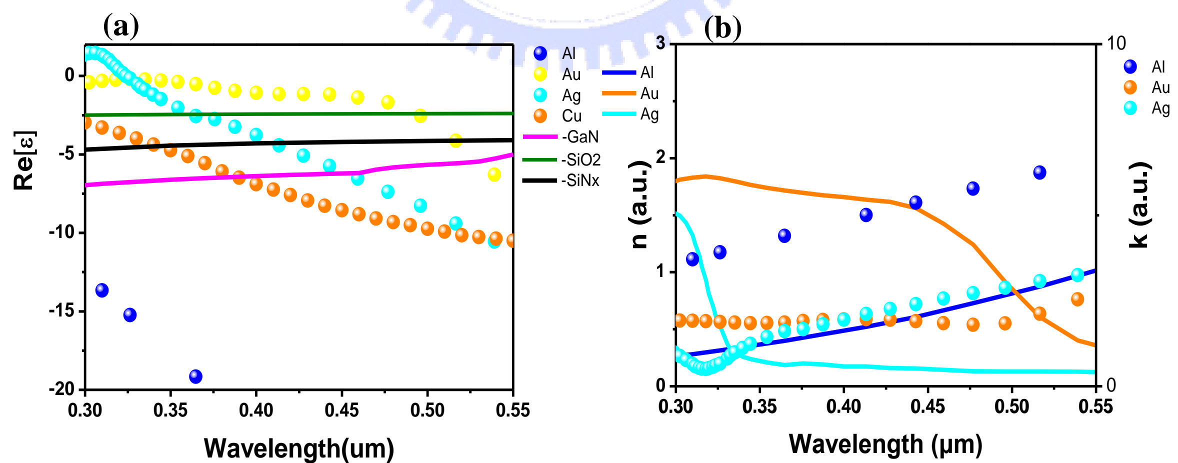

Fig. 4.10 (a) Real part of complex dielectric constant (b) n and k of common reflector

Fig. 4.11 (a) shows quality factor of the structure configuration including 5 pairs

dielectric DBRs、GaN 200 nm in diameter and 1000 nm in height、50 nm SiO_2 coating. As our perdition, Ag and Al shows higher quality factor because of high reflectivity compare with Au. Notice that there is a cross point of Al and Ag near 400nm which may due to strong absorption in UV region from plasmon frequency of Ag film. So we use Ag for GaN/InGaN QWs structure and Al for GaN bulk structure. As we could see in Fig. 4.11(b), Q factor continue growing up when applying thicker Ag and the growing rate saturate when Ag thickness over 60nm.

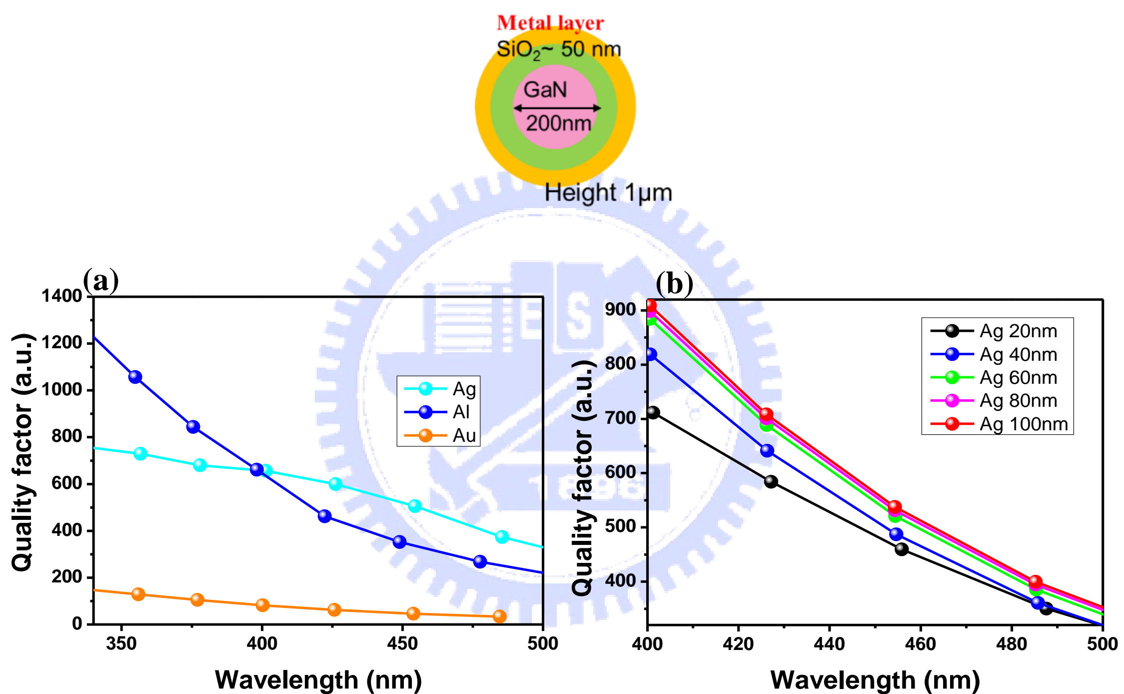

Fig. 4.11 Quality factor of (a) different metal (b) different thickness of Ag

Dielectric layer choices and thickness

As shown in Fig. 4.12 (a) to Fig. 4.12 (d), the modes pattern shows strong different with and without inserting dielectric layer . The use of dielectric layer pushes back the electric field near the metal surface. The refractive index difference between dielectric layer and GaN plays an important role. The thickness of dielectric layer also

has limitation. Excess thickness of dielectric layer gives space to bring out higher modes. Fig. 4.12 (e) shows quality factor variation of the structure configuration including 5 pairs dielectric DBRs、GaN 200 nm in diameter and 1000 nm in height、60nm Ag coating and different thickness of SiO_2.

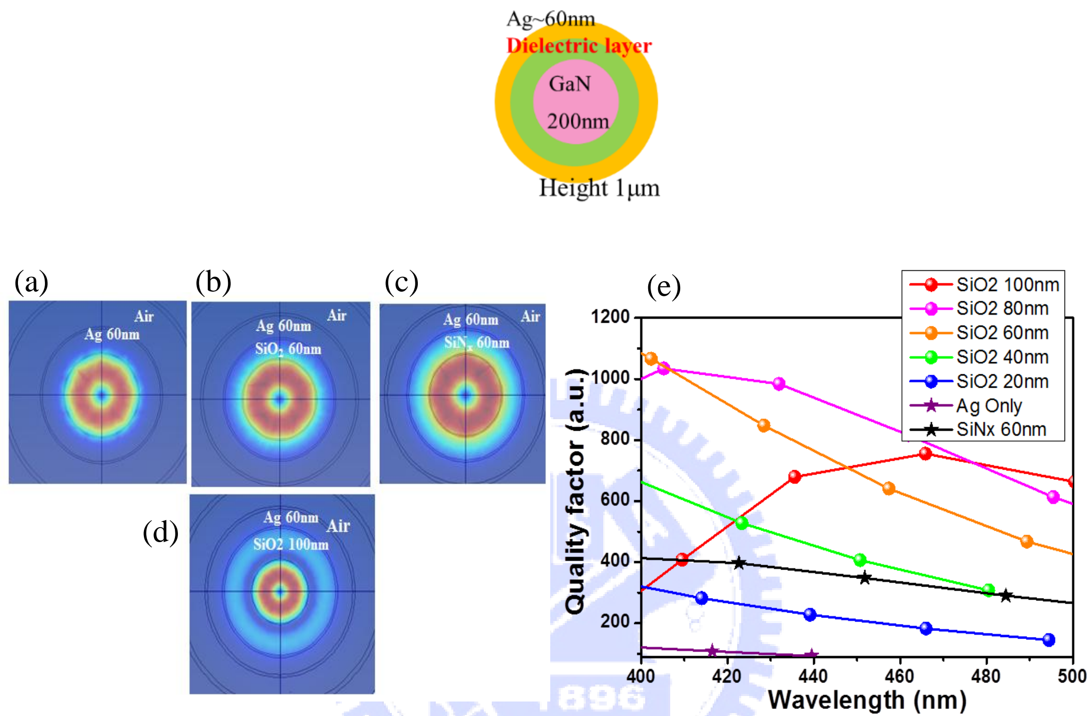

Fig. 4.12 (a) Electric field Mode patterns without dielectric layer (b)with SiO_2 60 nm (c)with SiN_x 60nm (d) with SiO_2 100 nm. (e) Quality factor of different thickness of SiO_2

Shape, diameter and height of GaN

We chose the cylinder shape just because of easy to analysis and calculation by circular waveguides theory. The diameter of GaN is concerning about the footprint of the device. Basically, we expect the footprint as small as possible. Here we chose the radius near 100 nm because there are appropriate amount of waveguides mode in this scale. Smaller diameter could give the possibility of single mode operation and better physical size of device, but this will also make more difficulty in fabrication. Here we calculate cutoff wavelength curves of different modes as we mentioned in chapter

4.1.2. Fig. 4.13 shows lowest five mode curves of the structure configuration including 60nm Ag、60nm SiO_2 and different radius of GaN rod. As you can see in Fig. 4.13 lowest five modes exist the in the wavelength between 360nm to 550nm corresponding common emission wavelength of GaN-base material when we choose the radius near100nm.

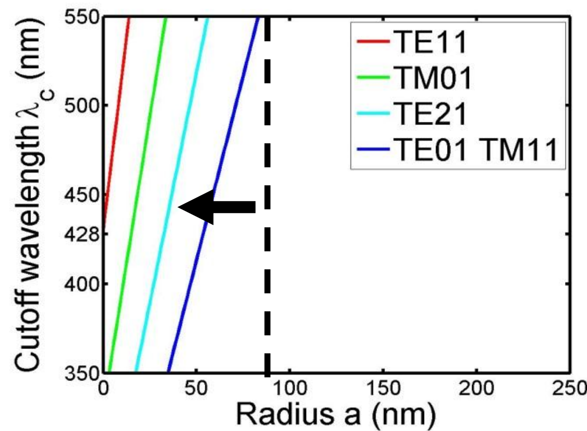

Fig. 4.13 Cutoff wavelength of the structure

Latest step, determine the structure height. As you can see in Fig. 4.14, for bulk GaN structure, cavity height both enhance quailty factor and confinement factor and threshold gain less than 1300 when height over 1000 nm. The structure configuration including 5 pairs dielectric DBRs、GaN 200 nm in diameter、50nm SiO_2、50nm Al coating and different height of GaN rod .

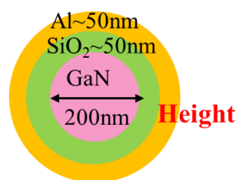

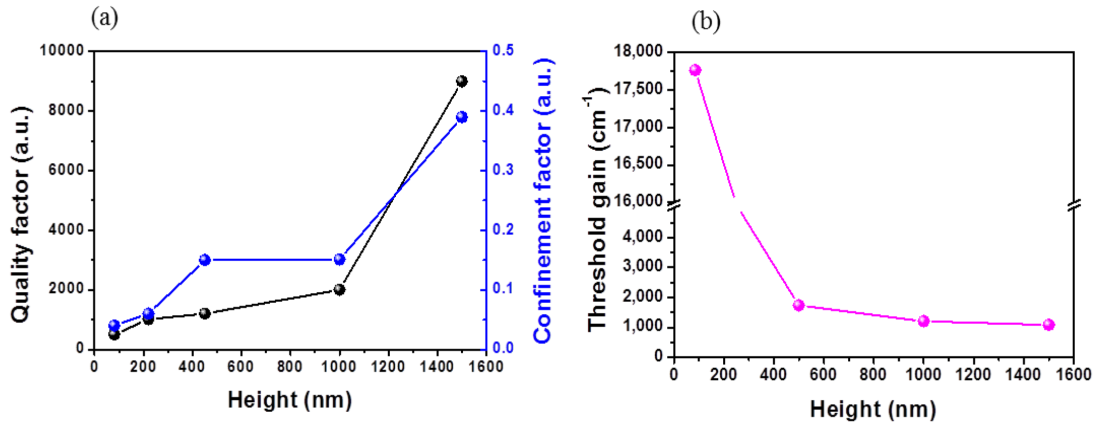

Fig. 4.14 (a) Quality factor, confinement factor and (b) threshold gain verse height of bulk GaN structure

As you can see in Fig. 4.15, for InGaN/GaN quantum wells structure, cavity height enhance Q factor, but make slight shift on confinement factor. Threshold gain less than 3000 when height over 1500nm. The structure configuration including 5 pairs dielectric DBRs、GaN 200 nm in diameter、60nm SiO_2 、60nm Ag coating and different height of GaN rod.

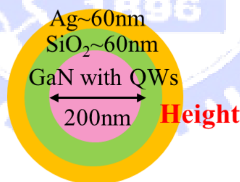

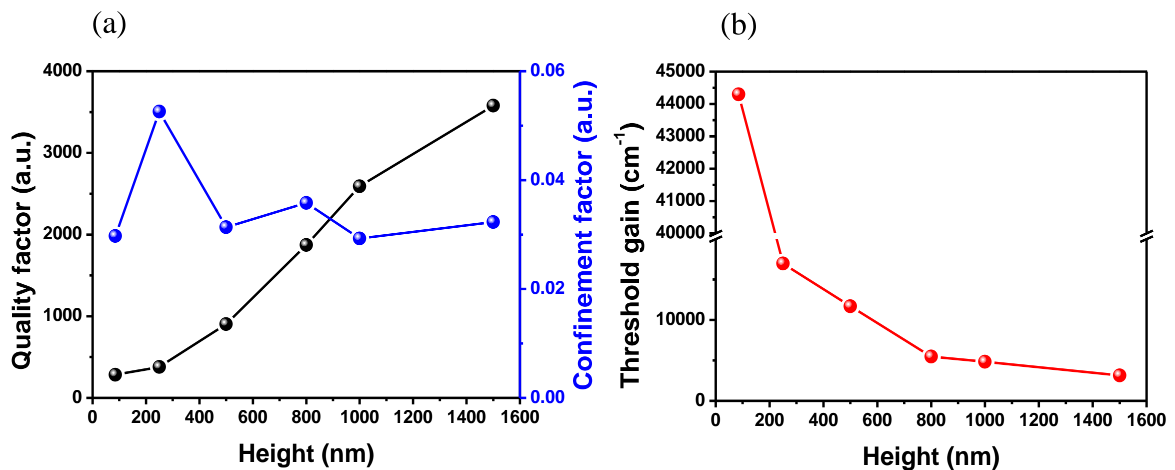

Fig. 4.15 (a) Quality factor, confinement factor and (b) threshold gain

verse t height of InGaN/GaN quantum wells structure

To reduce aspect ratio and lower threshold gain in same height, we sacrifice the foot print of structure. Because diameter raises lead to two dimensions variation, threshold gain quickly reduce to 1040 in diameter 400nm as shown in Fig. 4.16. However, increasing diameter may have several shortcomings including more transverse modes which cause multimode and reduce spontaneous emission factor in actual measurement.

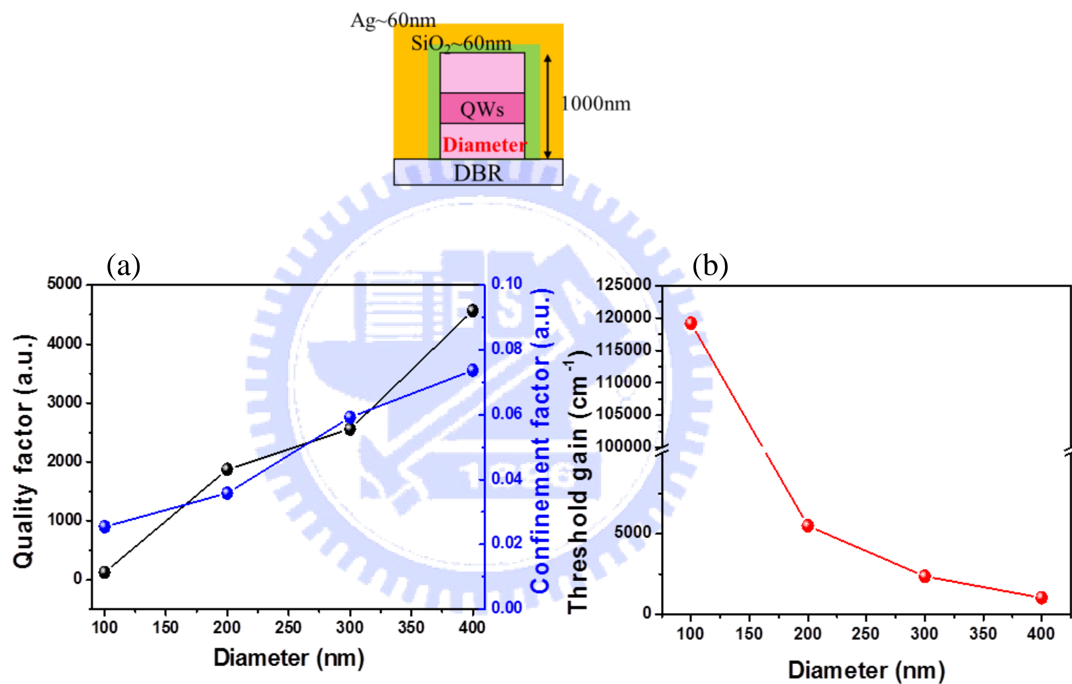

Fig. 4.16 (a) Quality factor , confinement factor and (b) threshold gain verse diameter of InGaN/GaN quantum wells structure

Preliminary results

First, we use nickel、liftoff technology and E-beam lithography system to form micor/naono-scale circle nickel hard mask. Then we use ICP dry etching GaN create GaN rod as shown in Fig. 4.17. Finally, we use PECVD and E-gun to deposit SiO2 and aluminum. A Series of diameter from 500nm to 8μm with 1.2μm in height were

made as shown in Fig. 4.17. The laser operation could be observed for both cases with or without metal coated as shown in Fig. 4.18 and Fig. 4.19 by optical pumping. However, metal coated GaN rod nanolaser shows higher quality factor and real threshold pumping energy density. Those could be attributed to metal layer provide improvement of top confinement and absorb incident pumping power. Better quality factor 、lower threshold、smaller structure size may be achieved by applying bottom DBR.

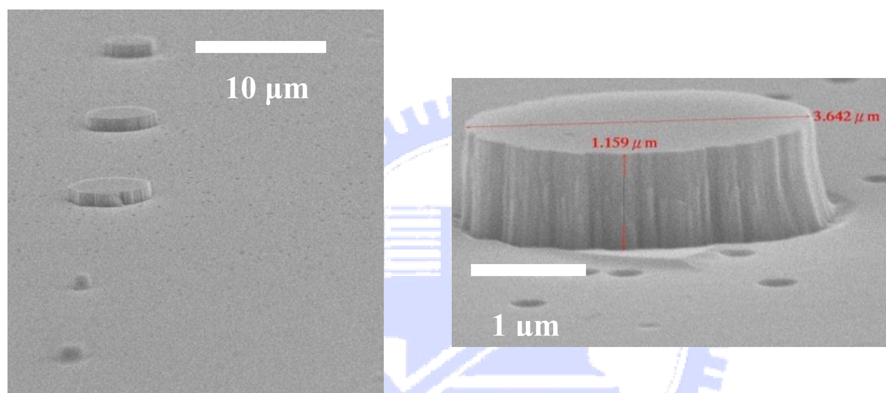

Fig. 4.17 SEM image of bulk GaN rod before Al deposition

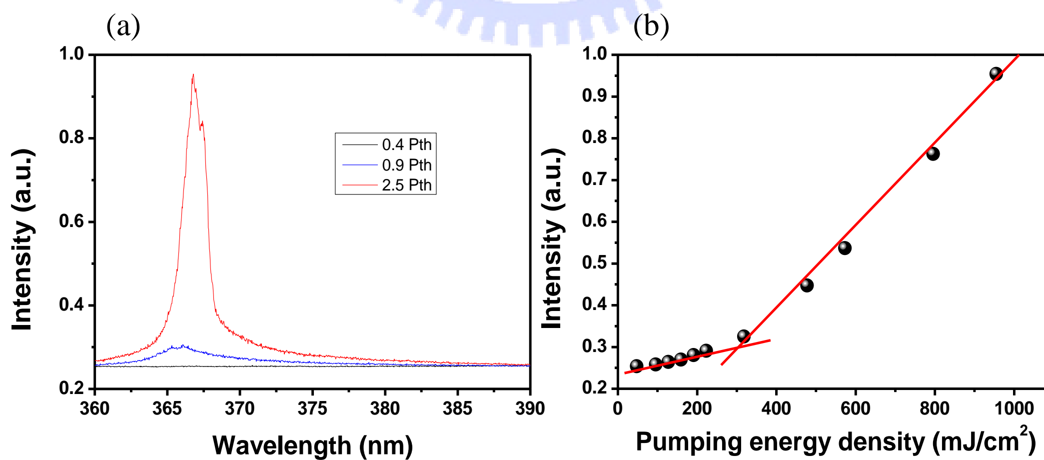

Fig. 4.18 PL spectrum and L.L curve of bare GaN rod with 1.2μm in height and 3.6μm in diameter.

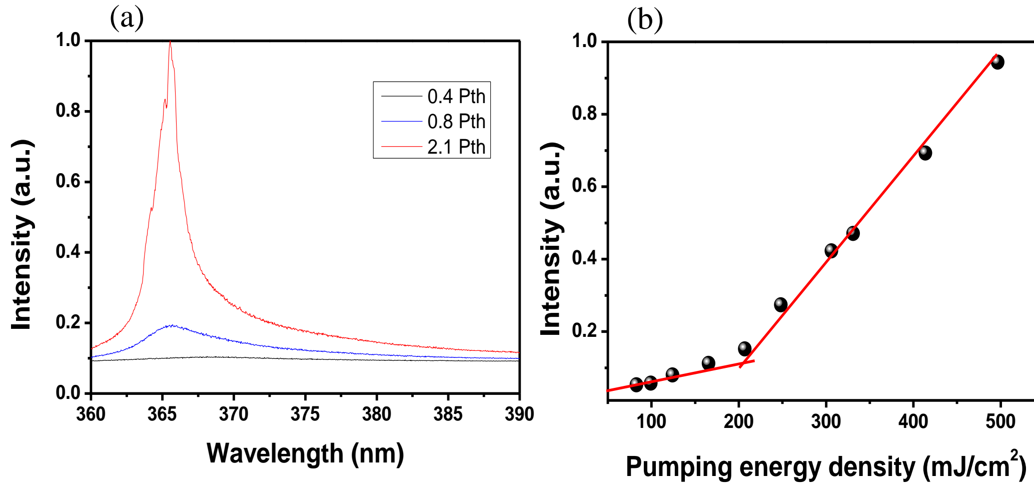

Fig. 4 .19 PL spectrum and effective L.L curve of metal coated GaN rod with 1.2μm in height and 3.6μm in diameter.

4.3 Summary

We design bulk GaN-based metal coated nanolaser combining 5 pairs of DBR, 50nm SiO2 and 50nm aluminum coating, the diameter and height of structure were controlled under 200 nm and 1 μm.We design QWs GaN-based metal coated nanolaser structure combining 5 pairs of DBR, 60nm SiO2 and 60nm silver coating, the diameter and height of structure were controlled under 500 nm and 1 μm. The TE11 and TE01 modes are two most likely modes for laser operation. We achieved a bulk GaN-based near nano-scale metal-coated laser with a lower threshold energy density compared to that of the uncoated GaN rod. The real metal-coated nanolaser could be achieved by improving the fabrication technique and using the DBR layer.

Reference

[1] William L. Barnes , Alain Dereux and Thomas W. Ebbesen, Nature, vol424, 14 august 2003

[2] X.D. Hoa, A. G. Kirk, M. Tabrizian, Biosensor and Bioelectronics, vol. 23, pp. 151, 2007.

[3] W. Striburavanich, L. Pan, Y. Wang, C. Sun, D. B. Bogy, and X. Zhang, Nat. Nanotechnology vol. 3, pp. 733, 2008.

[4] M. F. Garcia-Parajo, Nat. Photonics, vol. 2, pp. 201, 2008

[5] M. T. Hill, Y. S. Oei, B. Smallbrugge, Y. Zhu, T. de Vries, P. J. van Veldhoven, F. W. M. van Otten, T. J. Eljkemans, J. P. Turkiewicz, H. de Waardt, E. J. Geluk, S. H. Kwon, Y. H. Lee, R. Notzel, and M. K. smit, “Lasing in metallic-coated nanocavities,” Nat. Photonics, vol. 1, pp. 589, 2007.

[6] Cheng, D K, Field and Wave Electromagnetics, AW, 2ed, 1989.719s.djvu

Chapter 5

Conclusion and Future Work

5.1 Conclusion

We demonstrate the lasing behavior of GaN-based laser with mirco and near-nano scale cavity.

The laser liftoff GaN-based VCSELs with two dielectric DBRs were fabricated and measured. The device structure is composed of highly reflective TiO2/SiO2 p-DBR and HfO2/SiO2 n-DBR. The wavelength of the peak emission peak from the VCSEL is 401 nm with narrow line-width of 0.51 nm. Although the goal of laser operation under electrical operation is not achieved yet, we have successfully fabricated a complicated structure, which has high Q factor over 800 and the expected transverse modes have been measured.

We design a GaN-based nanolaser structure which can be achieve by etching method or epitaxial method. A series of simulations and experiments have been proposed. By finite element method and circular waveguides theory, we prove that the metal coated on nanocy rod provide better optical confinement. The mechanism of each part of the structure has been discussed. And because the prototype uses a dielectric layer and metal, the structure can be easily transform to electrical pumped laser. We also observe the lasing peak with wavelength about 365 nm and the quality factor about 198 for our metal-coated bulk GaN nano rod.

5.2 Future work

For microcavity light emitter (VCSELs), fabrication optimization including MQWs, AlN thickness, regrowth temperature and lithography mask design could further be improved. Using of nonpolar GaN and freestanding GaN substrate could make the structure with more academic value.

For nanocavity light emitter (metallic cavity), fabrication optimization including E-beam lithography, epitaxial type nanostructure, high quality crystalline metal layer could further be improved. Surface plasmon effect still gives the dream of ultra-small nanolaser. By applying of infra-red semiconductor material, metal coated nanolaser could make huge impact in real communication system.